

Probing the interior physics of stars through asteroseismology

C. Aerts (ORCID 0000-0003-1822-7126)*

*Institute of Astronomy,
Department of Physics & Astronomy,
KU Leuven, Celestijnenlaan 200D, 3001 Leuven,
Belgium[†]*

(Dated: Received: 13 December 2019; Accepted: 5 October 2020; To be published in Vol. 93, 2021)

Yearslong time series of high-precision brightness measurements have been assembled for thousands of stars with telescopes operating in space. Such data have allowed astronomers to measure the physics of stellar interiors via nonradial oscillations, opening a new avenue to study the stars in the Universe. Asteroseismology, the interpretation of the characteristics of oscillation modes in terms of the physical properties of the stellar interior, brought entirely new insights in how stars rotate and how they build up their chemistry throughout their evolution. Data-driven space asteroseismology delivered a drastic increase in the reliability of computer models mimicking the evolution of stars born with a variety of masses and metallicities. Such models are critical ingredients for modern physics as a whole, because they are used throughout various contemporary and multidisciplinary research fields in space science, including the search for life outside the solar system, archaeological studies of the Milky Way, and the study of single and binary supernova progenitors, among which are future gravitational wave sources. The specific role and potential of asteroseismology for those modern research fields are illustrated. The review concludes with current limitations of asteroseismology and highlights how they can be overcome with ongoing and future large infrastructures for survey astronomy combined with new theoretical research in the era of high-performance computing. This review presents results obtained through major community efforts over the past decade. These breakthroughs were achieved in a collaborative and inclusive spirit that is characteristic of the asteroseismology community. The review's aim is to make this research field accessible to graduate students and readers coming from other fields of physics, with incentives to enjoy and join future applications in this glorious domain of astrophysics.

Keywords: Variable and peculiar stars; Binary stars; H & He burning; Satellite data analysis; Composition of astronomical objects; Perturbative methods; Time series analysis; Astronomical masses & mass distributions

CONTENTS

I. Looking deep into stars	2	5. Nonstandard 1D models with rotation and waves	21
A. Stars and their “good” vibrations	3	6. One-dimensional equilibrium models as input for asteroseismology	25
B. The beginnings of space asteroseismology	6	B. Linear nonradial oscillation modes	25
C. Asteroseismology to improve stellar evolution	8	1. Pressure and gravity modes	26
D. Working in the Fourier domain truly helps	10	2. Asymptotic representations of high-order modes	27
1. Mode damping and mode lifetimes	12	3. Rotational splitting in a perturbative approach	31
2. Undamped oscillations with quasi-infinite lifetimes	12	4. Gravitational-inertial modes in the Traditional Approximation	33
3. Damped oscillations with short lifetimes	13	5. Rossby modes	34
II. Nonradial oscillations of stars	16	III. Principles of asteroseismic modeling	35
A. Stars and their hydrodynamics	16	A. Excitation mechanisms	36
1. The stellar structure equations	16	1. Heat mechanisms and stochastic driving	36
2. Simplification to 1D stellar models	18	2. Nonlinear resonant mode excitation	37
3. Standard 1D stellar models in hydrostatic equilibrium	19	3. Convectively driven internal gravity waves	38
4. Nonstandard 1D models with microscopic atomic diffusion	20	4. Tidal excitation of nonradial modes	39
		B. Mode identification	41
		1. Mode identification from échelle diagrams	41
		2. Mode identification from rotationally split multiplets	41
		3. Mode identification from period-spacing patterns	42
		C. Asteroseismic modeling using mode frequencies	42
		1. Some modeling preliminaries	42
		2. Setup of the modeling approach	43
		3. Considering individual stars and ensembles	45
		IV. Applications of asteroseismic modeling	46

* <https://fys.kuleuven.be/ster/staff/conny-aerts>;
Conny.Aerts@kuleuven.be

[†] Also at Department of Astrophysics, IMAPP, Radboud University Nijmegen, Heyendaalseweg 135, 6525 AJ Nijmegen, the Netherlands and Max Planck Institute for Astronomy, Königstuhl 17, 69117 Heidelberg, Germany

A. Sizing, weighing, and aging stars with convective envelopes	47
B. Assessing sharp features in stellar structure	49
C. Improving the physics of cool-star surface convection	51
D. Improving the theory of angular momentum transport	53
E. Inference of internal mixing from g modes	54
F. The beginnings of tidal asteroseismology	56
V. Glorious road map for the future	58
Acknowledgments	59
References	60

I. LOOKING DEEP INTO STARS

In his News and Views published in 1985 in the journal *Nature*, Douglas Gough (Gough, 1985b) announced the “*Beginnings of asteroseismology*”¹. He explained that this is

“The science of determining the internal structure of stars from the properties of dynamical oscillations”,

following the earlier introduction of the term in the scientific community by Jørgen Christensen-Dalsgaard during a conference in Meudon in 1984 (Christensen-Dalsgaard, 1984). Gough ends his *Nature* article with the exciting prospect of “*getting direct information about the stratification of the energy-generating core of a distant star*”, which sounded like a revolutionary idea at that time. A decade later, a less optimistic view was expressed by Brown & Gilliland (1994) in the introduction of their review paper entitled “*Asteroseismology*”:

“The Sun is (and will likely remain) the outstanding example of the progress that can be made using seismological methods”.

It is remarkable that a cosmologist was more optimistic on the matter than the experts, as expressed by Malcolm Longair (Longair, 2001) in his invited reflection entitled “*Facing the Millennium*”:

“...At the same time, we need to understand the internal structures of the stars. In 1915, the breakthrough came with the plotting of the Hertzsprung-Russell diagram for a few hundred stars for which distances had been measured. The counterpart for the 21st century will be asteroseismology, the direct measurement of the internal structure of the stars by measuring their normal modes of

oscillation. It is salutary to note that helioseismology has revolutionized our understanding of the interior of the Sun in ways which could not necessarily have been predicted. The precise location of the boundary between the radiation- and convection-dominated zones and their three-dimensional structures are spectacular advances – a major goal of the astronomy of the future must be to perform the same studies on the stars present in the Hipparcos Hertzsprung-Russell diagram”.

Meanwhile, we have amazing Gaia Hertzsprung-Russell diagrams (HRDs) based on space astrometry with microarcsecond precision for more than a billion stars in the Milky Way and beyond (Gaia Collaboration, Babusiaux et al., 2018) and asteroseismology for tens of thousands of those. Indeed, the past decade has seen the assembly of long-duration (up to four uninterrupted years) photometric data thanks to dedicated space missions, leading to the time-variable properties of stars derived with precisions of micromagnitude (μmag). This corresponds to flux variations at levels of parts-per-million (ppm). The primary research goal of several of those missions was the search for exoplanets around distant stars, but this is fine: the machinery delivered the data appropriate for asteroseismology (quite often, derogatorily, called “stellar noise” by exoplanetologists, while it actually concerns beautiful stellar signal; see the later discussion of Fig. 3). Asteroseismology based on these space photometric light curves meanwhile delivered interior rotation rates, stratification properties, and ages of thousands of distant stars, with impressive relative precisions unachievable by other methods (Aerts et al., 2019, Table 1). The past few years, we have even reached the status of being able to derive the core rotation frequency for more than a thousand stars and the near-core mixing for many of them. The Sun is no longer the outstanding example to assess the properties of the deep interiors of stars. Those properties have become accessible thanks to the detection and interpretation of hundreds of nonradial oscillations with probing capacity of the deepest internal layers of the stars. Such modes have now been identified in stars across almost the entire stellar mass range and have turned stellar interiors into observational territory.

History has shown the optimistic daring views to be visionary and at the same time entirely justified. The study of stellar interiors is nowadays a data-driven modern topic. As we highlight in this review, asteroseismology not only reveals the need for better models of stellar structure and evolution but is paving the way toward them. It brings us into the *renaissance* of stellar evolution theory and does so from a multidisciplinary approach relying on space science and technology coupled with mathematical modeling. More particularly, as-

¹ For the etymology of this specific term in astrophysics, see Gough (1996) in response to the anecdote on the terminology raised by Trimble & Leonard (1996).

teroseismology involves data analysis methods such as time-series analysis, pattern recognition, and statistical modeling, while relying on various fields of physics and chemistry such as thermodynamics, nuclear and atomic physics, and quantum mechanics. The bridging of these scientific fields, starting from the appropriate observational input, allows us to achieve the long-awaited calibration of the physical properties of stellar interiors. We anticipate that the asteroseismically calibrated stellar models will be highly beneficial for various fields of research in astronomy and in computational physics in general.

We now provide concise discussions of some key observational and data analysis aspects of asteroseismology, omitting many of the details, which can be found in the referenced literature. The bulk of the review then focuses on calibrating and improving the physics of stellar interiors, much in line with the previous quotations and with the purpose of *Reviews of Modern Physics*.

A. Stars and their “good” vibrations

Stellar variability is omnipresent in the HRD, which is a key diagnostic diagram used to evaluate stellar evolution theory. Such evaluations are often done by comparing the position of observed stars in this diagram with evolutionary tracks, such as the ones indicated by the full lines in Fig. 1. These tracks are based on particular versions of stellar evolution theories, of which there are many variants as further outlined in Sec. II.A. Those types of comparisons between observations and theory are merely a crude evaluation because the HRD relies on only two quantities: the effective temperature of the star T_{eff} and its luminosity L (usually expressed in solar luminosity L_{\odot}). As detailed in Sec. II.A, stellar models contain a multitude of free parameters and rely on input physics suffering from uncertainties. The evaluation of these models therefore requires additional observational diagnostics to accompany the position of an observed star in the HRD. Surface abundances derived from high-precision spectroscopy offer important constraints in this respect, among various other observational diagnostics of the stellar atmosphere. These typically reach relative precisions of 1% to 5% for the best cases (see Table 1 of Aerts et al., 2019).

A new view on stellar variability in the HRD is offered by data from the European Space Agency (ESA) Gaia satellite (Gaia Collaboration, Eyer et al., 2019). Using 22 months of calibrated photometric, spectro-photometric, and astrometric Gaia data, this study showed how the large-amplitude radial modes of classical variables, such as Cepheids, RR Lyr stars, and Miras (indicated in Fig. 1), makes them “move” in the observational analog of the HRD, i.e., a color-absolute magnitude diagram, during their pulsation cycle. This introduces a new

“time” dimension in the evaluation of stellar evolution theory. These radial pulsators remain of vast interest and importance for observational cosmology, e.g., Soszyński et al. (2016) and Anderson & Riess (2018), but are not considered in this review. Our attention is directed entirely to stars exhibiting multiple nonradial oscillation modes, which in the context of asteroseismology deserve to be called “good vibrations” after the eponymous 1966 song by the Beach Boys.

From a physical viewpoint, nonradial oscillation modes are solutions to the equation of motion of a star that gets perturbed from its equilibrium. The modes are classified into two main groups according to which of the two forces, the pressure force or the buoyancy force of Archimedes, is dominant in restoring the equilibrium. Modes dominantly restored by the pressure force are called pressure modes, or ‘p modes’ for short. These mainly have large amplitude in the envelopes of stars and are characterized by dominant radial motions. Gravity modes, or ‘g modes’, are dominantly restored by the buoyancy force of Archimedes and attain large amplitudes in the deep interior of the star; they are characterised by dominant horizontal motions. As stars evolve, a powerful type of modes having a pressure-mode character in the envelope and a gravity-mode character in the deep interior emerges. These so-called mixed modes have excellent probing power throughout the entire star.

A formal mathematical definition of nonradial oscillation modes is given in Sec. II. However, it is instructive to already know how the modes ‘look like’. One can consider nonradial modes of a 3D spherical star as the analogy of the vibration modes of a 1D string. Each vibration mode of a string makes it deviate from its equilibrium position and is characterized by three numbers: its frequency, its amplitude, and its number of nodes n . The nodes are points where the string does not move during the vibration cycle. One adopts the terminology that $n = 0$ corresponds to the fundamental vibration mode of the string, $n = 1$ to the first overtone, $n = 2$ to the second overtone, etc. Each nonradial mode of a 3D star makes the gas particles in this star deviate from their equilibrium position and is also characterized by a frequency and an amplitude, but now three integer numbers are needed to indicate the positions of the nodes of the displacement vector with respect to a symmetry axis of the star. Given that it concerns a 3D spherically symmetric body whose fluid elements get displaced from their equilibrium position by a vector $\boldsymbol{\xi} = (\xi_r, \xi_\theta, \xi_\phi)$, the angular geometry of this vector is described in terms of a spherical harmonic function, containing a Legendre polynomial P_l^m as a function of colatitude θ and a harmonic function in terms of azimuth ϕ . The rotation axis is usually taken as the symmetry axis of the modes. Thus for each nonradial oscillation mode, three labels (l, m, n) are used to indicate the nodes of the mode, where l is the total number of nodal lines on the stellar surface and $|m|$ of

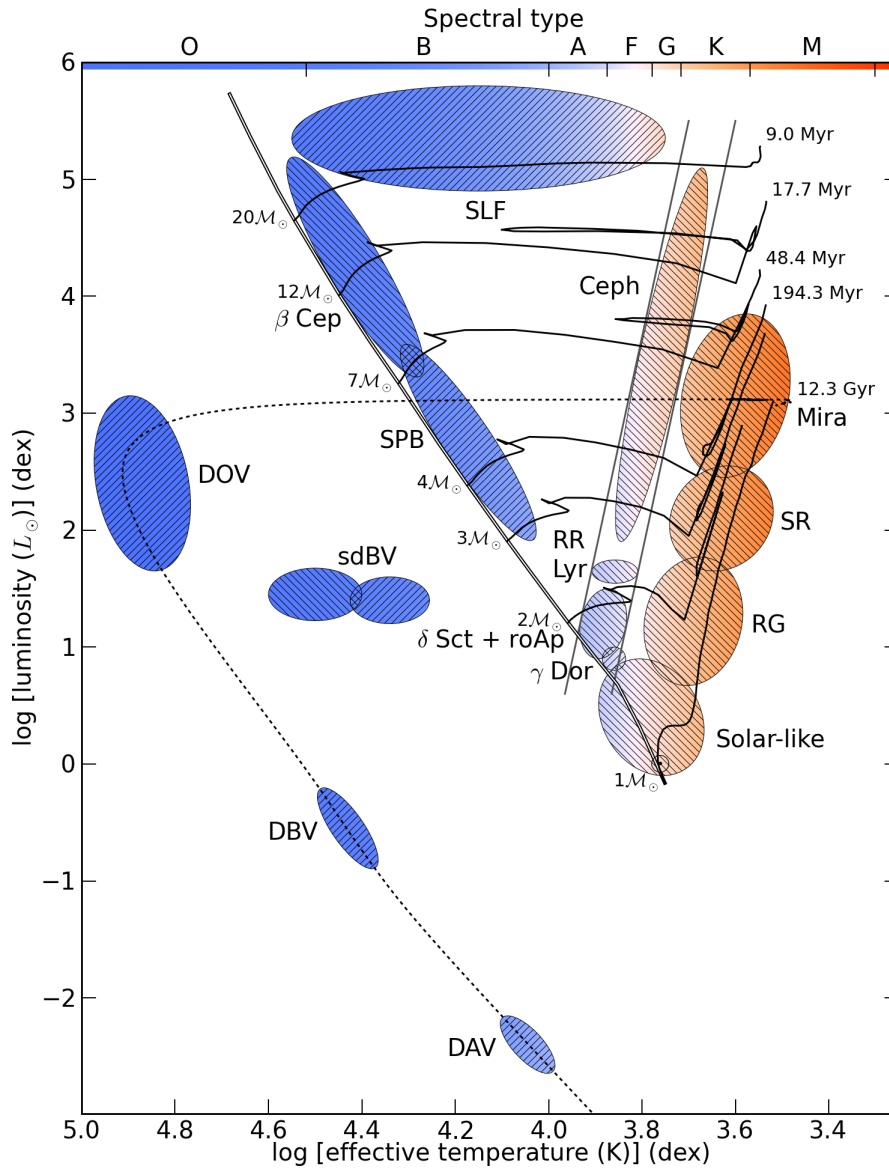


FIG. 1 Hertzsprung-Russell diagram (HRD) showing the position of different classes of pulsating stars. The abbreviation of the classes follows the nomenclature used by Aerts et al. (2010, Chapter 2), to which we refer for extensive discussions of all indicated classes in terms of the excitation mechanisms, along with the typical periods and amplitudes of the oscillations. The hatching linestyle used inside each of the ellipses marks the dominant type of oscillation mode in each class: // for gravity modes and \ for pressure modes. The recently discovered stochastic low-frequency (SLF) variability in O-type stars and blue supergiants is discussed in the text and has been added as a comparison with previous versions of this plot. The solid black lines and the black dotted line represent standard evolutionary model tracks, with birth masses and evolutionary timescales as indicated. The borders of the classical instability strip are plotted with gray lines, while the double line represents the zero-age main sequence. Early versions of this figure were made by Jørgen Christensen-Dalsgaard (Aarhus University) and by Pieter Degroote (KU Leuven). This updated version was produced by Péter Pápics based on the version in his PhD Thesis (Pápics, 2013).

those nodal lines pass through the symmetry axis. The n value again indicates the overtone of the mode, which now concerns the number of nodal shells situated inside the star that do not move during the oscillation cycle. The special case of a radial mode has $l = m = 0$ and displaces the fluid elements inside the star in the radial

direction only.

The symmetry axis of the oscillations is “inclined” with the line of sight of a distant observer by an unknown angle called the inclination angle i . Figure 2 gives a visual representation of the radial component of the displacement vector ξ_r for some typical nonradial modes “observed”

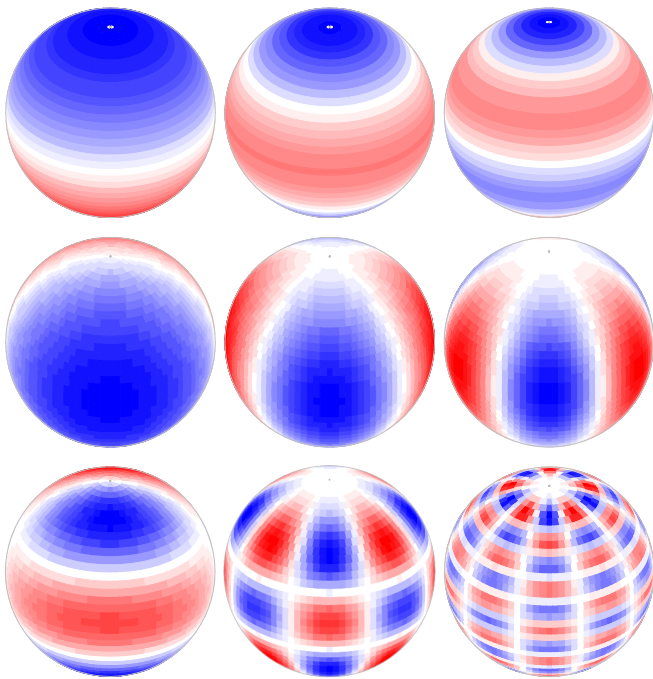


FIG. 2 Snapshot of the angular dependence of the radial component of the displacement vector ξ_r at one point in the oscillation cycle for various nonradial modes, seen under an inclination angle of 60° . White bands indicate the positions where $\xi_r = 0$; red and blue represent areas at the stellar surface moving in (out) at the chosen time. Shown from left to right are first row, axisymmetric ($m = 0$) modes with $l = 1, 2, 3$; second row, sectoral ($l = |m|$) modes with $l = 1, 2, 3$; third row, tesseral ($l \neq |m|$) modes with $(l, |m|) = (3, 1), (6, 4), (15, 5)$. High-degree modes as the two in the third row are usually not detected in space photometry due to cancellation effects when integrating the flux variations across the visible stellar disk.

under an inclination angle of 60° . The term *observed* is a bit misleading here because stellar surfaces cannot be resolved well enough to study the majority of nonradial oscillations of stars, except for the Sun. Rather, the signatures of the oscillation modes are “detected” in observables that are stellar quantities integrated over the part of the stellar disk that is visible for an observer. The nonradial oscillations make some parts of the star move up (indicated in blue in Fig. 2), while others are going down (red patches in Fig. 2) periodically according to the eigenfrequency of the mode. Such motions imply small local changes in the velocity, temperature, and radius of the stellar gas, creating local flux variations. These flux variations change periodically in time during the oscillation cycle, i.e., half a cycle further the red patches in Fig. 2 will have become blue and vice versa. The surface-integrated effect due to each nonradial mode measured in flux or velocity variations by an observer depends on the inclination angle because it is determined by the position of the surface nodal lines in the line of sight. This inter-

play between the geometry of the mode and the value of i gives rise to so-called partial cancellation due to integration over the visible stellar disk, which increases as the degree of the mode increases (see Figs. 1.4 and 1.5 in Aerts et al., 2010). In particular, when nonradial modes are seen under their angle of complete cancellation, they do not lead to variability, while the latter is maximal when seen under their optimal angle of least cancellation. For the values of these special mode angles, we refer to Table B.1 in Appendix B of Aerts et al. (2010). It is also noteworthy that partial cancellation works differently in photometric versus spectroscopic data, because the integrated flux is highly sensitive to limb darkening but the integrated velocity is less sensitive to it. In addition, the effect is different for p and g modes. The sensitivity to limb darkening is smaller for p modes because their ξ_r is dominant in the line of sight, while g modes have dominant ξ_θ and ξ_ϕ and are hence much more prone to limb-darkening effects for an observer.

Measuring the small flux or velocity variations during an oscillation-mode cycle allows us to derive the mode’s period without having to resolve the stellar surface. This is how the time-variability aspect of asteroseismology works. It is in principle an easy aspect of the research provided that one has data with a high duty cycle, which is defined as the fraction of the mode period covered with data expressed as a percentage. In practice, the overall beating cycle encapsulating the global pattern due to all active modes of the star has to be covered with a high duty cycle. Moreover, the data need to have noise levels below the amplitudes of the modes in the appropriate frequency regime. These scientific requirements become easier to meet the longer the time series and the more data points that one has available. Detecting oscillation mode frequencies and estimating their uncertainty is also much easier to do from uninterrupted data with high duty cycle than from gapped time-series data with a low duty cycle.

My fellow countryman, Paul Ledoux, proposed the occurrence of two nonradial p modes in a rotating star as the explanation for the detected variable velocity behavior of the star β Canis Majoris (Ledoux, 1951). His landmark paper provided the first correct interpretation and understanding of the observed biperiodic variability (i.e., caused by two simultaneously active p modes) of a rotating star in terms of the physics of nonradial oscillations. As a member of the class of β Cep stars, β Canis Majoris was thus the first star with confirmed nonradial modes occupying the proper ellipse in Fig. 1. It took another 41 years until the excitation mechanism of those nonradial oscillations was understood in terms of a heat mechanism, also known as the opacity mechanism (Moskalik & Dziembowski, 1992). We return to mode excitation mechanisms in Sec. III.A.

During the half century following Ledoux’s insightful 1951 paper, the search for and identification of nonradial

oscillations in time-series observations became an active research field. Inventories of nonradial modes and their identification in terms of the spherical wave numbers l and m (see Sec. II and Fig. 2) grew steadily. Nevertheless, asteroseismology in the spirit of Gough and Longair, i.e., with the aim to improve the interior physics of stars undergoing nuclear fusion, was nowhere near the horizon. Major successes were, however, booked for g modes of white dwarfs along their cooling track in the HRD (see Fig. 1). In their review, Brown & Gilliland (1994) indeed discussed the category of the stars “unlike the Sun”. They illustrated that white-dwarf asteroseismology based on weeks-long ground-based multisite monitoring of nonradial oscillations was furthest advanced, and that the next best cases of the rapidly-oscillating Ap (roAp) and δ Sct stars (see Fig. 1) were still limited in terms of physical interpretation. For none of the other classes of nonradial pulsators in Fig. 1 did one come anywhere near making inferences on how to improve the physics of their interiors from exploitation of the available detected nonradial oscillations.

Although major achievements were obtained in the decade after this first review on asteroseismology by Brown & Gilliland (1994), mainly from ground-based multisite network campaigns for pulsating white dwarfs (e.g., Winget et al., 1991), hot subdwarfs (e.g. Brassard et al., 2001; Kilkenny et al., 1999), roAp stars (e.g., Kurtz et al., 2005), δ Sct stars (e.g., Breger et al., 2005), and β Cep stars (e.g. Handler et al., 2006), the plea by Brown & Gilliland (1994) to replace photometric ground-based network observations with data to be taken with spaceborne telescopes was fully justified. Space data not only would provide much lower noise by avoiding disturbances due to Earth’s atmospheric variability but also would allow one to increase the duty cycles of the data significantly, without large daily interruptions of the time series that plague data from ground-based observatories. Indeed, even successful multisite campaigns remained below 50% duty cycle, meaning that the oscillation cycles were never covered appropriately, except for white dwarfs, subdwarfs, and roAp stars, all of whose oscillations have periods of only a few to tens of minutes and dominant mode amplitudes of the order of millimagnitudes, corresponding with levels of parts per thousand (ppt) when considering the star’s flux variability rather than its change in brightness expressed in magnitude. In retrospect, the gain from space photometry was illustrated by Zwintz et al. (2000), who analyzed ten years of Fine Guidance Sensors photometry of tens of thousands of supposedly “constant” guide stars observed with the Hubble Space Telescope to stabilize the satellite. They found variability in about 20 stars, among them four K giants revealing periods of a few hours. They reported this to be incompatible with rotational variability but did not interpret it in terms of oscillations, which we now know are the cause.

While awaiting space photometry, the hunt for solarlike oscillations in solar twins from radial-velocity time series grew fast after the predictions published in the seminal paper by Kjeldsen & Bedding (1995). The ever increasing precision reached by spectrographs led to the first firm discoveries of individual solarlike oscillation modes in the nearby Sun-like stars η Boo (Kjeldsen et al., 1995), β Hyi (Bedding et al., 2001), and α Cen A (Bouchy & Carrier, 2001), after earlier unconfirmed attempts to find them in Procyon (Brown et al., 1991). Oscillation modes were also detected in radial-velocity variations of the red giant ξ Hya (Frandsen et al., 2002). By the time of space asteroseismology, detections of solarlike oscillations had been achieved for about 25 bright stars (see Figs. 2.2 and 2.3 in Aerts et al., 2010, for summary plots). All those spectroscopic data revealed mode frequencies as expected from scaling those of the Sun, which was in line with the predictions made by Kjeldsen & Bedding (1995).

B. The beginnings of space asteroseismology

A half century of intense monitoring of pulsators with nonradial oscillation modes from ground-based observatories since Ledoux’s 1951 inspiring analysis took place. Despite heroic achievements in terms of number of detected nonradial mode frequencies in δ Sct stars (as summarized by Michel Breger, Breger, 2000, its pioneer), the struggle with daily alias frequencies due to periodic gaps in the data and the lack of unambiguous identification of their (l, m) could hardly be overcome. This disappointing situation got placed in a new light thanks to an opportunity that occurred by accident, and that is to be taken literally. The NASA Wide Field Infra Red Explorer (WIRE) lost its coolant after launch and could not perform the science it was designed for. Derek Buzasi convinced NASA to reorient the WIRE satellite project into a proof-of-concept asteroseismology mission, by using its onboard 5 cm tracker telescope and camera to monitor the variability of various kinds of bright stars uninterruptedly and with high cadence during several weeks. Despite major instrumental effects due to telescope jitter (the machinery was absolutely not built to do what it was used for), this blessing in disguise immediately showed the potential gain that could be achieved should a dedicated specifically designed asteroseismology space mission become available: Buzasi (2000) discovered oscillation modes in the red giant α UMa, as anticipated by Brown & Gilliland (1994). Despite having been an unplanned pioneer, WIRE achieved ppt-level amplitude detections and above all illustrated the great improvement of being able to observe uninterruptedly from space. Among other results, it led to detections of oscillations in K giants (Stello et al., 2008), showed nonradial modes to be present in the bright δ Sct star Altair (Buzasi et al., 2005) where ground-based monitoring had failed to find

any, and drastically improved light curves of eclipsing binaries (Southworth et al., 2007).

Canada’s first space mission, Microvariability and Oscillations of STars (MOST, launched in 2003, Walker et al., 2003), was also the first space mission dedicated to space asteroseismology, although it observed all sorts of stellar variability. Given its modest aperture of 15 cm, it is known in the asteroseismology community as the HST (“Hubble Space Telescope”) baptized as such by its Principle Investigator (PI), Jaymie Matthews. MOST data revealed numerous oscillation modes in stars belonging to almost all classes indicated in Fig. 1, such as red giants (Barban et al., 2007), rapidly oscillation A peculiar (roAp) stars (Huber et al., 2008), δ Sct and γ Dor stars (Rowe et al., 2006; Sódor et al., 2014), emission-line OB stars (Saio et al., 2007; Walker et al., 2005a,b), isolated and cluster slowly pulsating B stars (SPBs, Aerts et al., 2006; Cameron et al., 2008; Gruber et al., 2012), pre-main sequence stars – pre-MS, see Zwintz (2008) and Zwintz et al. (2009), and many more (see Matthews, 2007, for an early status report). Even though it could monitor stars for a period of only about six weeks maximally (limiting the precision of the oscillation frequencies) and its photometric precision in the time domain was of order ppt, it revealed many more oscillation modes than what had been achieved from ground-based campaigns. In many respects MOST was a highly successful (and inexpensive) planned pioneering mission.

The first “major” space mission dedicated to the monitoring of numerous nonradial pulsators with the aim of space asteroseismology (along with exoplanet hunting) was the French-led CoRoT mission. It was launched in 2006 into a low-Earth orbit and was operational until 2012 (Auvergne et al., 2009; Baglin et al., 2009). Its original acronym stood for “Convection et Rotation” (CoRot) but later in the project the exoplanet hunting was added to get the mission funded and hence the “t” got upgraded to “T” so as to match “Convection, Rotation, and exoplanetary Transits”. CoRoT carried a 27 cm telescope and was dedicated to asteroseismology of tens of bright stars (V magnitude between 5 and 9) monitored with a cadence of 32 s and exoplanet hunting around thousands of faint stars (V magnitude between 11 and 16) measured every 15 min during each of its pointings (see Auvergne et al., 2009, for the technical and operational details pertaining to the mission). Because of its construction and low-Earth orbit, CoRoT was able to point in the center or anticenter direction of the Milky Way over five uninterrupted months (its so-called long runs), between which it did short runs of about a month in duration. This meant that the target selection and the choice of the Fields-of-View (FOVs) to point at were critical and had to be optimized to meet the wishes of two until then hardly collaborating communities, the asteroseismologists and the exoplanet hunters, from the numerous countries that funded the mission. This “astrosoci-

ological” aspect of the mission led to heated debates (in various languages) during the so-called “CoRoT weeks”, which were preparatory workshops held twice a year to optimize the mission planning and exploitation. Had it not been for the heroic leadership of the mission PI Annie Baglin, we would have kept on changing our minds about the pointings until the day of the launch.

CoRoT was a major success on various fronts. It properly allowed asteroseismology of Sun-like stars as done by Michel et al. (2008), Appourchaux et al. (2008), García et al. (2009), Benomar et al. (2009), Deheuvels et al. (2010), Mathur et al. (2010), and Ballot et al. (2011), where the last study treated an exoplanet host star. It also led to the discovery of nonradial oscillations in red giants (De Ridder et al., 2009), opening up the major unexploited parameter space of so-called solarlike oscillations in evolved stars as studied by Hekker et al. (2009), Miglio et al. (2009), Barban et al. (2009), Mosser et al. (2010), and Kallinger et al. (2010). Applications to other types of nonradial pulsators are too numerous to mention, but a few breakthroughs were the discovery of outbursts with accompanying mass loss in Be stars due to the nonlinear interaction between nonradial modes observed in real time (Huat et al., 2009), the occurrence of stochastic nonradial oscillations in B-type stars (Belkacem et al., 2009; Degroote et al., 2010b; Neiner et al., 2012, the latter in the gravito-inertial regime – see below for an explanation of these types of modes), asteroseismic modeling of an O9 star (Briquet et al., 2011), the discovery of low-frequency variability in O-type stars that remained unexplained at that time (Blomme et al., 2011, see below for interpretations), and several eclipsing binaries with tidally induced or tidally affected nonradial oscillations, such as in Maceroni et al. (2009) and Maceroni et al. (2013) and da Silva et al. (2014). Many other results remain unmentioned here. The special volume 506 (2009) of the journal *Astronomy and Astrophysics*² was dedicated to 55 CoRoT papers and offers the reader an extensive review on the mission’s instrument performance and scientific results.

And then came the amazingly successful NASA *Kepler* mission (Koch et al., 2010), launched in 2009, delivering light curves of unprecedented quality, as shown in Fig. 3 for a few stars observed in its long cadence mode (29.43 min). *Kepler* delivered light curves with a duration of four years, for about 200000 low- and intermediate-mass stars in one FOV in the northern sky. These data have a 10 times longer time base and deliver a factor ~ 100 better precision for the oscillation frequencies than the CoRoT data, thanks to the larger aperture of the telescope (0.95 m), the longer pointing, and the more stable

² Journal volume available in open access at <https://www.aanda.org/component/toc/?task=topic&id=9>.

Earth-trailing orbit. The nominal *Kepler* mission lasted four years and had a dedicated asteroseismology program (Gilliland et al., 2010), monitoring several hundred low-mass stars at a short cadence of 58.85 s. After the nominal four-year mission, the *Kepler* spacecraft lost two of its four working reaction wheels. The mission was then repurposed as a space project monitoring fields in the ecliptic, making clever use of the solar radiation pressure to stabilize the satellite. This mission operated under the name K2 and monitored 19 fields, each of which during maximally ~ 80 d between February 2014 and October 2018, adopting the same cadence types as *Kepler* (Howell et al., 2014). Because of its superior quality, most of the results discussed in this review are based on *Kepler* (or K2) data, so we do not summarize results here as we did for the other space missions.

The BRiGht Target Explorer constellation (BRITE; launched in 2014 and currently operational) is a set of Austrian, Canadian, and Polish nanosatellites assembling multicolor photometry of the brightest stars in the sky for variability studies and asteroseismology (Weiss et al., 2014). BRITE is unique in that it offers two-band photometry based on a narrow blue and a broad red filter. While the data reduction was initially a challenge, given the limited weight and pointing stability of the small satellites, its photometric precision currently reaches ppt per data point. It can monitor selected stars during about half a year (Pablo et al., 2016). BRITE is monitoring a variety of bright variables. BRITE's data of high-mass stars is complementary to the *Kepler* data in terms of targets. BRITE revealed several more nonradial oscillation modes than what has been found in ground-based data for OB- and Be-type pulsators (e.g. Baade et al., 2016; Handler et al., 2017; Kallinger et al., 2017; Pigulski et al., 2016; Ramiaramanantsoa et al., 2018). Combined BRITE data and archival data assembled from extensive ground-based (multisite) campaigns or data that are currently being assembled by the NASA Transiting Exoplanet Survey Satellite (TESS, Ricker et al., 2016) hold good potential for asteroseismology of the highest-mass nearby stars with high-amplitude oscillation modes to perform modeling of their interior properties.

Handler et al. (2019) illustrated the TESS potential in revisiting bright B-type pulsators discovered from the ground but lacking sufficient identified pulsation modes. The nominal TESS mission is scanning almost the full sky, delivering high-precision space photometry for millions of stars with time bases between 27 and 352 d for each of the hemispheres, with similar cadences as *Kepler*. This difference in duration of the monitoring is due to its operational scheme of observing in sectors (13 per hemisphere), each monitored over 27 d. Increasing partial overlap between the consecutive sectors occurs for areas in the sky closer to the ecliptic pole, with a maximum of continuous observation over 352 d for stars in the TESS Continuous Viewing Zone (CVZ). TESS samplings

changed to 10 min and 20 s for the long and short cadence modes, respectively, in the extended mission (started in mid 2020). Owing to the more limited time base it delivers far less precise oscillation frequencies for asteroseismology than *Kepler*, but it opens up the entire sky to provide large samples of pulsators. Some of these samples were not yet treated by CoRoT and *Kepler*, including metal-poor high-mass stars in the Large Magellanic Cloud (LMC). Thus far large asteroseismology samples have essentially been limited to red-giant pulsators. In that sense, TESS will bring major advances for a variety of stars across the HRD in Fig. 1, from low-mass unevolved Sun-like stars (Schofield et al., 2019), including exoplanet hosts (Campante et al., 2016b), all the way up to the most massive stars.

The past decade brought us to a golden era for asteroseismology, with the BRITE and TESS missions ongoing, the PLANetary Transits and Oscillations of stars mission (PLATO, Rauer et al., 2014) on the horizon, and an immense amount of *Kepler* data yet to be interpreted in the true meaning of asteroseismology, i.e., with the aim of improving the physics of stellar interiors. How to achieve that, is discussed in the rest of the review.

C. Asteroseismology to improve stellar evolution

The HRD in Fig. 1 reveals that pulsational variables occupy many phases of stellar evolution. The periods of nonradial oscillations covered by stars and stellar remnants range from seconds to months or even years and their amplitudes of brightness variations cover the range of a magnitude to the current detection threshold of μmag (corresponding to hundreds of ppt to ppm in flux variability). We refer to Table A.1 given by Aerts et al. (2010) for a summary of the pulsation characteristics. The basic properties and the excitation mechanisms of all known classes of nonradial pulsators indicated in Fig. 1 were discussed in great detail in Chap. 2 given by Aerts et al. (2010). Noteworthy discoveries of nonradial oscillations not yet firmly established from ground-based data were made for red giants from CoRoT (De Ridder et al., 2009) and for blue supergiants from MOST (Saio et al., 2006), Hipparcos (Lefever et al., 2007), and *Kepler* (Aerts et al., 2017a). While oscillations were already discovered in red giants from ground-based spectroscopy, it was still heavily debated whether or not it concerned radial or nonradial oscillations (e.g., Frandsen et al., 2002). Both red giants and blue supergiants are meanwhile established as nonradial pulsators from early *Kepler* (Bedding et al., 2010), K2 (Bowman et al., 2019b), and TESS data (Pedersen et al., 2019). Hence they received their own ellipse and Fig. 1 was adapted accordingly.

The *Kepler* spacecraft led to the discovery of more than 20000 red giants with nonradial oscillations (Hon et al., 2019), and TESS will undoubtedly provide a fac-

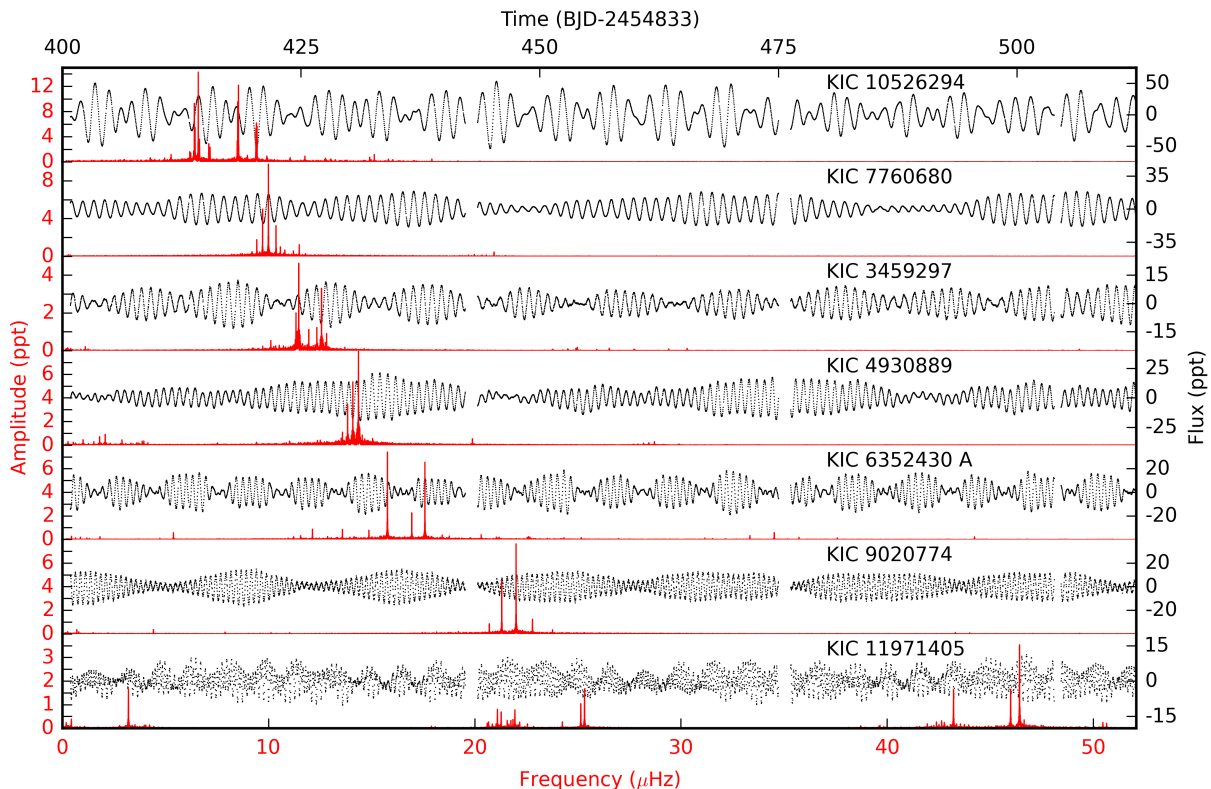


FIG. 3 Excerpts of 110 d duration (of the total ~ 1500 d) extracted from the *Kepler* long-cadence (~ 30 min per point) light curves (in black dots) of seven slowly pulsating B stars (see Fig. 1) indicated with their *Kepler* input catalog identification (KIC, Brown et al., 2011). The amplitude spectrum obtained from a Fourier transform of the full *Kepler* light curves is overplotted in red. These stars exhibit nonradial gravity modes with individual mode periods of the order of 1 d. The light curves reveal a gallery of diverse beating patterns among the modes and a gradual shift in maximum amplitude from low to high frequency as their rotation frequency changes from low in the top panel to high in the bottom panel. Despite their large amplitudes of several to ~ 12 ppt, none of these stars were known to have nonradial oscillations prior to the *Kepler* mission; it is notoriously difficult to detect modes with such periodicities from ground-based data given their similarity with the rotation period of Earth. Figure based on data from Pápics et al. (2017), by courtesy of Péter Pápics, KU Leuven.

tor of 10 more. Numbers for blue supergiants discovered from K2 and TESS are much lower, in the order of a few hundred, because these are rare objects. Moreover, they were omitted from the nominal *Kepler* FOV so as not to “disturb” the exoplanet hunting. The variability of O-type dwarfs and blue supergiants is caused by a complex interplay between various phenomena, which may involve internal gravity waves (IGWs, Rogers et al., 2013), rotational modulation (Ramiamanantsoa et al., 2018), sub-surface convection (Grassitelli et al., 2015), wind variability (Krtićka & Feldmeier, 2018), magnetism (Sundqvist et al., 2013), nonradial g modes (Moravveji et al., 2012), and binarity (Sana et al., 2012). The discovery of ubiquitous low-frequency power excess in hundreds of OB dwarfs and supergiants in the upper HRD from K2 and TESS space photometry by Pedersen et al. (2019) and Bowman et al. (2019b) granted them an ellipse in Fig. 1 labeled as “SLF” for stochastic low-frequency variability.

Gautschy & Saio (1995, 1996) announced that the importance of nonradial oscillation studies would grow as monitoring capacities to detect ever smaller amplitude variability would improve: a visionary outlook a few years before space asteroseismology came about with WIRE. Figure 1 shows that stars across almost the entire mass range will encounter nonradial oscillations at particular stages of their evolution. The characteristics of these nonradial oscillation modes (their periods or frequencies, amplitudes, and mode lifetimes) offer great diagnostic value for inferences of the stellar interior. As outlined in detail in Sec. II, the mode frequencies or periods allow high-precision views of the physical properties inside stars that are not accessible by classical “snapshot-type” data assessing only the surface or atmospheric properties at a particular time of the variability cycle (such as single-epoch spectroscopy, color indices, or interferometry). The combination of high-cadence time-series data covering the overall pulsational variability cycle,

along with observables representing the position in the HRD ($T_{\text{eff}}, L/L_{\odot}$) and surface abundances from spectroscopy, constitute an optimal starting point for asteroseismic modeling. The power of combining such a classical and asteroseismic approach for stellar modeling was illustrated by Lebreton et al. (2014) in their Fig. 13, with major improvement for stellar aging. In practice, the addition of asteroseismology to stellar modeling permits to reach levels of $\sim 10\%$ precision in stellar ages. Precise values for the stellar luminosity L or the stellar radius R_{\star} of low- and intermediate-mass stars can now be obtained from Gaia astrometry (Gaia Collaboration, Brown et al., 2018) and interferometry, respectively. Following the extensive review on how to bridge asteroseismology and interferometry by Cunha et al. (2007), this synergy turns out to be highly successful for the brightest pulsators with space asteroseismic data, as highlighted by North et al. (2007), Bazot et al. (2011), Huber et al. (2012), White et al. (2013), and White et al. (2018).

To conclude this section, nonradial oscillations occur all over the HRD. This offers the exciting opportunity to perform asteroseismology for members of the classes indicated in Fig. 1 and to couple the conclusions into a coherent picture across stellar evolution. Such a meta-study has been done for asteroseismic estimates of the interior rotation of low- and intermediate-mass stars, leading to the conclusion that the theory of angular momentum transport in stellar interiors already needed improvements from the earliest stages of stellar evolution. We come back to this in Sec. III but stress here that a global perspective of stellar evolution across all life phases proved to be necessary to assess the weaknesses of one particularly important aspect of stellar evolution theory: the transport of angular momentum is much more efficient than predicted by theory (see Fig. 4 in Aerts et al., 2019, which summarizes a global result based on major efforts by many scientists in the asteroseismology community). This is just one example of how asteroseismology paves the way towards better stellar evolution models. Data are now being assembled by the TESS mission to reach the same impact for high-mass stars. For the rest of this review, we adopt the same definition as Aerts et al. (2019) to discriminate between stars of low ($M_{\star} \lesssim 1.3 M_{\odot}$), intermediate ($1.3 \lesssim M_{\star} \lesssim 8 M_{\odot}$), and high ($M_{\star} \gtrsim 8 M_{\odot}$) mass.

D. Working in the Fourier domain truly helps

Figure 3 is a textbook illustration of how stars of intermediate mass exhibiting g modes behave in flux as their interior rotation increases (from top to bottom in the plot). We explain in Sec. II how to arrive at such a conclusion about their interior rotation, but for now the message is that this result cannot be “seen” easily in the time domain (i.e., in the light curve in gray), while it can

be directly distilled from the Fourier spectrum overplotted in red. It is amazing how much information about the stellar interior is contained in a Fourier transform of a light curve: the art is to get it out, and asteroseismologists are experts in this regard.

We see in Fig. 3 that the duty cycle of the *Kepler* data is high, but not 100%, because the satellite had to be turned every three months to keep its solar panels pointed to the Sun. Moreover, one-month data downlink and momentum dump desaturation interruptions occurred approximately every 3 d. Moreover, the *Kepler* photometer consisted of 21 CCD modules (Koch et al., 2010), but one of them (Module 3) broke down less than a year into the mission, causing gaps in the data for stars on that module. The *Kepler* spacecraft sampled the stars at a constant cadence, delivering data at precise time stamps. The data are modulated with 1-yr periodicity when transformed to the barycenter of the Solar System (Murphy et al., 2013b). Given that stellar oscillations are periodic because they occur at the “eigenfrequencies” of the star, Fourier analysis offers an optimal frequency extraction method. It is extensively described in Chap. 5 given by Aerts et al. (2010) in the general case of nonequidistant gapped time series of ground-based data. An excellent crash course on the topic was given by Apourchaux (2014), who tuned it to the modern era of space asteroseismology, while the effect of interruptions in the *Kepler* light curves on the frequency analysis for asteroseismology was thoroughly assessed by García et al. (2014). Basu & Chaplin (2017) provided even more detailed information and focused on data analysis in the case of solarlike oscillations. Here we limit ourselves to the bare minimum and pay specific attention to the aspects of time-series analysis from the viewpoint of having two major categories of nonradial oscillation modes: those that are damped and have short lifetimes and those that are undamped and, to a good approximation, have infinite lifetimes. These two cases require different data analysis approaches.

As explained later, the three components of the Lagrangian displacement vector due to a nonradial oscillation mode in the absence of rotation contain a common time-dependent factor $\exp(-i\omega t)$, with $\omega = 2\pi\nu$ the angular frequency of the mode, ν its cyclic frequency and $P = 2\pi/\omega = 1/\nu$ its period. In general, ω is an imaginary quantity $\omega = \omega_r + i\omega_i$, but for the study of the periodic behavior of the mode to be derived from data we consider its real part (for simplicity denoted as ω in the rest of the review). Imagine that we want to extract the frequencies present in time-series data representing a continuous and finite function $x(t)$ (the flux variations in the case of space asteroseismology, indicated with the black dots in Fig. 3). The Fourier transform of $x(t)$ is

given by

$$F(\nu) \equiv \int_{-\infty}^{+\infty} x(t) \exp(2\pi i \nu t) dt. \quad (1)$$

By performing this transformation, we move from the time domain (black dots in Fig. 3) to the frequency domain (shown in red in Fig. 3). In the following case where $x(t)$ is a sum of harmonic functions with frequencies ν_1, \dots, ν_M and amplitudes A_1, \dots, A_M :

$$x(t) = \sum_{k=1}^M A_k \exp(2\pi i \nu_k t), \quad (2)$$

we find that

$$F(\nu) = \sum_{k=1}^M A_k \delta(\nu - \nu_k), \quad (3)$$

where δ is Dirac's delta function for which $\delta(\nu - \nu_k) \neq 0$ only for the frequencies $\pm\nu_1, \dots, \pm\nu_M$. No matter how good the *Kepler* data are, the time series (1) contains discrete data points, (2) has finite duration, and (3) has gaps (even if they are small). This implies that one cannot compute the integral in Eq. (1). However, we can rely on the so-called window function defined by the data, measured at time points $t_j, j = 1, \dots, N$ during the time interval $[0, T]$ to obtain:

$$w_N(t) \equiv \frac{1}{N} \sum_{j=1}^N \delta(t - t_j). \quad (4)$$

This allows us to write the Discrete Fourier Transform (DFT) of the function $x(t)$ as

$$F_N(\nu) = N \int_{-\infty}^{+\infty} x(t) w_N(t) \exp(2\pi i \nu t) dt. \quad (5)$$

The following DFT of the window function is called the spectral window $W_N(\nu)$:

$$W_N(\nu) = \frac{1}{N} \sum_{j=1}^N \exp(2\pi i \nu t_j). \quad (6)$$

The DFT of the data is hence the convolution of its spectral window and its Fourier transform

$$\begin{aligned} F_N(\nu) &= N(F * W_N)(\nu) \\ &= \sum_{j=1}^N x(t_j) \exp(2\pi i \nu t_j) \Delta t_j, \end{aligned} \quad (7)$$

where $\Delta t_j \equiv t_j - t_{j-1}$ (Deeming, 1975). Frequencies are often searched from the power density (PD) instead of the Fourier transform. The PD is defined as the power present in the signal as a function of frequency, per unit frequency. Relying on Eq. (7), we get

$$\text{PD}(\nu) \equiv \frac{1}{T} |F_N(\nu)|^2. \quad (8)$$

The PD is hence expressed in $\text{ppm}^2/\mu\text{Hz}$ when the time series concerns flux measurements expressed in ppm and frequencies are expressed in microhertz.

For equidistant data, $t_j = j \cdot \Delta t$, where $\Delta t_j = \Delta t$ is a constant sampling interval between two consecutive measurements. In that case, we have

$$F_N(\nu) = \Delta t \cdot \sum_{j=1}^N x(j\Delta t) \exp[2\pi i \nu(j\Delta t)] \quad (9)$$

$$W_N(\nu) = \exp(\pi i \nu \Delta t(N+1)) \frac{\sin(\pi \nu N \Delta t)}{N \sin(\pi \nu \Delta t)}. \quad (10)$$

The Nyquist frequency of such data is half of the sampling rate $\nu_{\text{Ny}} = 1/2\Delta t$. This frequency is defined as the upper limit of the frequency range over which the Fourier transform is unique. In principle this sets an upper limit for the interval of frequencies to search for. However, a particular frequency detected below ν_{Ny} may be an alias of the true frequency that occurs above ν_{Ny} . Alias frequencies are frequency values given by the difference between the actual frequency of the signal and integer multiples of the sampling rate. Thus, aliasing allows the detection of true frequencies, even though they occur above ν_{Ny} (Murphy et al., 2013b).

Equations (9) and (10) reveal that $F_N(\nu)$ reaches maxima for alias frequencies $\nu_j = j/\Delta t$. Ground-based data are not evenly sampled but they give rise to 1-d and 1-yr alias frequencies whose values of $F_N(\nu_j)$ may be similar, preventing from unraveling the “true” frequency from the one introduced by the periodic gaps in the data. This has been a major show-stopper for ground-based asteroseismology, particularly in the case of stars with “slow” g modes with periods of approximately 1 d as in Fig. 3. While these g modes have amplitudes that are easily detectable with ground-based instruments, the 1-d aliasing problems are so severe that one can deduce a few mode frequencies at best, even after yearslong (often multisite) observations; see e.g. Zerbi et al. (1999), De Cat & Aerts (2002), Mathias et al. (2004), and Cuypers et al. (2009). This is why *Kepler* was so groundbreaking in the field of slow multiperiodic g-mode pulsators. *Kepler* data also revealed that a good fraction of dwarf pulsators with a convective core (indicated as γ Dor, δ Sct, SPB, and β Cep stars in Fig. 1) are actually hybrid pulsators; i.e., they have both short-period (lasting hours) p modes and long-period (lasting days) g modes. Such pulsators have major potential, as their p and g modes offer local *in situ* measurements in different regions in the star: p modes probe the envelope, while g modes probe the radiative near-core regions and allow us to turn the study of deep stellar interiors into observational astronomy.

In practice, applications of frequency analysis to space photometric data are always done after preprocessing and postprocessing of the light curves deduced from the raw data. Satellite repointings (every three months in the case of *Kepler*, so-called quarters) imply jumps in the

time series. Moreover, satellite drift has to be corrected for each quarter. Subsequently, outlier removal and detrending are applied as standard processing to get interpretable light curves (García et al., 2011). Such corrections and processing were applied to get the light curves in the version shown in Fig. 3.

1. Mode damping and mode lifetimes

Thus far we have considered a multiperiodic harmonic signal. For stars like those in Fig. 3, this is relatively straightforward because they have modes with extremely long lifetimes. However, a distinction has to be made between two cases: damped modes with lifetimes of the order of or shorter than the duration of the time series T and undamped (or so-called self-excited) modes that never die out and are always active with constant phase throughout the data gathering. The first option occurs for stars such as the Sun with oscillation modes triggered by turbulent motions in their outer convective envelope. Such “solarlike” oscillations are expected to occur for all stars whose convective envelopes contain sufficient mass to be highly turbulent. These oscillations are of stochastic nature in the sense that they are regularly but randomly excited to more or less the same amplitude but they damp out relatively quickly, in a time span on the order of days to months, while continuously being re-excited. At each time stamp, the phase within the oscillation cycle is perturbed stochastically relative to the previous measurements.

Stars with radiative envelopes can excite oscillations via a heat mechanism, because some of their partial ionization layers manage to transform radiative energy, created in their deep interior by nuclear fusion, into mechanical energy. This can excite modes that resonate inside a mode cavity. This occurs because of local opacity peaks in partial ionization layers of hydrogen, helium, or iron-like species in the outer envelope. Such mode excitation works along the lines of a valve mechanism (also known as thermodynamical Carnot cycle) and may excite radial and nonradial oscillation modes. Because of the key role played by the opacity in getting the modes excited, it is usually called the κ mechanism. To a good approximation such resonating modes do not die out as long as radiative energy is delivered to the excitation layer. Hence these modes have “quasi-infinite” lifetimes (i.e. they are infinite to a good approximation compared to the duration of the dataset; hence we drop “quasi” in the text). In such a case, it is predictable at what phase in its oscillation cycle the mode will be throughout time.

We return to mode excitation in Sec. III but in any case we take a data-driven approach to asteroseismology; i.e., we use as many independent eigenmode frequencies as possible, as long as we can extract them from the data, irrespective of how the star managed to excite these

oscillations.

2. Undamped oscillations with quasi-infinite lifetimes

We first treat the case of heat-driven undamped modes. In this case [see Eq. (3)] we seek to extract the optimal sum of harmonic functions with frequencies ν_1, \dots, ν_M and amplitudes A_1, \dots, A_M , where the number of modes M is unknown, keeping in mind the presence of instrumental noise in the data. Under the optimistic assumption of uncorrelated data with white Gaussian noise, a convenient approximation of the Fourier transform is the Lomb-Scargle (LS) periodogram, defined as

$$P_{\text{LS}}(\nu) = \frac{1}{2} \frac{\left\{ \sum_{i=1}^N x(t_i) \cos[2\pi\nu(t_i - \tau_0)] \right\}^2}{\sum_{i=1}^N \cos^2[2\pi\nu(t_i - \tau_0)]} + \frac{1}{2} \frac{\left\{ \sum_{i=1}^N x(t_i) \sin[2\pi\nu(t_i - \tau_0)] \right\}^2}{\sum_{i=1}^N \sin^2[2\pi\nu(t_i - \tau_0)]}, \quad (11)$$

where τ_0 is chosen such that $P_{\text{LS}}(\nu)$ becomes invariant with respect to the starting date of the dataset:

$$\tan(4\pi\nu\tau_0) = \frac{\sum_{i=1}^N \sin(4\pi\nu t_i)}{\sum_{i=1}^N \cos(4\pi\nu t_i)} \quad (12)$$

(Scargle, 1982). Along with the DFT, the LS periodogram is widely used in asteroseismology of stars with heat-driven modes. Both formalisms are suitable to treat gapped nonequidistant time-series data while requiring only a short computation time (Kurtz, 1985). Horne & Baliunas (1986) provide guidance for estimation of the number of independent frequencies as well as a method for detecting the presence of alias frequencies caused by the interaction between the window function and the observed data values. In the limit of $N \rightarrow \infty$, one has $P_{\text{LS}}(\nu_k) \approx A_k^2 N/4$ for each of the modes $k = 1, \dots, M$. The LS amplitude spectrum $A_{\text{LS}}(\nu) \equiv \sqrt{4P_{\text{LS}}(\nu)/N}$ thus gives the physically relevant quantities to perform asteroseismology, i.e., the frequencies and amplitudes of the modes. This is the amplitude spectrum shown in red for the seven B-type pulsators in Fig. 3.

Scargle (1982) showed the maxima of $A_{\text{LS}}(\nu)$ to lead to amplitudes A_k that are statistically equivalent to those obtained by performing a least-squares optimization to the light curve in the time domain in the limit of large N . Even modern datasets may consist of only a limited

number of data points. One therefore best performs an optimization to estimate the amplitudes and frequencies once an approximate value of ν_k is known from the DFT or LS periodogram, as a good starting value to perform a least-squares fitting in the time domain. This gives rise to the method of “prewhitening.”

We now consider the dominant mode with frequency ν_1 deduced from the DFT or LS amplitude spectrum. Minimizing the sum of squares of the residuals,

$$R^2(\nu_1) \equiv \sum_{i=1}^N [x(t_i) - x^c(t_i)]^2 \quad (13)$$

$$= \sum_{i=1}^N \{x(t_i) - \{A_1 \cos \{2\pi [\nu_1(t_i - \tau) + \psi_1]\} + c\}\}^2$$

leads to optimized values for ν_1, A_1, ψ_1 , and c , and provides the residual light curve with an average value of zero

$$x_R(t_i) = x(t_i) - x^c(t_i). \quad (14)$$

A second frequency is then searched for by computing the LS amplitude spectrum for the residual light curve $(t_i, x_R(t_i))$ and optimizing its values ν_2, A_2, ψ_2 , etc. This procedure is repeated until the periodogram no longer leads to frequencies that are significant for a specified criterion, such as the ones discussed in Horne & Baliunas (1986), Breger et al. (1993), and Degroote et al. (2009). For a *Kepler* light curve, this procedure is tedious and time consuming as it leads to hundreds of significant frequencies. To finalize the list of frequencies due to independent oscillation modes and their uncertainties, great care must be taken to properly account for the occurrence of combination frequencies and harmonics $r\nu_i + s\nu_j$ with $i, j \in \mathbb{N}; r$ and $s \in \mathbb{Z}$ due to nonlinearities in the light curve rather than independent mode frequencies, keeping in mind the spectral window and the introduction of spurious frequencies due to limited time resolution (Loumos & Deeming, 1978) during the prewhitening process. This was thoroughly discussed by Pápics (2012), Balona (2014), Kurtz et al. (2015), and Bowman (2017). Moreover, one should correct the error estimation of the frequencies and their amplitudes for the correlated nature of the data (e.g., as outlined in Degroote et al., 2009, for the highly oversampled CoRoT data). Although this correction is often omitted, one should apply it to the error estimates of the derived amplitudes, phases, and frequencies. For the case of N data points, one has (see Montgomery & O’Donoghue, 1999):

$$\sigma_\nu = \frac{D\sqrt{6}\sigma_N}{\pi\sqrt{N}AT}, \quad \sigma_A = D\sqrt{\frac{2}{N}}\sigma_N, \quad \sigma_\psi = \frac{D\sigma_N}{\pi\sqrt{2NA}}. \quad (15)$$

In these three expressions, σ_N can be approximated by the standard deviation of the final residual light curve. The correction factor due to the correlated nature of the

data D depends on the instrument properties and the sampling rate and can be estimated as the square root of the average number of consecutive data points of the same sign in the final residual light curve, as explained in Schwarzenberg-Czerny (1991) and applied to ground-based photometry by Schwarzenberg-Czerny (1998) and to space photometry by Degroote et al. (2009). Values for D are typically between two and ten for the *Kepler* long-cadence and CoRoT asteroseismology data sets.

3. Damped oscillations with short lifetimes

The frequency analysis for stochastically excited damped solarlike oscillations requires a different approach. Because of the random excitation and the damping of the modes, the functional form of the light curve changes. The simplest case of one damped oscillation mode with frequency ν_1 can be described as

$$x(t_i) = A_1 \cos [2\pi(\nu_1 t_i + \psi_1)] \exp(-\eta_1 t_i) + c, \quad (16)$$

with η_1 the damping rate of the mode, which is the inverse of the mode lifetime. The latter is unknown and hence must be estimated along with the frequency. In the hypothetical case of having continuous observations of such a signal over an infinite amount of time, the power spectrum is given by

$$P(\nu) = \frac{1}{4} \frac{A_1^2}{(4\pi^2(\nu - \nu_1)^2 + (\eta_1)^2)}. \quad (17)$$

In such a simplified (actually, unrealistic) case, the power spectrum thus takes a Lorentzian profile around the frequency ν_1 with the linewidth of the mode given by the full width at half maximum $\Gamma \equiv 2\eta_1/2\pi$. Estimation of Γ can be accompanied by major uncertainty, unless long and high-quality datasets, such as those assembled by *Kepler*, are available.

Solar-like oscillation frequencies are usually superimposed onto background power due to low-frequency variability caused by the convective envelope of the star, such as granulation and/or magnetic activity leading to rotational modulation. Stellar granulation occurs in stars with outer convection zones due to the difference between hotter rising gas and cooler downward moving gas. Rotational modulation observed in light or velocity curves is attributed to starspots on the stellar surface, which can have a different temperature, pressure, or chemistry than their surroundings. When the spots have properties that are slowly evolving with time compared to the rotation period, they give rise to rotational modulation at the frequency of the surface rotation and its (sub)harmonics. However, the spots may migrate and/or vary in size over time, leading to low-frequency power excess in the Fourier spectrum.

Both granulation and spots may reach amplitudes that are dominant over those of the oscillations. Any Fourier

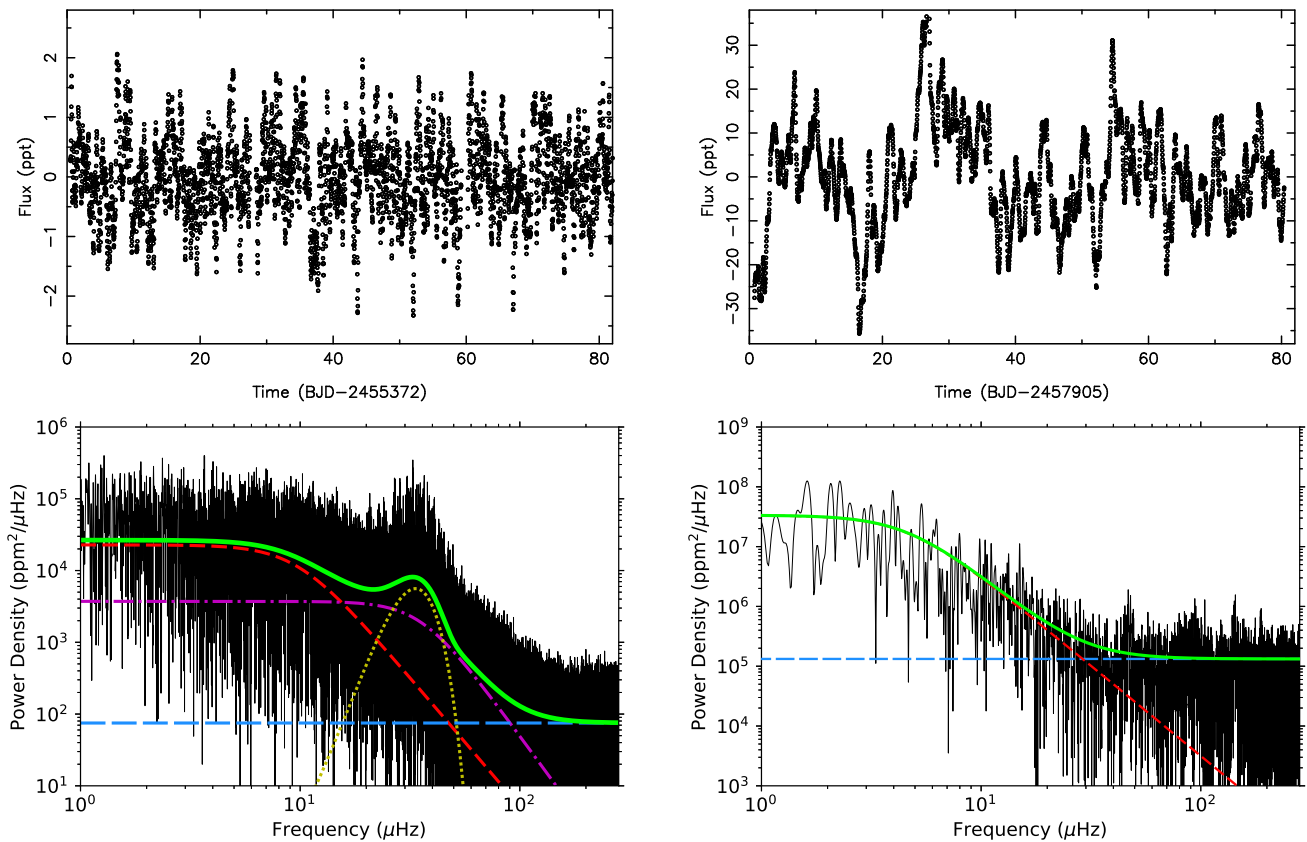


FIG. 4 Part of the *Kepler* light curve (top left panel) and the power density spectrum (bottom left panel, black) of the red-giant star KIC 007949599. Overplotted in the bottom left panel are the model fits from Table 1 given by Kallinger et al. (2014) based on their Eq. (2), representing two Lorentzian components due to granulation variability at low frequencies (dashed red and dot-dashed purple lines) and a Gaussian component due to stochastic p-mode oscillations (dotted yellow line). K2 light curve (top right panel) and its power density spectrum (bottom right panel, black) of the blue supergiant star ρ Leo. Overplotted in the bottom right is a Lorentzian model fit (dashed red line) using the formalism given by Bowman et al. (2019a) to represent the power excess due to the low-frequency stochastic variability. In both bottom panels, the blue dashed horizontal lines indicate the photon noise level and the green lines represent the superposition of the individual model components representing the variability. Figure based on data from Kallinger et al. (2014) and from Aerts et al. (2018a), by courtesy of Dominic Bowman, KU Leuven.

transform of a light curve undergoing these various aspects of variability will be composed of the superposition of all the harmonic and nonharmonic signals. In such a situation, the method of prewhitening is not meaningful due to the stochastic nature of the variability. Rather, one works with the PD and fits this to extract the oscillation frequencies. In Eq. (17) we have assumed for simplicity that the mode linewidth is independent of frequency. However, it may vary with frequency according to some functional form depending on the mode properties, as discussed for mixed modes in red giants by Mosser et al. (2018).

Different models to describe the oscillation modes and the overall “background” variability were developed and improved as the *Kepler* data got extended. Kallinger et al. (2014) investigated the PD of a large and homogeneous sample of 1364 stars observed with

the *Kepler* spacecraft, covering almost all evolutionary stages of stars born with a mass between approximately 0.7 to $2.5 M_{\odot}$. All these stars are expected to exhibit stochastically excited oscillations and granulation triggered by their extended convective outer envelope. Hence, Kallinger et al. (2014) searched for one global optimal fitting prescription for the background variability, instead of relying on the background model used for the Sun and adopted in red-giant studies based on early *Kepler* data releases (e.g., Mathur et al., 2011). Kallinger et al. (2014) considered various options for the statistical model formulations of the PD spectra; see their Eq. (2) and Table 1. In line with the findings of Karoff et al. (2013) for main-sequence stars, the optimal fits to the PD spectra of bright red-giant pulsators require more than one Lorentzian profile to describe the granulation/activity, in addition to a Gaussian power excess

caused by oscillations. This is illustrated for one of the red giants in their sample in Fig. 4, where we show the *Kepler* light curve in the upper left panel, revealing the stochasticity of the variability and the PD in the lower left panel.

Bastien et al. (2013) revealed that the scaling of the granulation amplitude delivers a proper diagnostic for the surface gravity g of the star. The scaling was found to be consistent with that of the pulsation amplitudes. Moreover, the effective temperature has only a marginal additional effect on those amplitudes. This brings us to an important quantity in low-mass star asteroseismology that is further outlined in Sec. IV: the frequency of maximum power ν_{\max} . This quantity was shown to scale to a good approximation as $g \cdot T_{\text{eff}}^{-1/2}$ by Brown & Gilliland (1994), Kjeldsen & Bedding (1995), and Belkacem et al. (2011). It can be deduced from the Gaussian fit represented by the yellow dotted line in Fig. 4.

Any asteroseismic modeling requires the oscillation frequencies of the damped modes to be extracted from the PD. Various methods and implemented pipelines to do so have been constructed. As said, one does not rely on the method of prewhitening to achieve this. Instead so-called peak-bagging³ is done, where the part of interest in the PD is fit with Lorentzian functions for each of the modes as in Eq. (17), either after subtraction of or along with the fit to the granulation background. These methods result in the individual mode frequencies and the mode lifetimes from the linewidths in the PD. Extensive literature covers the methodologies, where the use of an Markov Chain Monte Carlo (MCMC) technique was adopted in this context by Handberg & Campante (2011). Intercomparison of the results obtained by the various methods is taken into account as part of the uncertainties of the mode frequencies, amplitudes, and lifetimes; see Hekker et al. (2011, 2012) and Appourchaux et al. (2012a,b). Particular care of the correlation structure in the frequency analysis of exoplanet host stars was taken using a Bayesian unsupervised approach developed by Davies et al. (2016).

The *Kepler* observations led to numerical refinements and testing of early analytical expressions for uncertainty estimates of the frequencies of stochastic modes, confirming that they behave as $\sim 1/\sqrt{T}$ (see Eqs. (5.57) in Aerts et al., 2010) instead of $\sim 1/T$ as in Eqs. (15). To get a factor of 2 better frequency precision for damped oscillations one must hence observe 4 times as long as opposed to 2 times as long in the case of undamped modes. For elaborate discussions on how the mode linewidths of

p modes were derived from *Kepler* light curves for dwarfs, subgiants, and red giants, see Chaplin et al. (2009), Appourchaux et al. (2012a), Corsaro et al. (2015), and Vrard et al. (2018). Values translate into mode lifetimes from a fraction of a day for dwarfs to several tens of days for red giants, in good agreement with theoretical predictions by Belkacem et al. (2012). Mosser et al. (2018) succeeded in deriving the mode lifetimes for the challenging case of mixed dipole modes in red giants, with results up to ~ 100 d. Chaplin et al. (2014) and Yu et al. (2020) contain summaries of results for about 500 main-sequence stars and 20000 red giants observed with the *Kepler* spacecraft, respectively.

To place the stochastic variability of evolving low-mass stars into a more global context, stochastic low-frequency (indicated as SLF in Fig. 1) variability was also found to occur in high-mass stars, but for different physical reasons. While all stars develop a convective outer envelope after core-hydrogen burning, young high-mass stars are born with a radiative envelope on top of a convective core. Hence, one does not expect granulation to be present in their envelope. As originally discovered from CoRoT data, young hot O stars reveal SLF in their PD spectra (Blomme et al., 2011). This signature is different from the frequency spectrum for p-mode oscillations in β Cep stars (see Fig. 1) as found for the O9V CoRoT target HD 46202 (Briquet et al., 2011) in the same pointing of the satellite from which the SLF signal was found, so an instrumental cause was excluded. Tkachenko et al. (2014) and Aerts & Rogers (2015) interpreted the signal detected in the space photometry of the close massive binary V380 Cyg and of the O dwarfs as due to convectively driven IGWs. These waves are excited stochastically at the interface between the convective core and the bottom of the radiative envelope in intermediate- and high-mass stars (Rogers et al., 2013). The simulations by Edelman et al. (2019) and Horst et al. (2020) are representative for young unevolved stars of high mass and deliver frequency spectra of IGWs and eigenmodes as observed in dwarfs with CoRoT and *Kepler* for stars with masses in the range $[3, 25] M_{\odot}$.

Bowman et al. (2019a,b, 2020) performed a systematic study of OBA-type stars from their CoRoT, K2, and TESS data to search for SLF, keeping in mind that such a signal is hard to find when it occurs beneath the signal of self-excited modes in the same frequency regime, as for stars in Fig. 3. It was found that SLF variability is ubiquitous in space photometry of most of these stars, irrespective if they reside in the Milky Way or in the Large Magellanic Cloud. The K2 light curve and PD spectrum of one such case is shown in the right panels of Fig. 4. It concerns the bright blue supergiant ρ Leo (spectral type B1Iab) studied by Aerts et al. (2018a) and Pope et al. (2019) at different levels of sophistication. The fit to the PD spectrum of ρ Leo shown in Fig. 4 reveals a characteristic frequency $\nu_{\text{char}} = 16.624 \pm 0.007 \mu\text{Hz}$, corresponding

³ This term became standard use in helioseismology and asteroseismology after champion “peak bagger” Jesper Schou made the analogy between the detection of new solar oscillation frequencies in data obtained with the SoHO satellite and the addition of newly climbed +14 000 feet summits to his personal bag-pack.

to a characteristic timescale of 0.7 d. The K2 light curve of ρ Leo also reveals rotational modulation with a period of 26.8 d (Aerts et al., 2018a), which corresponds to a frequency of $0.432\mu\text{Hz}$. The astrophysical interpretation of SLF in intermediate- and high-mass stars may involve a variety of physical causes given the wide range of evolutionary stages covered by the sample.

Armed with the knowledge of how to derive the oscillation frequencies, $\omega_{nlm}^{\text{obs}}$, of a pulsating star from high-precision space photometry, we now move on to their exploitation in terms of the star’s interior physical properties. This requires that we dive into the theory of nonradial oscillations predicted from equilibrium models of stars. In the next two sections, we explain how this can be achieved and under which assumptions. Subsequently we summarize some of the impressive recent results of asteroseismic modeling.

II. NONRADIAL OSCILLATIONS OF STARS

The diagnostic power of nonradial oscillations to probe stellar interiors is immense, particularly when compared to observations that probe only the stellar atmosphere. For example, estimates of T_{eff} of slowly rotating single stars are dependent on atmosphere models and may reach 1% precision for the best cases. Dynamical masses of binary components are model-independent observables and may reach 1% accuracy (see Serenelli et al., 2021, for a summary). Oscillation frequencies can be measured directly from data, without any model dependence, at the level of 0.001% for p modes of low-mass stars and 0.1% for g modes of intermediate-mass stars (Aerts et al., 2019, Table 1). These precisions of mode frequencies lie at the heart of the revolution brought by space asteroseismology.

The interpretation of detected oscillation modes requires a good understanding of the theory of nonradial oscillations and how the modes depend on the properties of stellar interiors. This dependence is currently studied from numerical computations of stellar equilibrium models and their predicted oscillations, for different sets of input physics and free parameters. However, various forms of analytical expressions for the mode properties are highly insightful for the understanding of the mode behavior. In fact, asymptotic approximations of the mode frequencies offer an important basis to interpret the observations, even in current times of large computational power. This was stressed by Cunha et al. (2015) and illustrated by Van Reeth et al. (2016), Ouazzani et al. (2017), Christophe et al. (2018), and Cunha et al. (2019b).

Extensive textbooks on the theory of nonradial oscillations of stars were produced by Unno et al. (1989) and Smeyers & Van Hoolst (2010), to which we refer for the historical developments and for mathematical deriva-

tions. Here we limit ourselves to the bare minimum required to understand applications of asteroseismology. Aerts et al. (2010) provided detailed descriptions of the general methodology and applications covering all masses and types of nonradial oscillations, while Basu & Chaplin (2017) covered applications based on space photometry but limited to stochastically excited solarlike oscillations. Tong & García (2015) covered synergies between planetary and stellar seismology. As outlined in the Introduction, the asteroseismology revolution of the past decade is so immense that we focus the rest of this review on applications based on the recent space photometry, even though this does injustice to numerous studies and efforts prior to 2010.

A. Stars and their hydrodynamics

The equations describing the oscillations of stars are perturbed versions of the equations of hydrodynamics applied to a gaseous self-gravitating sphere. We introduce the basics of stellar hydrodynamics before moving on to stellar oscillations. We omit the derivation of these basic equations here, as this is the topic of various books on fluid dynamics. A seminal introduction to hydrodynamics with specific attention to stellar oscillations was given by Ledoux & Walraven (1958). Here we limit ourselves to the ingredients needed to move on to asteroseismic modeling while omitting unnecessary details.

1. The stellar structure equations

The equations to be solved to compute stellar models throughout the evolution of stars are the general equations of physics, expressing conservation of mass, momentum, and energy. In stellar interiors, the circumstances are such that viscosity can be ignored and the conservation laws can be limited to gaseous objects. The derivation of the equations expressing the conservation laws for stellar structure and evolution was covered by Cox & Giuli (1968), Hansen et al. (2004), Maeder (2009), and Kippenhahn et al. (2012).

Conservation of mass leads to the equation

$$\frac{\partial \rho}{\partial t} + \nabla \cdot (\rho \mathbf{v}) = 0, \quad (18)$$

where $\rho(\mathbf{r}, t)$ is the local density at position vector \mathbf{r} and $\mathbf{v}(\mathbf{r}, t)$ the local velocity vector, both at time t . The equations of motion, expressing conservation of momentum, can be written as

$$\rho \frac{\partial \mathbf{v}}{\partial t} + \rho \mathbf{v} \cdot \nabla \mathbf{v} = -\nabla p - \rho \nabla \Phi + \rho \mathbf{f}, \quad (19)$$

where \mathbf{f} is body force per unit mass and Φ is the gravitational potential satisfying the Poisson equation

$$\nabla^2 \Phi = 4\pi G \rho, \quad (20)$$

and where it is assumed that internal friction in the gas can be ignored (i.e., zero viscosity). In general, \mathbf{f} stands for the electromagnetic and possibly external forces such as tidal forces in multiple systems. The energy equation is derived from the thermodynamical properties and the energetics of the gas and can be formulated as

$$\rho T \frac{\partial S}{\partial t} + \rho T \mathbf{v} \cdot \nabla S = \rho \varepsilon - \nabla \mathbf{F}, \quad (21)$$

with S the entropy per unit mass, ε the energy generation rate per unit mass taking into account the energy loss from neutrinos, and \mathbf{F} the energy flux.

Further, an equation for the overall energy transport throughout the star needs to be added. This is fairly straightforward in radiative zones of the star, because the mean free path of a photon is ultrashort compared to the length scales over which the stellar structure changes (~ 2 cm in the solar interior, for instance). In such a case the radiative energy transport is well described by a diffusion approximation. For stellar interiors, this is given by

$$\mathbf{F} = -\frac{4\pi}{3\kappa\rho} \nabla B = -\frac{4acT^3}{3\kappa\rho} \nabla T, \quad (22)$$

where $B = (ac/4\pi)T^4$ results from integrating Planck's radiation function, κ is the flux-weighted opacity, c is the speed of light, and a is the radiation density constant.

In convection zones of the stellar interior, the turbulent gas motions transport the energy in an efficient yet complex manner. In the absence of a proper theory for the dynamical effect of convection for stellar interiors, the turbulent pressure is usually ignored and the treatment of convective energy transport in stellar evolution codes is time-independent. This approach is a crude approximation; it is based on pragmatism rather than sophistication. Although various versions exist for the description of convective instabilities, the most popular treatment of time-independent convection is the so-called mixing-length theory (mlt, see Houdek & Dupret, 2015, for a historical overview). It is characterized by the free parameter α_{mlt} (expressed in units of the local pressure scale height H_p), which stands for the mean free path over which the convective eddies travel before dissolving in their environment. Asteroseismology allows one to infer the extent of convective regions via estimation of the free parameters of the convection formulation used for the modeling. This was done for mlt by Joyce & Chaboyer (2018) and Viani et al. (2018).

Whenever the diffusion of photons is insufficiently efficient as an energy transport mechanism, convection not only takes over the energy transport, but it also changes the temperature gradient relative to the radiative one in Eq. (22). From a computational point of view, the calculation of the energy transport must hence be split up for the radiative and convective zones inside the stellar

model. This is done by testing whether a zone with temperature gradient

$$\nabla \equiv \frac{d \ln T}{d \ln p} \quad (23)$$

is stable or unstable against convection. The general condition to test for convective stability is the so-called Ledoux criterion

$$\nabla_{\text{rad}} < \nabla_{\text{ad}} + \frac{\varphi}{\delta} \nabla_{\mu}, \quad (24)$$

where we have introduced

$$\nabla_{\text{rad}} = \frac{3}{16\pi acG} \frac{\kappa p}{T^4} \frac{L(r)}{m(r)}, \quad \nabla_{\text{ad}} = \left(\frac{\partial \ln T}{\partial \ln p} \right)_S,$$

$$\nabla_{\mu} = \frac{d \ln \mu}{d \ln p}, \quad \delta = - \left(\frac{\partial \ln \rho}{\partial \ln T} \right)_{p,\mu}, \quad \varphi = \left(\frac{\partial \ln \rho}{\partial \ln \mu} \right)_{p,T},$$

with μ the mean molecular weight of the ionized gas. For zones with a homogeneous chemical composition, the Ledoux criterion reduces to the Schwarzschild criterion

$$\nabla_{\text{rad}} < \nabla_{\text{ad}}. \quad (25)$$

Stars born with a mass above $\sim 1.7 M_{\odot}$ have a receding convective core as they evolve throughout the core hydrogen-burning phase because the opacity κ decreases as the hydrogen depletes, reducing ∇_{rad} . The resulting composition gradient gives rise to $\nabla_{\mu} \neq 0$ and increases stability in that zone. On the other hand, the change of ∇_{rad} for stars born with a mass below $\sim 1.3 M_{\odot}$ is dominated by the factor $L(r)/m(r)$, which increases faster than κ decreases. The interplay in importance between κ and $L(r)/m(r)$ in the expression of ∇_{rad} , and along with it the growth or shrinkage of the convective core, depends on the physical circumstances for masses between 1.3 and $1.7 M_{\odot}$ (e.g., Mombarg et al., 2019).

In a zone that is stable against convection, a fluid element that gets displaced by moving up will be pulled back down until it is again situated at its equilibrium position, thanks to the action of the buoyancy force of Archimedes. This oscillatory motion of the fluid elements depends on the local density, pressure, and chemical composition of the gas and happens with the so-called Brunt-Väisälä frequency, or buoyancy frequency for short, which can be approximated as

$$N^2 \simeq \frac{g}{H_p} [\delta (\nabla_{\text{ad}} - \nabla) + \varphi \nabla_{\mu}], \quad (26)$$

with g the local gravity. The μ -gradient affects the local behavior of $N(r)$ in the radiatively stratified layers of the star. As discussed later, this will affect stellar oscillations, notably internal gravity waves. In the case of instability, i.e. $N^2 < 0$, the speed of the fluid element

increases exponentially with time until it breaks up, causing complete and instantaneous mixing of the chemical species.

Even though Eq. (24) allows us to derive the zones where convection takes place inside the star, complications occur in the transition layers between convective and radiative zones, hereafter termed convective boundary layers. The fluid elements inside a convection zone experience a turbulent motion with velocity \mathbf{v}_{conv} . When they reach the convective boundary layer, their inertia will prevent them from stopping abruptly; i.e., they will “overshoot” from the convection zone into the radiative layer over an unknown distance, which we denote as α_{ov} (in analogy to α_{mlt} , it is expressed in the unit H_p). The way in which the fluid elements overshoot the convective boundary depends on the location of the convection zone inside the star and the physical circumstances at that position. For extensive discussions, see Zahn (1991), Viallet et al. (2015), Cristini et al. (2016), Constantino et al. (2017), and Arnett et al. (2019). Three-dimensional simulation studies have indicated at least three physical processes that may come into play: penetration by plumes leading to superadiabatic mixing over a distance d_{pen} (Zahn, 1991), subadiabatic thermal diffusion over a distance described by means of an exponentially decaying mixing profile with parameter f_{ov} (Freytag et al., 1996; Herwig, 2000), or turbulent entrainment that occurs over a dissipation length scale expressed as a distance l_d (Meakin & Arnett, 2007; Viallet et al., 2013). These imply a different and uncalibrated level and functional form of convective boundary mixing (CBM) and have a different temperature gradient in the transition layer. We use the notation of the free parameter α_{ov} to express the unknown length scale over which the fluid elements move from inside a convective region into the radiative adjacent zone, representing any of d_{pen} , f_{ov} , l_d , or other formulations (see Augustson & Mathis, 2019).

The rate of change of species of type i with relative mass fraction X_i is caused by various processes, some of which are diffusive but others that are not. When the rate of change happens much faster than the nuclear timescale, it is customary to approach $\partial X_i / \partial t$ by a diffusion equation for computational convenience. In the simplest case of changes due to convective motions, along with nuclear fusion in a spherically symmetric star, we can write

$$\frac{\partial X_i}{\partial t} = \mathcal{R}_i + \frac{1}{\rho r^2} \frac{\partial}{\partial r} \left[(D_{\text{conv}} + D_{\text{ov}}) \rho r^2 \frac{\partial X_i}{\partial r} \right], \quad (27)$$

where the rate of change of X_i due to nuclear reactions is denoted symbolically as \mathcal{R}_i . The diffusion coefficient associated with the convective mixing described by mlt is given by

$$D_{\text{conv}} = \frac{1}{3} \alpha_{\text{mlt}} H_p v_{\text{conv}}. \quad (28)$$

The unknown profile of CBM due to the overshooting of the fluid elements beyond the convective boundary is denoted here as D_{ov} . Each of the profiles $D_{\text{conv}}(r)$ and $D_{\text{ov}}(r)$ (expressed in the physical units $\text{cm}^2 \text{s}^{-1}$) is in general an unknown function of r and involves at least one free parameter (α_{mlt} and α_{ov}).

For stars with a convective core, the lack of calibration of the physics in the convective boundary layers implies a serious limitation. Indeed, the CBM influences the amount of matter that can be brought into the central regions where nuclear fusion takes place. The higher the CBM, the more fresh fuel reaches the nuclear reactor and hence the longer the nuclear fusion can go on. This has a major impact on the star’s core mass and its age. For this reason, calibration of the amount of matter in the convective core of a star M_{cc} , via an observational estimation of the profile $D_{\text{ov}}(r, t)$ and its feedback throughout the evolution of the star, is a crucial piece of information to predict a star’s life and age. It was shown that space asteroseismology has the capacity to deliver such an estimation across a large mass range by Deheuvels et al. (2016) and Pedersen et al. (2018), including assessment of the temperature gradient in the near-core boundary layer (Michielsen et al., 2019). This potential had already been pointed out by Dziembowski & Pamyatnykh (1991) but remained without practical application until recently. Concrete applications to derive $D_{\text{ov}}(r)$ based on space asteroseismology are discussed in Sec. IV.

2. Simplification to 1D stellar models

Because of the immense range in timescales and spatial scales occurring in the interiors of stars, stellar models must necessarily remain a simplified version of reality. Indeed, the computation of 3D models across stellar evolution is not yet feasible. One thus needs to adopt simplifications in the computation of stellar structure models. With asteroseismic applications in mind, we make two important approximations: we assume that any equilibrium model, which will be perturbed to compute a star’s oscillations, is spherically symmetric and does not have a dynamical atmosphere. The first simplification implies that we can rely on 1D models in hydrostatic equilibrium computed for stars that do not rotate close to their so-called critical rotation rate. The second simplification allows us to use a static atmosphere model to connect to the stellar interior as outer boundary, at each time step in a star’s evolution.

In practice, stellar evolution codes rely on mass-loss or accretion rates described by parametrized laws, such that an amount $\dot{M} \cdot \Delta t$ is peeled off or added to the stellar model after a duration Δt of stellar life has passed. For each particular instance in time, the stellar model is considered to have a static atmosphere on top of its interior structure. In this way, the models are built while taking

mass loss or accreted mass into account and ignoring the dynamical properties due to a stellar wind or an accretion disk. This simplifies the boundary conditions adopted to close the set of equations to be solved. This basic assumption is justified for the majority of applications in asteroseismology, because nonradial oscillations are usually undetectable for stars that have a strong dynamical wind or high levels of accretion.

Ignoring fast rotation needs more justification than neglecting the dynamics of the wind, because rotation is common in stars throughout their lives. Rotation acts upon stellar structure in at least three ways: it deforms the star from spherical symmetry, it leads to higher polar than equatorial flux due to gravity darkening, and it induces various instabilities and mixing in the stellar interior. The level of confidence in how to treat these effects is different for the three aspects. Gravity darkening was first discussed by von Zeipel (1924). It stands for a reduction in the flux and hence in the effective temperature of the star resulting from the reduced gravity in the equatorial regions relative to the polar ones. The von Zeipel effect is expressed as

$$T_{\text{eff}} = T_{\text{eff,p}} \left(\frac{g_{\text{eff}}}{g_{\text{eff,p}}} \right)^{\beta}, \quad (29)$$

where $T_{\text{eff,p}}$ and $g_{\text{eff,p}}$ are the effective temperature and effective gravity at the pole of the star. For a radiative envelope as considered by von Zeipel, $\beta \simeq 0.25$. In the presence of a convective envelope, β is usually assumed to be $\beta < 0.1$. This limited knowledge of the exponent β , and along with it a nonsymmetrical stellar wind, implies a nontrivial treatment in stellar evolution computations in the presence of rotation.

By definition, the critical (or breakup) velocity is reached when the outwardly directed centrifugal acceleration is equal to the inward effective gravitational acceleration at any one point of the stellar surface. Here we work with the critical rotation frequency since we are making a comparison to the frequencies of oscillations. Usually the Roche approximation is adopted, which assumes that the mass concentration inside the star is not distorted by the rotation. In this case, the polar (R_p) and equatorial (R_e) radii of the star differ by less than a factor of 3/2, where $R_{e,\text{crit}}/R_{p,\text{crit}} = 3/2$. This leads to the critical rotation frequency given by $\Omega_{\text{crit}} = \sqrt{GM_{\star}/R_{e,\text{crit}}^3} = \sqrt{8GM_{\star}/27R_{p,\text{crit}}^3}$, with M_{\star} the mass of the star and $R_{e,\text{crit}}, R_{p,\text{crit}}$ its critical equatorial and polar radii. This is the solution for the critical rotation frequency when the Eddington parameter $\Gamma = \kappa L/4\pi cGM_{\star} < 0.639$ (Maeder, 1999). The other solution is not considered here, as almost all applications in asteroseismology thus far occur for stars without a strong radiation-driven wind.

The prediction $R_{e,\text{crit}}/R_{p,\text{crit}} < 3/2$, along with von Zeipel's formula (29), can be evaluated directly from in-

terferometric measurements of stellar surfaces. Such observations indeed show that fast rotators are oblate (e.g. Domiciano de Souza et al., 2018) and that their surface properties and winds are not spherically symmetric, as revealed by, e.g., Kervella & Domiciano de Souza (2006) and Domiciano de Souza et al. (2014). However, fast rotating stars do not necessarily comply with the Roche approximation. Interferometry of the Be star *Archernar* (Domiciano de Souza et al., 2003) led to $R_e/R_p \simeq 1.56$. Moreover, von Zeipel's law is not adhered to by the stars having gravity darkening measurements from interferometry (Domiciano de Souza et al., 2018). This led Gagnier et al. (2019) to perform a new evaluation of the critical rotation of a star from 2D static models, with the conclusion that β decreases from 0.25 to 0.13 for rotation rates evolving from slow to critical.

In conclusion, the computation of 2D equilibrium models in the presence of rotation comes with major uncertainty, even in its simplest aspects of the local surface and its flux. For this reason, computations of stellar oscillations from 2D equilibrium models are often restricted to static polytropic models (Lignières et al., 2006; Reese et al., 2006). Although progress is steadily achieved (Ouazzani et al., 2012; Reese et al., 2013), fitting of measured frequencies to perform 2D asteroseismic modeling is not within reach yet. We thus do not treat 2D equilibrium models as input for oscillation-mode computations. Rather, we focus in this review on tuning the stellar interior quantitatively by taking into account the Coriolis acceleration at the level of the mode computations while relying on 1D equilibrium models. Lignières et al. (2006), Ballot et al. (2010) and Ouazzani et al. (2017) provided comparisons between oscillation frequency predictions of rapid rotators from 1D versus 2D equilibrium models using higher-order perturbative expressions for the effect of rotation. These studies revealed that a 1D treatment for p modes leads to appropriate oscillation predictions for stars rotating up to $\sim 15\%$ of the critical rotation frequency. For high-order g modes, the 1D treatment is justified up to $\sim 70\%$ of the critical rotation frequency (Henneco et al., 2021). Within these regimes, it is justified to work with 1D equilibrium models as input for the computation of oscillation modes, where no rotation or only the spherically symmetric component of the centrifugal force is included in Eq. (19). In the latter case, the simplified equation of hydrostatic equilibrium reads

$$\frac{\partial p}{\partial r} = -\frac{Gm\rho}{r^2} + \frac{2}{3}\rho r \Omega^2. \quad (30)$$

3. Standard 1D stellar models in hydrostatic equilibrium

Thus far we have focused on the internal structure of the star, but we have hardly considered its chemical evolution. The chemical composition inside the star at time t is described by relative mass fractions of species i ,

$X_i = X_i(r, t)$, where $r \in [0, R_*(t)]$ with $R_*(t)$ the radius of the spherically symmetric star at time t in its evolution. These profiles are an important aspect of stellar models, because they determine the opacity, thermodynamical characteristics, and energy production ε due to nuclear reactions as in Eq. (21). These reactions, in turn, change the chemical composition and rule the life of the star.

To solve the stellar structure equations (18) – (21) along with the energy transport equation(s) and the changes in the chemical profiles $X_i = X_i(r, t)$, the microscopic properties of the stellar matter need to be known as a function of $p(r, t)$, $T(r, t)$, etc. This requires adopting an equation of state, various thermodynamical properties, opacity tables to compute the Rosseland mean opacity, a network of nuclear reaction rates, etc. This is jointly referred to as “input physics” when one computes stellar models. Further, proper boundary conditions at the center and surface of the star and initial conditions characterizing the star’s properties at birth ($\tau \equiv 0$) when it has arrived at the so-called Zero-Age-Main-Sequence (ZAMS) have to be chosen (this is not discussed here, see, e.g., Kippenhahn et al., 2012). The solution of the equations for chosen boundary conditions delivers what is called a stellar equilibrium model at age τ described by $m(r, \tau)$, $p(r, \tau)$, $L(r, \tau)$, $T(r, \tau)$, $X_i(r, \tau)$, and by all other relevant functions that can be derived from these solutions, with $m(r, \tau)$ the mass enclosed by the shell positioned at $r \in [0, R_*(\tau)]$ inside the star.

The ZAMS $\tau \equiv 0$ is defined as the point in time when hydrogen fusion occurs in full equilibrium in the center of the star. At the ZAMS, the star has a specific yet unknown chemical mixture of species X_i in its interior. This mixture is the result from the initial chemistry it received from its birth cloud when it started as a fully convective protostar on the so-called Hayashi track (see, e.g., Kippenhahn et al., 2012, for a definition) and from changes in this mixture due to nuclear reactions and due to mixing taking place during the contraction phase from the Hayashi track towards the ZAMS. Often, the computation of stellar models for low-mass stars adopts the solar mixture using the Sun’s current or initial surface abundances (Asplund et al., 2009). On the other hand, the surface abundances of B-type stars in the solar neighborhood (Przybilla et al., 2013) constitute a logical choice for the initial chemical mixture when computing high-mass stellar models. With a specified chemical mixture, the initial composition is an input for the 1D evolutionary computations. We denote this initial composition as X_{ini} , Y_{ini} , Z_{ini} , which stand for the initial hydrogen, helium and metal mass fractions, complying with $X_{\text{ini}} + Y_{\text{ini}} + Z_{\text{ini}} = 1$. For most of the phases of stellar evolution, the stars do not change on a dynamical timescale, as it is much shorter than the contraction timescale and the nuclear timescale. Whenever this is the case, the left hand side of Eq. (19) is zero and the

resulting stellar model is in hydrostatic equilibrium.

In the simplest case of a nonrotating nonmagnetic single star without a stellar wind, there is no additional body force \mathbf{f} in Eq. (19) such that the pressure and gravity forces are the actors that compensate for each other. Such simplifications lead to equilibrium models that resemble reality well for many of the stars and during large fractions of their life. Stellar models computed with those simplifications for the interior and with a static atmosphere as outer boundary are called standard stellar models. Evolutionary tracks representing such standard models are included as full lines in Fig. 1. Extensive comparisons of stellar evolution models computed with independently developed codes have been done for low-mass stars in the context of CoRoT (Monteiro, 2009) and show impressive agreement when the same input physics is considered. This is in sharp contrast to the major differences occurring for stellar evolution computations based on similar input physics for high-mass stars, even for nonrotating models (Martins & Palacios, 2013).

4. Nonstandard 1D models with microscopic atomic diffusion

Composition changes do not occur only in regions where nuclear reactions take place. In addition to full and instantaneous mixing in convective regions and full or partial mixing in convective boundary layers, the chemical profiles in radiative regions may also change due to microscopic and macroscopic transport processes (e.g. Pinsonneault, 1997; Salaris & Cassisi, 2017, for reviews). Which of those is dominant depends on the timescales upon which they act. Macroscopic mixing may be induced by turbulence, magnetic fields, waves, rotation, etc. In this section, we focus on the microscopic scale and consider element transport caused by microscopic atomic diffusion. The accompanying local chemical composition changes induced by it are caused by gradients operating in the radiative layers of the star. These gradients may introduce lower or higher concentrations of particular chemical species in particular layers of the radiative envelope. Section II.A.5 treats macroscopic element transport.

A key aspect of assessing the importance of microscopic diffusion is that the timescales upon which it acts are significantly different for the atmosphere than for the interior of the star (Michaud et al., 2015). Diffusion timescales are typically less than a century for the stellar atmosphere, while millions to billions of years for the interior regions. Given that we focus on asteroseismic applications and on the tuning of stellar interiors, we do not consider modeling surface abundances affected by atomic diffusion as observed in some intermediate-mass stars (so-called Ap and Bp stars). Rather, we limit ourselves to those aspects of atomic diffusion that act on long timescales in radiative parts of the stellar interior,

keeping in mind the importance of atomic diffusion for the solar case, as demonstrated from helioseismology by Christensen-Dalsgaard et al. (1993).

Following Thoul et al. (1994), Chayer et al. (1995), Richer et al. (2000), VandenBerg et al. (2002), Richard et al. (2002a,b), Michaud et al. (2004), Hu et al. (2011), Théado et al. (2012), and Deal et al. (2016), four different aspects of microscopic atomic diffusion are considered in stellar models. These occur due to pressure, temperature, and concentration gradients on the one hand, and radiative forces on the other hand. While pressure and temperature gradients augment the concentration of more massive species toward the center of the star, concentration gradients have the opposite effect. On the other hand, radiative forces levitate species with an efficiency that depends on the details of the atomic structure of the involved isotopes. The calculation of the appropriate radiative accelerations is therefore challenging in terms of computation times. The accelerations can be computed from atomic data by treating the appropriate multicomponent gas (Burgers, 1969). This requires evaluations of the frequency-dependent absorption coefficients derived from a screened Coulomb potential (Paquette et al., 1986), taking into account partial ionization, and this for all the layers inside the star (see Thoul et al., 1994). Once the overall local velocities w_i for each of the species i involved in the atomic diffusion are computed, they can be inserted in the equation governing the time evolution of the mass fraction X_i :

$$\begin{aligned} \frac{\partial X_i}{\partial t} = & \mathcal{R}_i - \frac{1}{\rho r^2} \frac{\partial}{\partial r} (\rho r^2 X_i w_i) \\ & + \frac{1}{\rho r^2} \frac{\partial}{\partial r} \left[(D_{\text{conv}} + D_{\text{ov}}) \rho r^2 \frac{\partial X_i}{\partial r} \right], \end{aligned} \quad (31)$$

where the second term on the right-hand side is the result of the microscopic atomic diffusion acting upon species X_i and the third term is the result of macroscopic transport of the chemical species due to convection and overshooting.

If atomic diffusion can be treated without the radiative effects, which is a good approximation for cool stars with extended convective envelopes such as the Sun, its impact on the computation time required for evolutionary model calculations is modest. As a consequence, the use of such simplified microscopic diffusion computations without levitation in evolutionary models is widespread (e.g., Chaboyer et al., 1995; Pinsonneault, 1997). With levitation included, the computation of w_i and the solution of the set of equations (31) at each step of the evolution is a major challenge. Nevertheless, such computations have been done with the specific aim of asteroseismic applications, adopting various levels of complexity. Studies of stellar interiors of A- and F-type stars were given by Turcotte et al. (1998), Deal et al. (2018), and Verma & Silva Aguirre (2019), subdwarf B stars were studied by Hu et al. (2011) and Bloemen et al. (2014),

and white dwarfs were studied by Romero et al. (2017) and De Gerónimo et al. (2019), where the last two papers did not include radiative levitation. Figure 5 shows the influence of atomic diffusion on g-mode frequencies of intermediate-mass stars whose rotation period is about 10 times longer than its dipole-mode periods. The frequency shifts induced by atomic diffusion are much larger than the measurement uncertainties, highlighting the fact that asteroseismology has the capacity to evaluate the need (or not) of radiative levitation in models of such stars, as illustrated by Mombarg et al. (2020).

It is instructive, particularly for the later nuclear burning stages, to compare the asteroseismic results based on evolutionary models with those obtained from static structure models that are more sophisticated in some aspects of the structure yet less prone to unknown aspects of the physics in the models that accumulate throughout the evolution. This approach was followed by Charpinet et al. (2011) and Van Grootel et al. (2013), as well as by Giammichele et al. (2018) and Charpinet et al. (2019) for subdwarfs and white dwarfs, respectively. Differences in the stellar structure profiles from such static models [$m(r)$, $p(r)$, $T(r)$, $L(r)$, and $X_i(r)$] compared to those obtained from evolutionary models can then be used to improve the input physics adopted for full evolutionary computations via an iterative loop between asteroseismology and the equilibrium models as given by Timmes et al. (2018) and De Gerónimo et al. (2019).

Atomic diffusion impacts the concentration of the species in the stellar interior on timescales that are relevant for stellar evolution. Its effect is hard to unravel from a star's luminosity and effective temperature, which are the two quantities that define the evolutionary tracks in an HRD. Models with and without atomic diffusion (either with or without levitation) usually differ far less than typical observational errors of L or $\log g$ plotted versus T_{eff} as shown by Dotter et al. (2017) and by Deal et al. (2018). As a confrontation between data and theory in the HRD is commonly the only assessment to evaluate stellar evolutionary theory, and given the computational requirements, microscopic atomic diffusion is often ignored in stellar and galactic astrophysics. Its inclusion is, however, critical when evaluating surface abundances for archaeological chemical tagging (Dotter et al., 2017) and to interpret asteroseismic data as done by Verma et al. (2017), Deal et al. (2018, 2020), and Mombarg et al. (2020).

5. Nonstandard 1D models with rotation and waves

Rotation has a major effect on stellar evolution (Maeder, 2009). Yet in this era of space asteroseismology, it has become clear that its treatment in stellar interiors is up for improvement. Predictions based on local conservation of angular momentum and rotational mixing, both

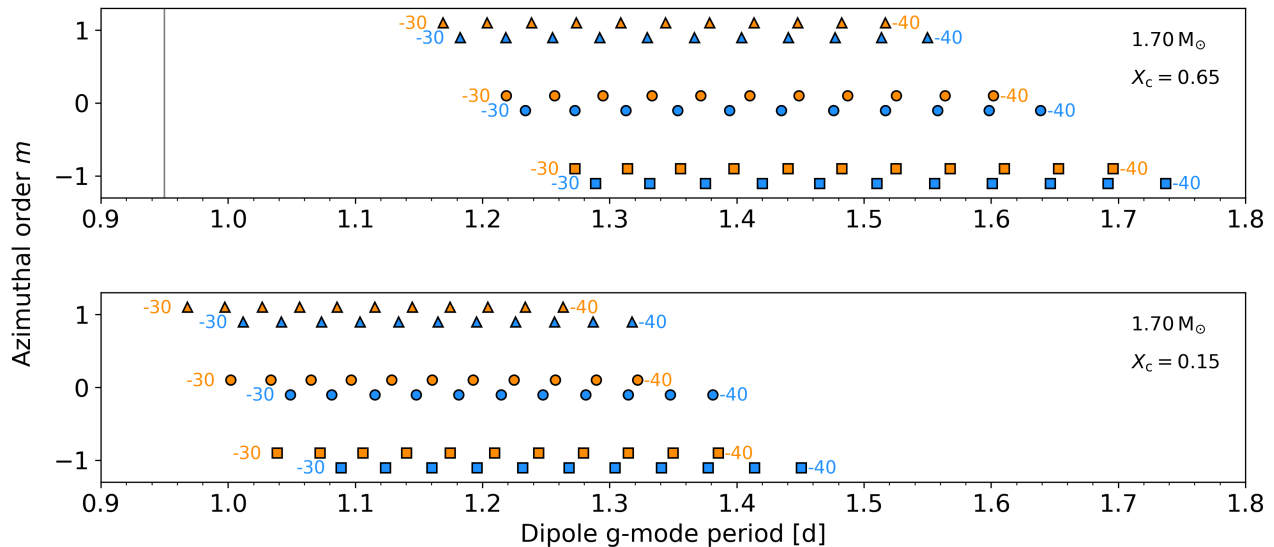


FIG. 5 Shifts in the periods of dipole ($l = 1$) triplet g modes of two equilibrium models [blue (orange), without (with) atomic diffusion, including radiative levitation] with the same input physics, for parameters $M = 1.7 M_{\odot}$, $X_{\text{ini}} = 0.7154$, $Z_{\text{ini}} = 0.022$, and at two different evolutionary stages expressed in terms of the central hydrogen fraction X_c . The g modes were computed assuming rigid rotation with a period of 14.4 d. The radial orders n are labeled. The vertical line indicated on the left side in the upper panel denotes the measurement uncertainty for such mode periods from a 4-yr nominal *Kepler* light curve. Figure based on stellar models in Mombarg et al. (2020) by courtesy of Joey Mombarg, KU Leuven.

of which have been used extensively in stellar evolution models the past few decades, lead to predictions that are incompatible with asteroseismology, as discussed later. Even 1D models of slowly rotating stars face challenges. Improving them is a major aim of asteroseismology and of stellar astrophysics in general. We have now reached the stage where asteroseismic inferences based on high-quality space photometry can be used to derive $\Omega(r)$ for stars and to provide a calibration of the poorly known physical ingredients of rotating stellar models, which is in line with Gough’s quote in the Introduction: asteroseismology in action.

To compute equilibrium models including rotation, we need to know $\Omega(r)$ and how it changes throughout stellar evolution. Asteroseismology is a major and thus far unique game changer on this front. While we discuss methods to deduce $\Omega(r)$ in Sec. IV.D., we provide the current status of the rotation frequencies in the region just outside the convective core (denoted as Ω_{core} throughout the review) in Fig. 6. We also highlight the envelope (Ω_{env}) or surface (Ω_{surf}) rotation frequency for the stars with this information. Figure 6 updates the work of Aerts et al. (2019), who presented these asteroseismic measurements for low- and intermediate-mass stars distributed across all evolutionary stages from *Kepler* photometry. We discuss these results extensively in Sec. IV, but we point out here that almost all single stars in the covered mass range of $[0.8, 3.3] M_{\odot}$ were found to rotate nearly uniformly during the core-hydrogen-burning and core-

helium-burning phases and that the angular momentum of the helium-burning core of these stars is in agreement with the angular momentum of white dwarfs. Figure 6 implies a strong decrease of core angular momentum in the phase when stars have a convective core. Current stellar evolution theory of rotating stars cannot explain these asteroseismic results. This calls for a reevaluation of 1D models with rotation.

Stellar models with rotation often adopt the approximation of shellular rotation, following Zahn (1992). In this approximation, one assumes that the chemical composition and the angular velocity remain constant on isobars. As such, the ratio of the rotation frequency of the star $\Omega(r)$ with respect to Ω_{crit} [or the accompanying $v(r)/v_{\text{crit}}$] is used as input for the numerical computations of the stellar models. Given the limited knowledge on angular momentum evolution during the contraction phase, the input ratio $\Omega(R_{\star})/\Omega_{\text{crit}}$ is usually taken at the ZAMS, assuming a rigid rotation profile to start the evolutionary computations.

From a theoretical perspective, rotation is expected to induce a myriad of processes and instabilities in the stellar interior, leading to transport of angular momentum and of chemical species. This was extensively discussed by Maeder (2009). As recently reviewed in the modern context of asteroseismology, these macroscopic processes can be classified into four main categories (Aerts et al., 2019, Sec. 3): meridional circulation, hydrodynamical instabilities, magnetorotational instabilities, and IGWs.

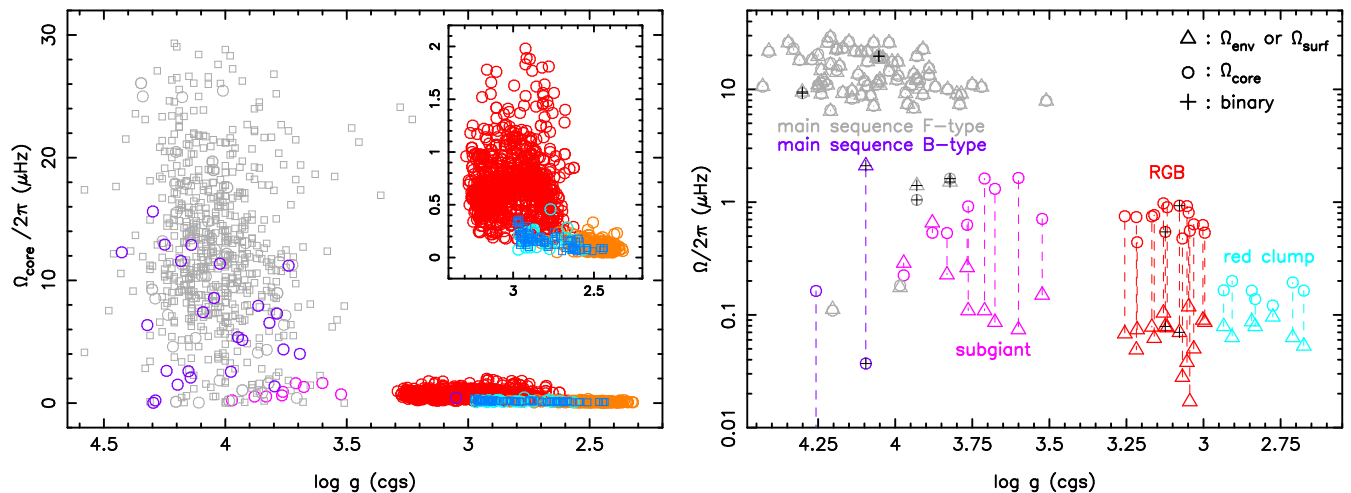


FIG. 6 Left panel: core (near-core) rotation rates derived from mixed (gravity) modes for stars in core-hydrogen burning (purple and gray), hydrogen-shell burning (pink and red), and core-helium burning (after the helium flash in orange and avoiding the helium flash in cyan). The circles indicate stars with asteroseismic estimates of Ω_{core} and $\log g$ taken from Aerts et al. (2019); their errors are smaller than the symbol size. The squares are additional stars with asteroseismic determinations for Ω_{core} but with less reliable values for $\log g$ from spectroscopy and/or stellar models from Li et al. (2020, 622 γ Dor stars, indicated in gray) and from Tayar et al. (2019, 72 core-helium-burning red giants in blue). Their uncertainties for $\log g$ range from 0.2 (blue squares) to 0.5 dex (gray squares) and are omitted for clarity. Right panel: all stars with an additional measurement of the envelope (from p modes) or surface (from rotational modulation) rotation frequency. This figure is an update of Fig. 4 in Aerts et al. (2019) and is based on data kindly provided by Gang Li, Sydney University and Jamie Tayar, University of Hawaii.

However, the concept of “rotational mixing” in stellar evolution computations and in the literature often stands for the macroscopic element transport due to the action of circulation and all instabilities together. Further, in analogy to rotational mixing, we will use the term “pulsational mixing” for element transport caused by waves. Because rotational or pulsational mixing is expected to homogenize the chemical mixture in the layers where they are active on short timescales, models including these ingredients often ignore the microscopic atomic diffusion effects leading to concentrations of species. However, there is no justified physical reason for this “computationally convenient” simplification when the timescales of these processes are similar (see Deal et al., 2020).

The transport equation controlling the evolution of the angular momentum $r^2\Omega(r)$ reads

$$\begin{aligned} \frac{\partial}{\partial t} (r^2\Omega) &= \frac{1}{5\rho r^2} \frac{\partial}{\partial r} [\rho r^4 \Omega U(r)] \\ &+ \frac{1}{\rho r^2} \frac{\partial}{\partial r} \left(\rho r^4 D_{\text{shear}} \frac{\partial \Omega}{\partial r} \right). \end{aligned} \quad (32)$$

Here $U(r)$ is the radial component of the velocity due to meridional circulation and the diffusion coefficient D_{shear} represents a variety of vertical shear instabilities occurring between layers subject to different velocities (Maeder, 2009). In addition to these instabilities, IGWs also occur in the radiative zones of stellar interiors. Given that the dominant restoring force for an IGW is the buoyancy force of Archimedes, the frequencies of IGWs are below

$N(r)$. These IGWs propagate in the radiative zones of the star, where they dissipate, depositing angular momentum efficiently in the layers where they break. A pioneering study of the excitation and propagation of IGWs in Sun-like stars was presented by Charbonnel & Talon (2005). It demonstrated convincingly the capacity of IGWs to transport angular momentum in an efficient way, explaining the flat rotation profile of the Sun derived from helioseismology.

As for the transport of the chemical species due to rotation, Chaboyer & Zahn (1992) showed that it can be approximated as a diffusive process in the presence of strong horizontal turbulence due to shear instabilities. For this reason, the diffusive part in the chemical composition equations in Eq. (27) gets extra terms due to various effects of rotation, each with its own diffusion coefficient (Maeder, 2009). Aside from rotation, additional causes of element mixing are also considered, particularly in transition layers that are stable against the Schwarzschild criterion, but unstable against the Ledoux criterion, for the cases of both $\nabla_{\mu} > 0$ (called semiconvective mixing) and $\nabla_{\mu} < 0$ (called thermohaline mixing). Magnetism and IGWs may also affect the mixing. Overall, this brings a multitude of extra diffusion coefficients that affect the chemical composition profiles of the star, aside from $D_{\text{conv}}(r)$ and $D_{\text{ov}}(r)$ included in Eq. (27). For rotation, these have been grouped as $D_{\text{shear}}(r)$ and $D_{\text{eff}}(r)$ adopting the notation by Maeder (2009), where the latter is due to meridional circulation in the approx-

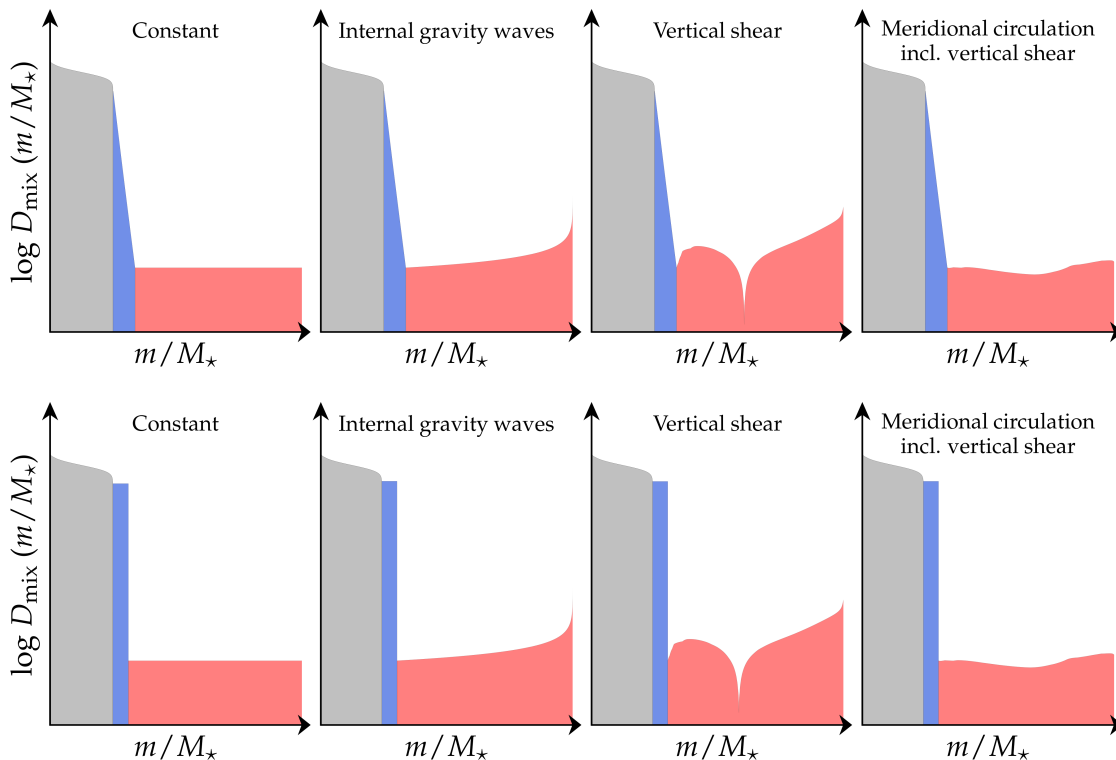


FIG. 7 Schematic representation of mixing profiles due to various transport processes in stars with a convective core (indicated in gray) and a radiative envelope for exponentially decaying diffusive core overshooting (upper panels) and convective penetration (lower panels) as CBM (purple). Four types of envelope mixing based on different theoretical frameworks are considered (pink), as labeled. Figure courtesy of May Gade Pedersen, KU Leuven, based upon data for $5 M_{\odot}$ and $3 M_{\odot}$ ZAMS models kindly made available by Sylvia Ekström and Tami Rogers, from Georgy et al. (2013) and Rogers & McElwaine (2017), respectively.

imation of strong horizontal turbulence and the former stands for the joint effect of vertical shear due to all sorts of rotational (and possibly magnetic) instabilities. Pulsational mixing profiles due to IGWs, adopting a diffusion approximation, were derived from hydrodynamical simulations for a $3 M_{\odot}$ ZAMS star by Rogers & McElwaine (2017), resulting in a diffusion coefficient depending on the density as $D_{\text{IGW}}(r) \sim D_{\text{IGW}} \cdot \rho^{-\gamma}(r)$ with $\gamma \in [0.5; 1]$.

Figure 7 offers a schematic representation of mixing profiles adopted in stellar evolution computations, where the envelope mixing profiles were stitched to the CBM at an arbitrary level. The two rightmost panels show profiles for a $5 M_{\odot}$ ZAMS model rotating at 50% of the critical rate taken from Georgy et al. (2013); the particular shape of the third panel from the left in Fig. 7 is due to the drop in $U(r) \simeq 0$ in the envelope layers near $m/M_{\star} \simeq 0.5$ (cf., Maeder, 2003). Similar sharp-peaked mixing profiles based on independently developed stellar evolution codes were found by Heger et al. (2000), Chieffi & Limongi (2013), and Paxton et al. (2013), among others. The profile labeled as Internal gravity waves is from a $3 M_{\odot}$ nonrotating model computed by Rogers & McEL-

waine (2017). In general, the mixing profiles indicated in Fig. 7 vary strongly during the evolution of the star, but it is poorly understood how. In this sense, none of these profiles are calibrated. Asteroseismology offers a major tool to infer the overall mixing profiles throughout stars, denoted as of now as $D_{\text{mix}}(r, t)$.

Inferences of the internal mixing in stars received less attention than the probing of $\Omega(r, t)$ thus far. The reason is simple: estimation of $D_{\text{mix}}(r, t)$ is much harder than of $\Omega(r, t)$. The latter can be achieved in a quasi-model-independent way and (almost) directly from the Fourier transform of the data, as explained in Sec. II.B. Given that the levels of $D_{\text{mix}}(r, t)$ as displayed in Fig. 7 differ by orders of magnitude in the literature, it is highly beneficial to infer asteroseismic levels of mixing (and the accompanying convective core mass) to bring the models into agreement with measurements of nonradial oscillations of intermediate- and high-mass stars. Asteroseismology of γ Dor, SPB, and β Cep stars has the potential to provide the answer if proper ensembles of such pulsators are subjected to asteroseismic inference. We return to this potential and its first applications in Sec. IV.

6. One-dimensional equilibrium models as input for asteroseismology

For stars with detected nonradial oscillations, space asteroseismology brings an entirely new way to assess the rotation frequency $\Omega(r, t)$ and the overall chemical mixing $D_{\text{mix}}(r, t)$ in the radiative zones of stars. Indeed, mode frequencies provide high-precision observational constraints coming directly from the deep stellar interior. Assembling asteroseismic data for stars in various evolutionary stages allows one, in principle, to assess the change of $\Omega(r)$ and $D_{\text{mix}}(r)$ as a function of stellar age. Yet asteroseismic probing capacities for $\Omega(r, t)$ and $D_{\text{mix}}(r, t)$ are different for low-mass stars with a radiative core and a convective envelope than for high-mass stars with a convective core and a radiative envelope. They also differ for young stars burning hydrogen in their core and for old stars close to their final fate as stellar remnant. To understand why, it is necessary to dive into the nature of nonradial oscillations based on 1D equilibrium models.

As discussed earlier, the simplest versions of 1D stellar equilibrium models are nonrotating nonmagnetic models having only 6 free parameters for fixed choices of the input physics: the stellar birth mass M_* , the initial chemical composition guided by a galactic enrichment law (e.g., as in Verma et al., 2019) and expressed as relative mass fractions ($X_{\text{ini}}, Y_{\text{ini}}$) (or equivalently $X_{\text{ini}}, Z_{\text{ini}}$), the mixing-length value α_{mlt} that gives rise to the mixing profile $D_{\text{conv}}(r)$, the convective overshoot length scale α_{ov} that leads to the CBM profile $D_{\text{ov}}(r)$, and the age τ . Asteroseismic modeling will then consist of determining the maximum likelihood estimators (MLEs) of these six free parameters from measured oscillation mode frequencies (often accompanied by other observables). For a rotating star, at least one additional parameter has to be added (Ω for the simplest case of rigid rotation). Once the most likely 6D or 7D parameter vector $\theta \equiv (M_*, X_{\text{ini}}, Y_{\text{ini}}, \alpha_{\text{mlt}}, \alpha_{\text{ov}}, \tau)$ has been found, the exercise can be repeated for other choices of the input physics to come to an overall selection of the best stellar models for an ensemble of stars. Any residual values between the measured and theoretically predicted oscillation frequencies of unambiguously identified modes can then be exploited to assess shortcomings in $\Omega(r, \tau)$ and $D_{\text{mix}}(r, \tau)$ for the fixed chosen input physics. Once a sufficiently large and unbiased (in terms of rotation, initial chemical composition, etc.) sample of nonradial pulsators with suitable modes is available from observations, we can investigate whether they adhere to the same theory of stellar structure and evolution or instead need different internal mixing profiles as in Fig. 7. We return to this procedure of “ensemble asteroseismology” and will discuss simplifications and applications of it for various types of stars in Sec. IV. An overall scheme representing this approach is graphically visualized in Fig. 16 and is

discussed in Sec. III.

B. Linear nonradial oscillation modes

We now consider small perturbations to 1D spherically symmetric stellar models in hydrostatic equilibrium, whose quantities we assume to have been derived from solving the stellar structure equations. We denote the equilibrium solutions at age τ as $m_0(r), p_0(r), L_0(r), T_0(r), X_{i,0}(r)$. We assume that the oscillations cause 3D periodic deviations from equilibrium with amplitudes that justify a linear approach in the derivation of the pulsation equations. In practice this implies that we perturb Eqs. (18), (19), and (21) while retaining only the linear terms in the perturbations. For example, a fluid element at position vector \mathbf{r}_0 in the equilibrium model of the star is displaced due to the 3D stellar oscillations to the vector $\mathbf{r}_0 + \delta\mathbf{r}$, where $\delta\mathbf{r}$ is the Lagrangian perturbation of the position vector. The Lagrangian perturbation to the pressure then becomes

$$\delta p(\mathbf{r}) = p(\mathbf{r}_0 + \delta\mathbf{r}) - p_0(\mathbf{r}_0) = p(\mathbf{r}_0) + \delta\mathbf{r} \cdot \nabla p_0 - p_0(\mathbf{r}_0). \quad (33)$$

All perturbed quantities that occur in Eqs. (18), (19), and (21) can be deduced in a similar way. The linearized versions of the perturbed equations are obtained by inserting expressions like Eq. (33) into the full equations, subtracting the version of those equations for the static equilibrium solutions, and neglecting all terms of order higher than 1 in the perturbed quantities. Aerts et al. (2010, Chap. 3) gave full derivations; we adopt the notations from that book. Additional extensive discussions on the theory of nonradial oscillations were given by Cox (1980); Unno et al. (1989) and Smeyers & Van Hoolst (2010), where the last work includes a particularly extensive historical perspective of the topic.

We argued in Sec. II.A that it is meaningful to ignore the nonradial components of the centrifugal force for stars that rotate up to $\sim 70\%$ of their critical rotation frequency and to treat the Coriolis and Lorentz forces only at the level of the 3D perturbations to computed nonradial g modes, but not for the equilibrium models. For p modes, this validity already breaks down above $\sim 15\%$. In the following sections, we gradually build up the complexity of the treatment of the oscillations. An obvious simplification occurs when we consider the adiabatic approximation for the computation of the modes. This means that we can ignore the perturbations of the entropy S in Eq. (21). We do so in the rest of this section. Working in the adiabatic approximation is good and fully justified as long as we consider modes that are mostly sensitive to the physics in the deep stellar interior where adiabaticity is well met. This restriction is a point of attention when dealing with modes that have their dominant energy in the envelope of the star, close

to the stellar surface; cf. p modes in low-mass stars as in Fig. 9, which is discussed later.

1. Pressure and gravity modes

We simplify the perturbed stellar structure equations maximally by ignoring the Lorentz and Coriolis forces. In that case, the only forces at play are the pressure force and gravity. These simplifications offer maximal separability in terms of spherical polar coordinates (r, θ, ϕ) and time t , where r is the distance to the center of the star, θ is the angle from the polar axis, which is taken to coincide with the rotation axis of the star, and ϕ is the longitude. The displacement $\delta\mathbf{r}$ can then be separated into radial and horizontal components as

$$\delta\mathbf{r} = \xi_r \mathbf{a}_r + \boldsymbol{\xi}_h, \quad (34)$$

where \mathbf{a}_r is a unit vector directed radially outward. The solutions to the resulting perturbed versions of the equations, along with proper boundary conditions for the center and for the surface of the star (not discussed here, see, e.g., Unno et al., 1989) lead to nontrivial solutions only for the nonzero eigenfrequencies ω of the stellar equilibrium model. Each of these eigenfrequencies corresponds to a so-called time-dependent spheroidal mode of oscillation. Because the equations are homogeneous, the eigen-solutions are determined only up to a constant factor.

Each of the nonradial eigenmodes of the equilibrium model corresponds to a displacement vector $\boldsymbol{\xi}$ whose components are written in terms of a mode degree l , azimuthal order m , and radial order n as $\boldsymbol{\xi}(r, \theta, \phi, t) = [(\xi_{r,nl} \mathbf{a}_r + \xi_{h,nl} \nabla_h) Y_l^m(\theta, \phi)] \exp(-i\omega_{nlm}t)$. Modes with $m = 0$ are called axisymmetric (or zonal) modes; these reveal l latitudinal surface nodal lines. For $|m| = l$, all surface nodal lines are lines of longitude. These modes are called sectoral modes. Modes with $0 \neq |m| < l$ are called tesseral modes and have $|m|$ longitudinal and $l - |m|$ latitudinal nodal lines. As a special case, radial oscillations have $l = 0$; i.e., they do not reveal any nodal lines on the stellar surface. The angular dependence of the radial eigenvector component (ξ_r) of some nonradial modes was graphically illustrated in Fig. 2. Space photometry has predominantly given rise to the detection of low-degree modes, typically with $l < 4$. As discussed in Fig. 2, the higher the degree of the mode, the more the detection is prone to partial cancellation due to the integration of the mode's overall perturbation over the visible stellar surface in the line of sight. The cancellation gets more pronounced as l increases, because more and smaller patches with opposite sign occur in the spherical harmonic Y_l^m that represents ξ_r . The level of cancellation also depends on the angle between the rotation axis and the line of sight (chosen as 60° in Fig. 2). The radial order of the mode, n , represents the number of nodes of ξ_r in the stellar interior, where these nodes are counted

positively for p modes and negatively for g modes. For unevolved stars, the assignment of n is straightforward in that modes with $n = 0$ have no nodes aside from the stellar center. These modes are called fundamental modes, abbreviated as f modes. For mixed modes in evolved stars, however, one could obtain $n = 0$ from the occurrence of pairs of nodes for ξ_r in the p- and g-mode cavities. Since the assignment of the radial order n is used to classify modes, such classification may be subject to quite complex issues, as explained in Sec. 3.5.2 of Aerts et al. (2010), to which we refer for more details. Further, we adopt the convention that the sign of m distinguishes prograde ($m > 0$) from retrograde ($m < 0$) modes, where the former represent motions along the rotation of the star and the latter represent motions against it.

The general system of differential equations that lies at the basis of the eigenvalue problem describing non-radial oscillation modes is of fourth order in the unknown perturbed quantities, which are ξ_r and the perturbations to the pressure δp , gravitational potential $\delta\Phi$ and the derivative of $\delta\Phi$. These equations have $Y_l^m(\theta, \phi) \exp(-i\omega_{nlm}t)$ as a common factor. Hence this factor can be divided out. The resulting ordinary differential equations to solve for the radial component of the unknown eigenfunctions do not depend on the azimuthal order m due to the assumption of having a spherically symmetric equilibrium model. This fourth-order system of equations needs four boundary conditions to be solved. However, it is often appropriate to ignore the perturbation to the gravitational potential because this perturbation is sufficiently small relative to the perturbation to the density. This is known as the Cowling approximation (Cowling, 1941). It renders the system of equations to second order and thus requires only two boundary conditions to get physically meaningful solutions. These are $\xi_r \simeq l\xi_h \sim r^{l-1}$ for $r \rightarrow 0$ and $\delta p = 0$ for $r \rightarrow R_\star$ (Unno et al., 1989). This also allows for the derivation of an analytical expression for the ratio of the horizontal to the radial displacement at the stellar surface, which depends only on the frequency of the mode:

$$\frac{\xi_h(R_\star)}{\xi_r(R_\star)} \simeq \frac{GM_\star}{\omega_{nl0}^2 R_\star^3}. \quad (35)$$

This ratio is called the ‘‘K-value’’ by observers. Typical values for this ratio are below 0.001 for high-order p modes as in the Sun and 10 – 1000 for high-order g modes of core-hydrogen-burning stars. Mathematically, the Cowling approximation is valid only for modes of high radial order n and of ‘‘high’’ degree l . One should therefore not expect this to be an optimal approximation for low-order low-degree modes, and in particular not for $l = 1, n = 0$ f modes (Sec. 3.4.1 in Aerts et al., 2010). Hence, observed stars may reveal frequency values for their f modes that do not coincide with those computed in the Cowling approximation.

The two pulsation equations resulting from adoption of

the Cowling approximation can be combined into a single approximate second-order differential equation for ξ_r as follows:

$$\frac{d^2 \xi_r}{dr^2} \simeq \frac{\omega^2}{c_s^2} \left(1 - \frac{N^2}{\omega^2} \right) \left(\frac{S_l^2}{\omega^2} - 1 \right) \xi_r, \quad (36)$$

with $N(r)$ as given in Eq.(26) and where we have introduced the following local characteristic acoustic frequency (also called the Lamb frequency) for the mode with degree l :

$$S_l^2(r) \equiv \frac{l(l+1)c_s^2}{r^2}, \quad (37)$$

with c_s the sound speed in the stellar interior. While Eq. (36) is the simplest form in which nonradial oscillations can be described, it still leads to a good approximation for the mode frequencies, and more importantly to insightful interpretations and an elegant way to introduce the so-called mode cavities. These are illustrative when plotted in propagation diagrams. Solutions for ξ_r from solving Eq. (36) are oscillatory as a function of r when (a) $|\omega| > |N|$ and $|\omega| > S_l$ or when (b) $|\omega| < |N|$ and $|\omega| < S_l$. The position inside the star where these conditions are met correspond with the zones in the stellar interior where the modes resonate inside a cavity. In this sense, the modes correspond to standing waves in their mode cavity and are said to be trapped there. The modes that meet conditions a) are dominantly restored by the pressure force and are therefore called pressure modes, usually labeled as p modes. Within their mode cavity, these modes are resonating sound waves (also called acoustic waves). By convention, we denote their number of nodes in the stellar interior as $n > 0$. Buoyancy is the dominant restoring force when conditions b) are met and these modes are therefore called gravity modes, labeled as g modes. Their radial order is denoted by $n < 0$, which means that they have $-n > 0$ nodes in the interior of the star. Within their mode cavity, they behave like low-frequency (i.e., slow) internal gravity waves with a dominant horizontal displacement in a gas that is radially stratified due to gravity. Finally, solutions for ξ_r when solving Eq. (36) have an exponential behavior when $|N| < |\omega| < S_l$ or $S_l < |\omega| < |N|$. The zones in which the modes behave exponentially are called evanescent regions and the eigensolutions decrease or increase exponentially the farther away they are from the mode cavities.

Figure 8 shows propagation diagrams for four stellar models that represent stars about halfway through their core-hydrogen-burning stage, with birth masses of 1, 1.7, 5, and $15 M_\odot$ and with solar chemical composition and mixture. The oscillation modes were computed with the open source pulsation code **GYRE** (Townsend et al., 2018; Townsend & Teitler, 2013), coupled to equilibrium models computed with the open source code **Modules for Experiments in Stellar Astrophysics (MESA Paxton**

et al., 2011, 2013, 2015, 2018, 2019). The results in Fig. 8 were obtained not by relying on the Cowling approximation but rather by from solving the fourth-order set of equations, as in modern applications of asteroseismology. The mode cavities for axisymmetric dipole ($l = 1$) and quadrupole ($l = 2$) modes are indicated, as are the mode's eigenvalues (horizontal lines) and positions of the radial nodes (dots). The importance of the receding convective core and the accompanying shape of $N(r)$ for the g-mode oscillations in intermediate- and high-mass models is visible in the lower panels of Fig. 8.

Eigenfunctions for eight modes are shown in the left and middle panels of Fig. 9 for the stellar model whose mode cavities are displayed in the upper right panel of Fig. 8. In the absence of predictive power for the mode amplitudes, we normalize the modes such that $\xi_r(R_\star) = 1$ in Fig. 9. It can be seen by comparing the left and middle panels that high-order g modes have dominant horizontal displacements, while it is the opposite for p modes. This is in line with the predictions based on the Cowling approximation. It is a general property of p and g modes. Moreover, Fig. 9 shows that p modes have higher amplitudes in the outer stellar envelope than in the inner regions, while g modes have their highest amplitude in the regions near the convective core.

The mode cavities change as a star evolves, reflecting the increased density contrast in the stellar interior. This drastically changes the profile of the sound speed $c_s(r)$ and hence the profile of $S_l(r)$ as well. As a result, the p-mode cavities decrease in frequency and the evanescent zones become narrower. Their exponential decay may hence be limited, allowing them to reach the g-mode cavity and couple to the eigenfrequencies of the g modes. Such is the case for dipole modes in red-giant stars. These modes are therefore called mixed modes: they have a p-mode character in the outer envelope and a g-mode character in the inner regions of the star. We refer to Figs. 2 to 4 in the Supplemental Material given by Aerts et al. (2019) for propagation diagrams of mixed modes in red-giant stars and refrain from repeating such diagrams here for brevity. This mixed character of these dipole modes was predicted theoretically by Dziembowski (1971) and Shibahashi (1979). Dupret et al. (2009) pointed out their probing power for the center of evolved stars following the discovery of nonradial oscillations in red giants from CoRoT (De Ridder et al., 2009), prior to their actual detection in *Kepler* data. We return to this capacity in Sec. IV.

2. Asymptotic representations of high-order modes

As discussed in Sec. III, mode identification is a critical step to be taken before any asteroseismic inference can be made. Indeed, a comparison between the detected and theoretically computed oscillation mode frequencies,

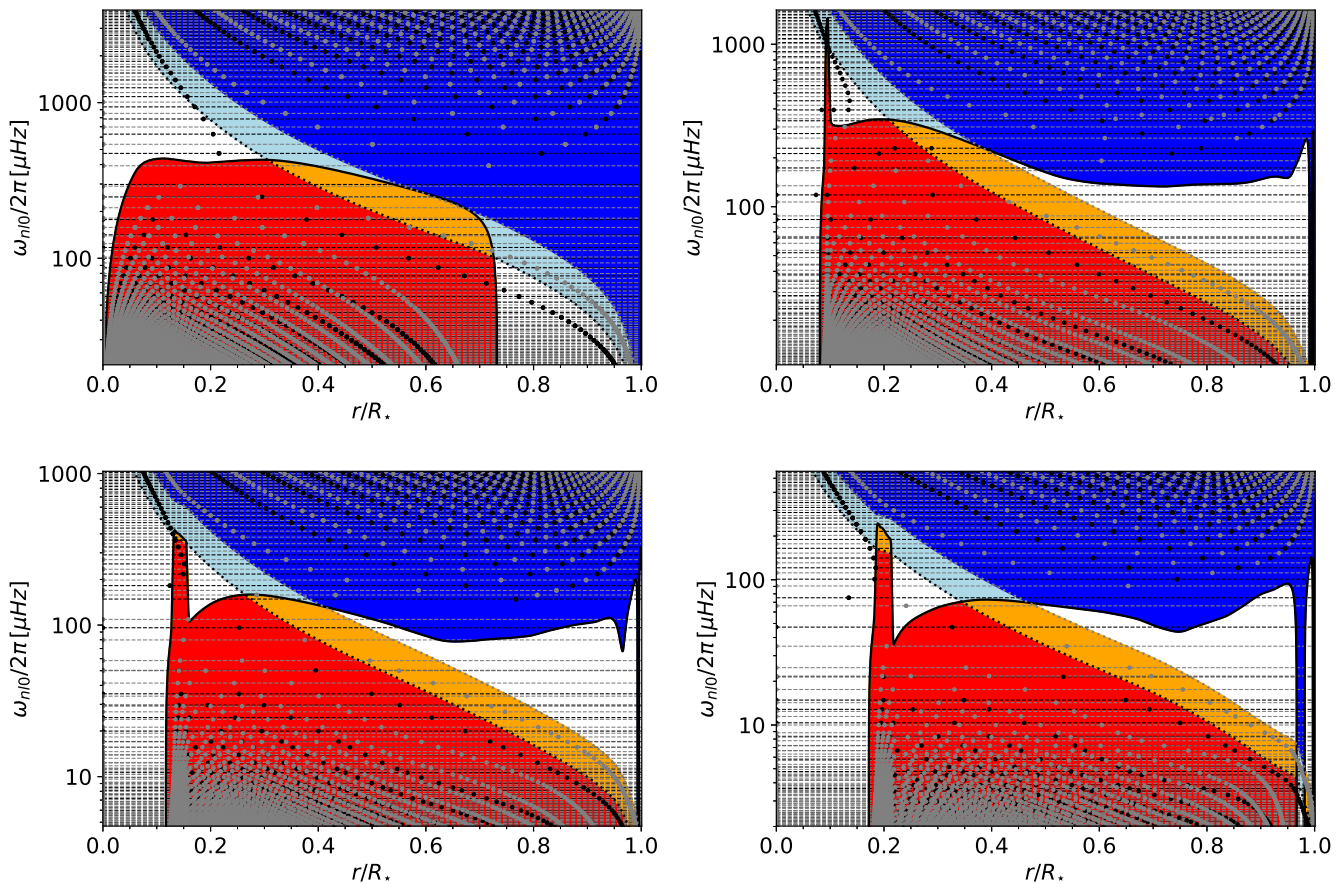


FIG. 8 Propagation diagrams showing the mode cavities of axisymmetric p and g modes in four stellar models halfway through the core-hydrogen-burning stage of evolution. The models have masses of 1, 1.7, 5, 15 M_{\odot} from top left to bottom right. The thick solid black line indicates $N(r)$, while the dotted black and gray lines represent $S_1(r)$ and $S_2(r)$, respectively. The values of the dipole (quadrupole) mode frequencies are indicated as black (gray) horizontal lines. The position of the nodes of ξ_r are indicated as thick black and gray dots for $l = 1$ and 2, respectively. The red region is the g-mode cavity for dipole modes; it is extended by the orange part for quadrupole modes. The dark blue region is the mode cavity of quadrupole ($l = 2$) p modes. It is extended by the light blue region for dipole ($l = 1$) p modes. The modes correspond to evanescent waves in the white regions in the stellar envelope. The g modes cannot propagate in the convective core of the three most massive stellar models, nor in the outer $\sim 26\%$ of the convective envelope of the 1 M_{\odot} model, where $N^2(r) < 0$. Figure courtesy of Joey Mombarg, KU Leuven.

ω_{nlm} , can be made only after the mode labels (n, l, m) have been derived. Given that we cannot resolve the surfaces of pulsating stars in sufficient detail (except for the Sun), we cannot identify the spherical wave numbers (l, m) of the nonradial modes from maps of the eigenfunctions, as in the graphical representation in Fig. 2. We somehow have to derive the mode identification from the observables. To this end, asymptotic representations of high-order modes help a great deal, although other more empirical methods for mode identification of modes exist as well (Chap. 6 in Aerts et al., 2010). Here, we limit the discussion to mode identification based on patterns deduced among the detected oscillation mode frequencies or mode periods.

The asymptotic theory of nonradial oscillations is

based on second-order differential equations describing the modes, which illustrates again why the Cowling approximation is so useful for asteroseismology. The convenience of asymptotic representations of high-order modes was initially considered for the case of linear radial modes by Ledoux (1962) (in French). He recognized that the radial-mode properties can be derived from a second-order differential equation, which constitutes a Sturm-Liouville eigenvalue problem with singular endpoints at $r = 0$ and $r = R_*$. The asymptotic properties of nonradial oscillation modes have been studied more generally ever since and are well covered in the literature, at various levels of mathematical detail. See the extensive papers by Tassoul (1980, 1990) and see Sec. 3.4 and Appendix E given by Aerts et al. (2010)

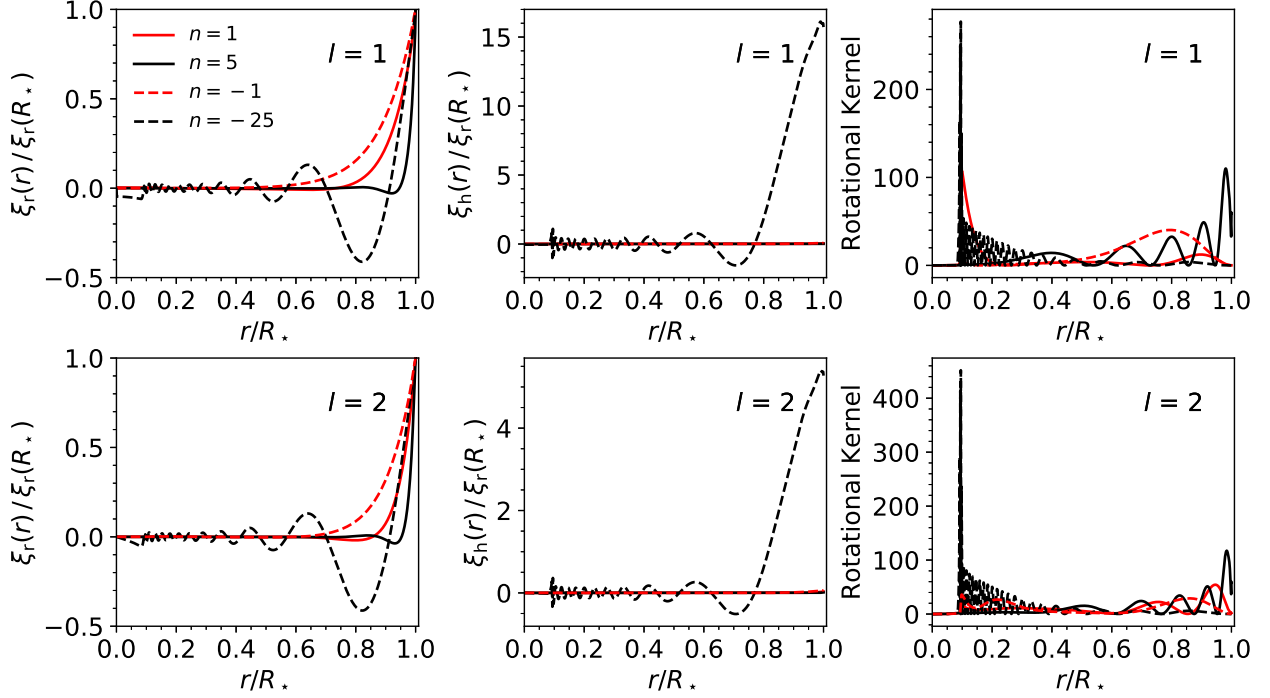


FIG. 9 Radial (left panels) and horizontal components (middle panels) of the Lagrangian displacement of four indicated axisymmetric ($m = 0$) p and g modes for $l = 1$ (top panels) and $l = 2$ (bottom panels) of a stellar model with $M_* = 1.7M_\odot$ halfway through its core-hydrogen-burning stage of evolution. The right panels show the rotation kernel defined by Eq. (45), which represents the probing power of an oscillation mode. Figure courtesy of Joey Mombarg, KU Leuven.

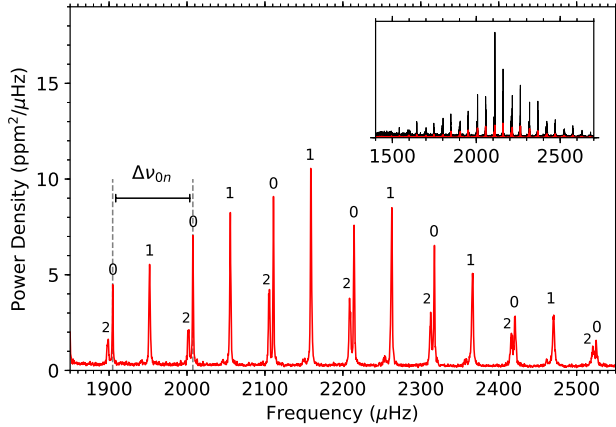


FIG. 10 Enlargement (red) of the observed envelope of oscillation signal revealed by the power density spectrum (black) of the solar analog 16 Cyg A as deduced from data assembled with the *Kepler* satellite. The p modes are labeled by their degree l . The large frequency separation based on the detected radial mode frequencies is indicated. Figure based on data in Chaplin & Miglio (2013) by courtesy of Dominic Bowman, KU Leuven.

for a general background and results. Smeyers & Van Hoolst (2010) provides in their Chaps.14–18 thorough mathematical details and comparisons for the different regimes of validity while considering different types of modes and various types of equilibrium models.

High-order p modes. We first consider the case of low-degree high-order axisymmetric p modes. To leading order in the asymptotics, the frequencies of such modes comply with

$$\nu_{nl} \equiv \frac{\omega_{nl}}{2\pi} \simeq \left(n + \frac{l}{2} + \frac{1}{4} + \alpha \right) \Delta\nu, \quad (38)$$

where we have dropped the $m = 0$ wave number in the notation and where we use the cyclic frequencies of the oscillation modes. In Eq. (38)

$$\Delta\nu = \left(2 \int_0^R \frac{dr}{c_s} \right)^{-1} \quad (39)$$

is called the large frequency separation. It is the inverse of twice the sound travel time between the center and the surface of the star. On the basis of this theoretical prediction, one expects the frequencies of the p modes with

sufficiently high n to be equally spaced and modes with the same value of $n + l/2$ to have almost the same frequency values, since $\nu_{nl} \simeq \nu_{n-1l+2}$. Such frequency patterns have indeed been observed for the solar low-degree p modes and these observational findings have given rise to the research field of helioseismology (see Christensen-Dalsgaard, 2002, for an extensive review, including historical aspects of the development of asteroseismology of “our own” star).

Given that the excitation and damping of the solar oscillations is due to the turbulent convection in its outer envelope, we expect similar asymptotic behavior for the high-order p modes of all stars with a convective envelope. This was confirmed almost two decades ago from ground-based velocity data for β Hydri (Bedding et al., 2001) and α Cen A (Bouchy & Carrier, 2001) and prior to space photometry for several tens of stars (Aerts et al., 2010). Space photometry confirms that stars with a convective envelope comply with asymptotic theory, from dwarfs to the bottom of the asymptotic giant branch. One of the best datasets of solarlike oscillations in a star different from the Sun was assembled for 16 Cyg A; its PD spectrum in Fig. 10 illustrates the validity of the asymptotic theory.

Equation (38) is based on the dominant term in the asymptotic representation of low-order p modes. The second-dominant term in the expansion leads to the so-called small frequency separation, given by

$$\delta\nu_{nl} \equiv \nu_{nl} - \nu_{n-1l+2} \simeq -(4l + 6) \frac{\Delta\nu}{4\pi^2\nu_{nl}} \int_0^R \frac{dc_s}{dr} \frac{dr}{r}, \quad (40)$$

where $c_s(R_\star) \simeq 0$ was assumed to arrive at this approximation. From this expression, it is clear that $\delta\nu_{nl}$ probes the sound-speed gradient in the deep stellar interior. For stars in the core-hydrogen-burning stage, dc_s/dr is highly sensitive to the hydrogen and helium composition profiles, which are directly impacted by the nuclear fusion. It is then readily understood that $\delta\nu_{nl}$ is of major diagnostic value to estimate the age of the exoplanet host star by comparing its observed values with predictions of this quantity based on equilibrium models. In the case of 16 Cyg A, as can be seen in Fig. 10, $\delta\nu_{nl}$ can be measured with high precision from the radial and quadrupole modes. This, and more sophisticated diagnostics for additional modes, was used by Bellinger et al. (2017) to find an asteroseismic estimate of $\tau = 6.9 \pm 0.4$ Gyr. This is in excellent agreement with other methods for this well-characterized bright exoplanet host binary (Maia et al., 2019).

The similarity of the nonradial oscillations of 16 Cyg A to those of the Sun as illustrated in Fig. 10, is representative of low-mass dwarfs with convective envelopes. This observational finding is of key diagnostic importance to estimate stellar masses, radii, and ages of such stars, as we discuss further in Sec. IV.

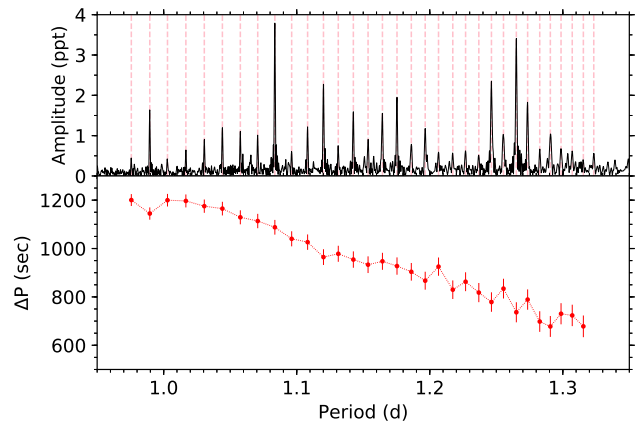


FIG. 11 Top panel: observed amplitude spectrum (black) in terms of the period for the γ Dor star KIC 11721304 from its light curve observed with the *Kepler* satellite. The mode periods with dominant amplitude are indicated with red dashed vertical lines as a guide for the eye. Bottom panel: period-spacing pattern deduced from the dipole sectoral prograde modes of consecutive radial order n indicated in the top panel. Figure based on data in Van Reeth et al. (2015) by courtesy of Timothy Van Reeth, KU Leuven.

High-order g modes. For high-order low-degree axisymmetric g modes, $\omega \ll N$ over most of the mode cavity; cf. Fig. 8. We denote with r_1 and r_2 the inner and outer positions of the g-mode cavity. In this case, the asymptotic analysis based on the Cowling approximation by Tassoul (1980) led to

$$P_{nl} = \frac{\Pi_0}{\sqrt{l(l+1)}} (|n| + \alpha_{l,g}), \quad (41)$$

where

$$\Pi_0 \equiv 2\pi^2 \left(\int_{r_1}^{r_2} N \frac{dr}{r} \right)^{-1}. \quad (42)$$

The quantity Π_0 stands for the buoyancy travel time and represents a characteristic period for the g modes of the star (as inverse of a frequency, it is expressed in the unit of time). In this case, the mode periods are asymptotically equally spaced in the order of the mode and the period-spacing value decreases with increasing l . The phase term $\alpha_{l,g}$ depends on whether the star has a radiative or a convective core.

Long before space asteroseismology, g-mode period spacing patterns have been extensively exploited for pulsating white dwarfs, based on photometric data assembled with the Whole Earth Telescope (Winget et al., 1991, 1994). The short periods of their g modes (a few to tens of minutes) imply beating patterns in the light curves of only a few days, while the modes may have high amplitudes of percentage level. This led to the

detection of tens of dipole and quadrupole modes that are subject to strong mode trapping in the outer thin H and He layers of these objects, where $N(r)$ experiences spikes due to strong changes in μ . In the context of white dwarfs, polytropes can be taken as equilibrium models, leading to analytical expressions for $\alpha_{l,g}$ that allow detailed interpretation of the mode trapping in terms of the chemical composition and mass of the outer layers of such pulsators (Brassard et al., 1992, for a seminal paper). Ground-based asteroseismology was therefore already highly successful for white dwarfs in the early 1990s.

For applications to SPB stars and γ Dor stars, which are both core-hydrogen-burning g-mode pulsators with a convective core (cf. Figs. 1 and 8), $\alpha_{l,g} = \alpha_g$ turns out to be independent of the mode degree l and one gets $\Delta P \equiv P_{nl} - P_{n-1l} = \Pi_0 / \sqrt{l(l+1)}$. Smeyers & Moya (2007) provided more sophisticated asymptotic analyses based on the full fourth-order theory of nonradial oscillations; i.e., they omitted the Cowling approximation. They developed the asymptotic approximations for both the cases of a radiative (SPB stars) and a convective (γ Dor stars) envelope. Although they derived more complicated expressions, the patterns to be expected from observations are well captured by Eq. (41). However, the number of nodes may differ by 1 compared with the simpler treatment from Tassoul (1980) based on the Cowling approximation. This implies that one should consider an uncertainty in the assignment of the radial order n by at least 1 in any practical asteroseismic modeling based on observed g-mode period spacings. In general, modern pulsation codes usually adopt the Takata (2012) classification scheme to assign the radial order n to modes.

The period-spacing pattern of high-order g modes offers a direct probe of the physical conditions in the region near the convective core of main-sequence stars. This offers interesting applications to assess the mixing at the bottom of the radiative envelope of core-hydrogen-burning stars, which is one of the major uncertainties in the theory of stellar evolution, as discussed in Sec. II.A. A seminal paper on this probing capacity was written by Miglio et al. (2008). In retrospect, this paper offered a remarkable sneak-preview of the major insights to come from g-mode space asteroseismology when turned into practice. Aside from the somewhat controversial detection and interpretation of g modes in the Sun (García et al., 2007), the first g-mode period-spacing pattern detection for an intermediate-mass dwarf came from CoRoT data of the $\sim 7 M_\odot$ B3V star HD 50230. Eight axisymmetric g modes with consecutive radial order could be deduced from a 137-d-long light curve by Degroote et al. (2010a). This star revealed periodic deviations from a uniform spacing, which is in line with the theoretical predictions by Miglio et al. (2008). This detection allowed researchers to assess the level of D_{ov} and to derive an upper limit for $D_{mix}(r)$ in the radiative

envelope. These results were confirmed by independent asteroseismic modeling by Wu & Li (2019).

Given the immense asteroseismic potential of g-mode period-spacing patterns, the CoRoT discovery opened the floodgates in the hunt for such patterns in SPB and γ Dor stars, once the 4-yr light curves of the *Kepler* spacecraft became available. Meanwhile Π_0 has been measured for hundreds of stars, one of which is shown in Fig. 11. It can be seen that a clear pattern emerges from the data but that ΔP is not constant as predicted by Eq. (41). Rather, it decreases for increasing mode period and reveals substructures. Such “tilted” ΔP patterns turn out to be common in *Kepler* data of SPB stars as found by Pápics et al. (2015, 2017) and Szewczuk & Daszyńska-Daszkiewicz (2018) and of γ Dor stars as revealed by Van Reeth et al. (2015), Bedding et al. (2015), Keen et al. (2015), Ouazzani et al. (2017), and Li et al. (2019b,c, 2020). The slope in these observed g-mode ΔP patterns is caused by the rotation frequency of the star as deduced by Van Reeth et al. (2016), Ouazzani et al. (2017), Christophe et al. (2018), and Li et al. (2020). This rotation frequency turns out to be of a similar order as the g-mode frequencies and puts these modes into the gravito-inertial regime (Aerts et al., 2017b). This implies the need to include the Coriolis force into the theory at the level of the pulsation equations for a proper asteroseismic interpretation. We do so in the next two sections, following the recent review on angular momentum transport by Aerts et al. (2019) which includes more details and illustrations.

3. Rotational splitting in a perturbative approach

Thus far we have simplified the equations to compute the stellar oscillations by ignoring the stellar rotation. Rotation affects the observed oscillation frequencies in several ways. We choose a reference frame with the polar axis along the rotation axis of the star and corotating with the star under the assumption of a constant rotation frequency Ω . This leads to a purely geometric shift of

$$\omega_{nlm} = \omega_{nl} + m\Omega \quad (43)$$

for a mode with frequency ω_{nl} in the nonrotating case. Further, both the Coriolis and centrifugal forces come into play in the stellar structure equations; see Eq. (30). The Coriolis force lifts the degeneracy of the modes in the star with respect to the azimuthal order m . Each mode frequency ω_{nl} of the eigenvector $\xi_{nl} = (\xi_{r,nl}, \xi_{h,nl})$ for the nonrotating case gets split into $2l + 1$ frequency multiplet components due to the influence of the Coriolis force. Hence, each mode degree l can occur with $2l + 1$ different values for m , namely $-l, -l + 1, \dots, -1, 0, 1, \dots, l - 1, l$. Moreover, each of these multiplet components gets shifted over $m\Omega$ as in Eq. (43) in the inertial coordinate system of the observer.

We now consider the case where the so-called spin parameter $s = 2\Omega/\omega \ll 1$ for all involved mode frequencies, with ω an abbreviated global notation for the oscillation frequencies in the corotating frame. This allows us to treat the Coriolis force as a small perturbation in the pulsation equations. This condition is usually met for p modes in low-mass stars with convective envelopes, for p and mixed modes in red giants, and for g modes in subdwarfs and white dwarfs, all of which are slow rotators. This simplification is not justified for the g modes observed in the majority of intermediate- and high-mass dwarfs, as these modes occur in the gravito-inertial regime and require the Coriolis force to be treated nonperturbatively (Aerts et al., 2017b). We return to the case of gravito-inertial modes later but first treat the easier case of a perturbative treatment of the Coriolis force.

Following the same arguments as for the shellular rotation, we simplify the problem to be solved by assuming that the rotation profile depends only on the radial coordinate $\Omega(r)$. In this case, multiplet components in the inertial coordinate system are, up to first order in $\Omega(r)$, given by (see Chapter 6 and Sec. 3.8 in Aerts et al., 2010; Unno et al., 1989, for the derivations)

$$\omega_{nlm} = \omega_{nl} + m(1 - C_{nl}) \int_0^R K_{nl}(r)\Omega(r)dr, \quad (44)$$

where

$$K_{nl}(r) = \frac{(\xi_r^2 + [l(l+1)]\xi_h^2 - 2\xi_r\xi_h - \xi_h^2)r^2\rho}{\int_0^R (\xi_r^2 + [l(l+1)]\xi_h^2 - 2\xi_r\xi_h - \xi_h^2)r^2\rho dr}, \quad (45)$$

is the rotational kernel and

$$C_{nl} = \frac{\int_0^R (2\xi_r\xi_h + \xi_h^2)r^2\rho dr}{\int_0^R (\xi_r^2 + [l(l+1)]\xi_h^2)r^2\rho dr} \quad (46)$$

is the Ledoux constant (Ledoux, 1951). Rotational kernels for dipole and quadrupole modes of four radial orders are plotted in the right panels of Fig. 9 for a $1.7 M_\odot$ star halfway through its core-hydrogen-burning stage. It can be seen that the high-order g modes have far better probing potential for the core regions of the star than the low-order modes. It is then understood from the profile shape of $K_{nl}(r)$, which acts as a weighting function to the rotation profile, why it is far easier to estimate the near-core values of $\Omega(r)$ than the envelope values for g modes in stars with a convective core and a radiative envelope, once rotational splitting has been detected from data. Finally, we see from Eqs. (45) and (46) that they depend on the equilibrium model via its density profile $\rho(r)$ and its influence on the eigenfunctions.

In the limit of high-order or high-degree p modes, one can show that $C_{nl} \simeq 0$ and $\xi_r > \xi_h$ (Aerts et al., 2010, Sec. 3.8). On the other hand, for high-order high-degree g modes, one has $\xi_r < \xi_h$ as shown in Fig. 9 and one may

neglect the terms with ξ_r in Eqs. (45) and (46). In this way, the simplification

$$C_{nl} \simeq \frac{1}{[l(l+1)]} \quad (47)$$

emerges. For uniform rotation, this implies that the measured rotational splitting provides a good measure of the average of $\Omega(r)$, weighted with the squared eigenfunction. A further simplification is useful, as Van Reeth et al. (2018) showed that intermediate-mass stars with a convective core are quasiuniform rotators. In the case of constant Ω one has

$$\omega_{nlm} = \omega_{nl} + m(1 - C_{nl})\Omega \quad (48)$$

and C_{nl} fully determines the shifts of the frequencies due to the Coriolis force, i.e., those shifts do not depend on the rotational kernels. This means that the adjacent frequencies in a high-order p-mode multiplet belonging to $m = -l, \dots, +l$ give a direct measure of the average rotation frequency in the stellar envelope, without depending on the equilibrium model (because $C_{nl} \simeq 0$). In the case of high-order dipole g modes, Ω is found to be twice the splitting value in a triplet since $C_{nl} \simeq 1/2$.

More complicated perturbative approaches treating the Coriolis force up to second and third order at the level of the pulsation computations, while still relying on 1D equilibrium models, have been developed. We refrain from including the results here for conciseness and refer the interested reader to Saio (1981), Dziembowski & Goode (1992), Lee & Baraffe (1995), Soufi et al. (1998), Daszyńska-Daszkiewicz et al. (2002), Suárez et al. (2006), and Suárez et al. (2010). Few of those theories have been applied to modern space photometric data because the stars for which they are most appropriate are rapidly rotating p-mode pulsators, such as δ Sct stars and β Cep stars; cf. Fig. 1. In the case of the δ Sct stars, lack of mode identification prevents applications, although Bedding et al. (2020) managed to overcome this hurdle for a limited sample of such stars. The few observed β Cep stars with precise space photometry either lack mode identification (Burssens et al., 2019) or rotate slow enough to stick to the first-order perturbative approach. Suárez et al. (2010) made a careful analysis of second-order effects in Ω for stochastic p modes and found those to become important for equatorial rotation velocities above some 15 km s^{-1} . This is also the limiting value for the treatment of g modes in intermediate-mass stars derived by Schmid & Aerts (2016). For rotation speeds above this value, a perturbative analysis should be abandoned as illustrated from their asteroseismic modeling of the high-order g modes in the two F-type p- and g-mode hybrid pulsators in the eccentric binary KIC 10080943. For faster rotation, the g modes enter into the gravito-inertial regime, where one can no longer treat the Coriolis force perturbatively ($s > 1$). As outlined

by Aerts et al. (2017b) and shown in Fig. 6, this is the case for the observed g modes in almost all intermediate- and high-mass stars. We thus conclude that the treatment of g modes in stars with a convective core requires a nonperturbative treatment of the Coriolis force.

4. Gravito-inertial modes in the Traditional Approximation

A major achievement resulting from the 4-yr light curves assembled with the *Kepler* satellite is the discovery of g modes with period-spacing patterns such as the one illustrated in Fig. 11 in hundreds of stars covering spectral types early-F to early-B along the main sequence; cf. Fig 1. Except for the few (less than 10%) stars for which a surface magnetic field was detected in this range of spectral type (Wade et al., 2016), such stars are in general moderate to fast rotators. They are indeed not subject to braking due to the lack of a magnetic field, which does occur in low-mass stars with an appreciable convective envelope. The high-order g modes in these stars of intermediate mass have periods similar to their rotation period so the oscillations are gravito-inertial modes (see Fig. 5 given by Aerts et al., 2019). Van Reeth et al. (2016) and Aerts et al. (2017b) computed the spin parameters for more than 1650 g modes in 37 γ Dor stars and found the majority to have subinertial values, defined as the regime for which $s > 1$. In practice, the spin parameter covered values $s = 2\Omega/\omega_{nlm}^{\text{co}} \in [1, 15]$, where ω_{nlm}^{co} is the mode frequency in the corotating frame.

Taking full account of the Coriolis force in the equation of momentum conservation, even in the adiabatic and Cowling approximations while ignoring the centrifugal force, does not lead to separability of the pulsation equations in terms of the coordinates (r, θ, ϕ) . This is why Lee & Saio (1987a,b, 1989) considered the so-called ‘‘Traditional Approximation of Rotation’’ (TAR) in their theoretical studies of low-frequency g modes. In the TAR, one ignores the horizontal component of the rotation vector such that the equations can be separated in each of the coordinates. This approximation leads us to the Laplace tidal equations (Laplace, 1799), which are commonly used in geophysics (Eckart, 1960). The TAR is a particularly good approximation for the g modes in intermediate- and high-mass main-sequence stars (as well as in neutron stars, cf. Bildsten et al., 1996), given that their Lagrangian displacement vector is dominantly horizontal; see Fig. 9. For derivations of the pulsation equations in the TAR and their asymptotic analysis in a modern numerical context, see Lee & Saio (1997), Townsend (2003a,b), and Mathis (2013). Here we provide the outcome in concise notation that allows for easy comparison with Eq. (41). For uniform rotation, the TAR leads to the following g-mode period-spacing pattern in the corotating frame of reference:

$$\Delta P_{l,m,s}^{\text{co}} = \frac{\Pi_0}{\sqrt{\lambda_{lms}}}, \quad (49)$$

with λ_{lms} the eigenvalue of the Laplace tidal equation for the g mode with quantum numbers (l, m) in a star with spin parameter s . In the limit of $s \rightarrow 0$, $\lambda \rightarrow l(l+1)$ is recovered. Numerical computation of the eigenvalues λ_{lms} for a chosen 1D equilibrium model of the star then allows for the identification of (l, m) , as well as estimation of the spin parameter along with Ω from an observed period-spacing pattern as in Fig. 11. This opportunity was developed theoretically by Bouabid et al. (2013) and was put into practice for the past five years after careful frequency analysis based on the 4-yr light curves assembled with the *Kepler* spacecraft. We highlight some of the recent achievements on asteroseismic derivations of $\Omega(r)$ along with opportunities to estimate $D_{\text{mix}}(r)$ from the period-spacing diagnostics in Sec. IV.

Mathis (2009) generalized the TAR to take into account differential rotation with a profile $\Omega(r, \theta)$, while Mathis & Prat (2019) included the centrifugal force for slightly deformed stars in the case of close-to-uniform rotation, deriving an analytical expression for the period spacing patterns in the Cowling and other justified approximations. In addition, Prat et al. (2017) derived an asymptotic period spacing for axisymmetric gravito-inertial waves taking into account all the components of the rotation vector; i.e., they went beyond the treatment of the TAR. This work was further generalized by Prat et al. (2018) into an asymptotic theory for gravito-inertial waves for a differential rotation profile $\Omega(r, \theta)$. Finally, Prat et al. (2019) derived a period-spacing expression in the presence of uniform rotation on top of an axisymmetric fossil magnetic field with poloidal and toroidal components. None of these recent new theoretical developments have yet been applied to measured g-mode frequencies. This obviously constitutes several future paths for improved asteroseismic modeling compared to the current state of the art. The *Kepler* data of gravito-inertial pulsators are currently under study with this purpose.

As a noteworthy side step, we point out that only one intermediate-mass g-mode pulsator with a detected surface magnetic field has been the subject of magnetogravitational asteroseismology thus far (Buysschaert et al., 2018). This led to the conclusion that the frequency shifts for g modes due to the Lorentz force are far smaller than those due to the Coriolis force for meaningful values of the interior magnetic field strength (Prat et al., 2019). This is quite different from the case of high-frequency magnetoacoustic modes, which occur on the other side of the frequency spectrum in terms of the validity (or lack thereof) of a perturbative approach to treat the Coriolis and Lorentz forces (see Fig. 5 in Aerts et al., 2019). Inspired by the solar oscillations, Gough & Thompson (1990) derived expressions for the perturbation to the

eigenfunctions caused by rotation and a magnetic field in the stellar interior. Their asymptotic analysis and numerical results for high-order solar acoustic modes for various magnetic field configurations, including a localized magnetic field at the base of the convection zone, provide estimates for the frequency splitting when the magnetic field and rotation vary smoothly. This work is a convenient guide to compare with observations.

Aside from Sun-like stars, the best known magnetic pulsators are the roAp stars, which were discovered in 1978 by Don Kurtz (Kurtz, 1990, for his review on these stars) and later studied in great detail (Saio, 2014, for a more recent review). These core-hydrogen-burning stars oscillate in high- n low- l p modes according to an axis that may be misaligned with respect to both the magnetic and rotation axes, although it is usually close to the magnetic axis. Their magnetic field strengths are up to a few thousand gauss, while they are slow rotators and this implies that the Lorentz force is more important than the Coriolis force. This is thus a case where the symmetry axis for the oscillations is inclined with respect to the rotation axis. Although their magneto-acoustic modes have sufficiently high amplitudes and periods of only a few minutes, making them easily accessible from ground-based asteroseismology, their recent studies have benefited greatly from modern space photometry. The oblique pulsator model of roAp stars has constantly been in need of improvement as more data become available, as shown by Shibahashi & Takata (1993) and Bigot & Dziembowski (2002). This model was again challenged and refined thanks to the high-frequency precision obtained from space asteroseismology, which revealed that some roAp stars seem to have multiple pulsation axes (Kurtz et al., 2011) and others oscillate in distorted pulsation modes (Holdsworth et al., 2016). Recent TESS data have been used to find the shortest period roAp star, with a pulsation period of only 4.7 min (Cunha et al., 2019a). A growing number of roAp stars have been found to pulsate above their acoustic cutoff frequency, which presents another challenge to current pulsation theory.

5. Rossby modes

We now return to the maximally simplified version of the stellar pulsation equations deduced from perturbing Eq. (19) in the absence of rotation and magnetism. This approach allowed us to introduce the time-dependent spheroidal modes of oscillation known as p and g modes. However, if we keep the Coriolis force in Eq. (19) and perturb that version of the equation, then two families of eigenvalue problems actually result, each with nonzero eigenvalues. The first family is the one we have been discussing, leading to spheroidal normal modes of a star. We now pick up the second family of eigensolutions, termed toroidal normal modes. In particular, we con-

sider the Rossby modes, also termed and abbreviated as “r modes” by Papaloizou & Pringle (1978). This is a family of toroidal normal modes that become time-dependent (and hence nonzero) only in a rotating star. The dominant restoring force of these modes is the Coriolis force. This is why they cannot be deduced from Eq. (19) unless a nonzero rotation vector is considered.

Toroidal modes comply with $\text{div } \xi = 0$ and $\xi_r = 0$. Therefore, just as with the gravito-inertial modes discussed in the previous section, the eigenvalues of Rossby modes can be deduced with excellent precision by adopting the TAR and solving the Laplace tidal equations. For the eigenfrequencies of the spheroidal g modes we had the limiting case of $\lambda \rightarrow l(l+1)$ as $s \rightarrow 0$. For the Rossby modes, one obtains $\lambda \rightarrow 0$ as $s \rightarrow [l(l+1)]/m$ (Papaloizou & Pringle, 1978). For this reason, Lee & Saio (1997) adopted an ordering of the eigenvalues by introducing a labelling scheme that allows one to treat the cases of gravito-inertial g modes and pure inertial modes with one set of indices (k, m) , with $k = l - |m| \geq 0$ for gravito-inertial modes and $k < 0$ for purely inertial modes (see the seminal paper by Townsend, 2003b, for the various types of low-frequency modes in rotating pulsators). Rossby modes have frequencies below the rotation frequency in the corotating frame and are therefore always retrograde modes in the inertial frame of the observer (Saio, 1982). The occurrence of the temperature variations at the stellar surface due to Rossby modes and for various values of the spin parameter is shown in Fig. 2 given by Saio et al. (2018b) and omitted here for conciseness.

With the labeling scheme introduced by Lee & Saio (1997), the period-spacing pattern of Rossby modes becomes

$$\Delta P_{kms}^{\text{co}} = \frac{\Pi_0}{\sqrt{\lambda_{kms}}}, \quad (50)$$

with λ_{kms} again the eigenvalues of the Laplace tidal equation. It was shown by Townsend (2003a) that the eigenvalues for Rossby modes comply with $\lambda_{kms} \approx m^2(2|k| - 1)^{-2}$ for $s \gg 1$ and $k \leq -2$. From this, it is found that the period-spacing value of Rossby modes of consecutive radial order as seen by an observer increases with increasing mode period. This is illustrated for the γ Dor star KIC 12066947 observed by the *Kepler* spacecraft in Fig. 12. This star has both prograde gravito-inertial dipole modes with $k = 0$ and retrograde Rossby modes with $k = -2$. For its sectoral gravito-inertial g modes, just as for the ones observed for KIC 11721304 shown in Fig. 11, the label is $k = 0$ and we recover the treatment of the period-spacing pattern represented by Eq. (49).

Van Reeth et al. (2016) made the first discovery of Rossby modes in *Kepler* data. This was achieved for ten γ Dor stars, all of which were found to have spin parameters $s \in [14, 30]$ (Aerts et al., 2017b). Meanwhile, Rossby modes were found to be common in F-, B-, Be-, and A-type stars, as well as in eccentric binaries, all of which

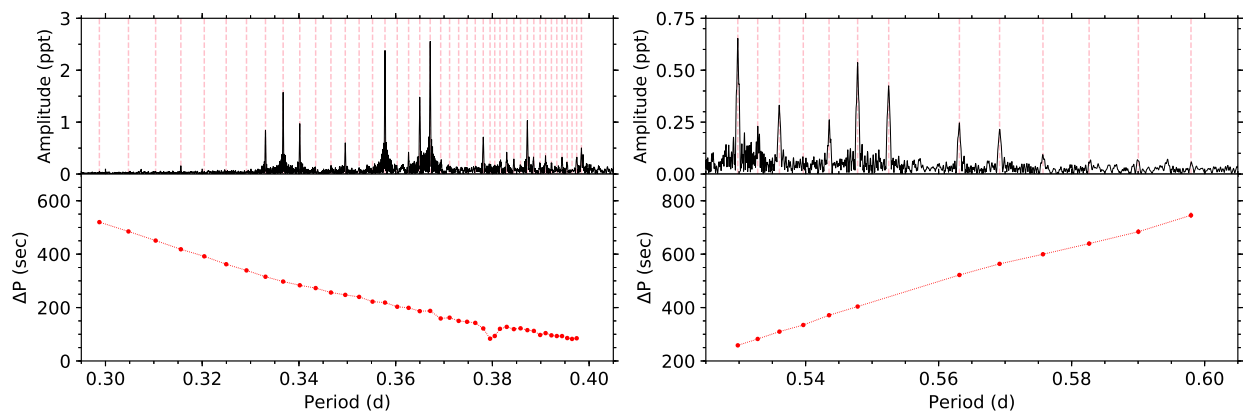


FIG. 12 Same as Fig. 11, but for the γ Dor star KIC 12066947 exhibiting both prograde dipole gravito-inertial modes with $(k, m) = (0, +1)$ and retrograde Rossby modes with $(k, m) = (-2, -1)$. In contrast to the case of KIC 11721304 shown in Fig. 11, the errors in the period-spacing pattern are smaller than the symbol size. Figure based on data in Van Reeth et al. (2015) by courtesy of Timothy Van Reeth, KU Leuven.

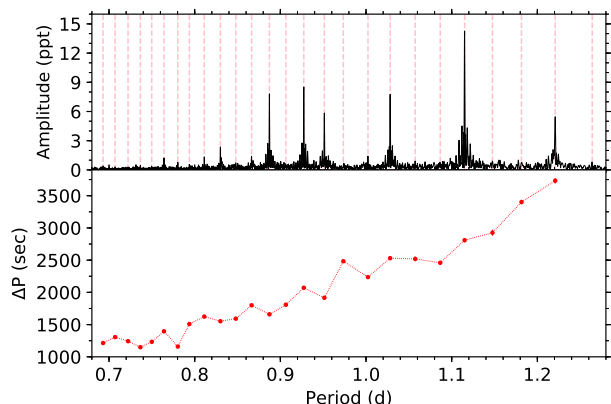


FIG. 13 Same as Fig. 11, but for the γ Dor star KIC 6425437 exhibiting retrograde Yanai modes with $(k, m) = (-1, -1)$. In contrast to the case of KIC 11721304 shown in Fig. 11, the errors in the period-spacing pattern are smaller than the symbol size. Figure based on data in Van Reeth et al. (2015) by courtesy of Timothy Van Reeth, KU Leuven.

were observed with the *Kepler* spacecraft and studied by Saio et al. (2018b) and Li et al. (2019c). These discoveries offer the opportunity to assess whether the interior rotation is constant or differential from combined g- and r-mode asteroseismology. We also note in passing that retrograde Yanai modes were discovered in *Kepler* data of seven γ Dor stars so far by Van Reeth et al. (2018) and Li et al. (2019c). As explained by Townsend (2003a), this family of modes behaves like gravito-inertial modes when they are prograde, while the retrograde Yanai modes behave as Rossby modes but have $k = -1$. We show the results for KIC 6425437, which is one such star revealing a period-spacing pattern of Yanai modes, in Fig. 13 (Van

Reeth et al., 2018). Just as with the Rossby modes, the full potential of Yanai-mode frequencies in terms of asteroseismic probing of the properties of the interior physics has yet to be investigated and exploited, given their recent discoveries.

III. PRINCIPLES OF ASTEROSEISMIC MODELING

The theory of nonradial oscillations outlined in Sec. II rests on the assumption of linearity. Although the amplitudes of stochastically excited modes of the Sun can now be predicted from the damping rate and the stochastic energy from 3D convection simulations (Zhou et al., 2019), this is not the case for the amplitudes of the modes excited by other mechanisms. Thus, most interpretations in asteroseismology rely on the properties of the detected mode frequencies and not on their amplitudes. Asteroseismic modeling is therefore usually done in a linear adiabatic framework. After having derived the frequencies of the modes ω and their uncertainty σ_ω from data, interpretations in terms of the theory of nonradial oscillations computed from perturbing stellar equilibrium models (see Sec. II) can be done only if the modes' identifications have been achieved. This means that we must be able to label the radial order, the degree, and the azimuthal order (n, l, m) for each of the modes corresponding to the measured oscillation frequencies $\omega_{nlm}^{\text{obs}}$.

Mode identification is usually based on patterns recognized from the list of adiabatic frequencies $\omega_{nlm}^{\text{theo}}$, predicted from the perturbation of 1D equilibrium models as outlined in Sec. II. Easily interpretable patterns concern those due to rotational splitting or corresponding to the predictions from the asymptotic theory, as outlined in Sec. II. Comparison between predicted and detected patterns such as those shown in Figs. 10 – 12 can then

be fed with the “wisdom” of the applicant to identify (n, l, m) . This wording already indicates why asteroseismologists tend to be “Bayesianminded” when identifying modes and performing asteroseismic modeling (see Gruberbauer et al. (2012), Bazot et al. (2012), Appourchaux (2014), and Aerts et al. (2018b) for thorough discussions). Nevertheless, MLE and model selection with so-called noninformative (flat) priors is often enlightening and sometimes necessary to avoid too much prejudice in the prior, particularly on the appropriateness of the equilibrium models used to compute the mode predictions.

Despite our inability to predict reliably which of the eigenmodes should get excited to observable amplitudes, the mode excitation mechanisms are understood in general terms for the classes in Fig. 1. Therefore, even though the nonadiabatic treatment of the oscillations is not sufficiently established to derive perfect mode excitation and amplitude predictions, it is still instructive to consider the regimes of mode excitation before tackling the task of mode identification and asteroseismic modeling.

A. Excitation mechanisms

1. Heat mechanisms and stochastic driving

Thus far we have ignored the perturbation of the entropy in Eq. (21), which greatly simplifies the theory of nonradial oscillations. However, to get an understanding of mode excitation, nonadiabatic theory needs to be considered. This is extensively discussed in Chaps. IV and V given by Unno et al. (1989) and also in Aerts et al. (2010, Sec. 3.7), which addressed the general problem and the development of the so-called quasiadiabatic approximation. The prediction for a mode to get excited relies on the computation of its growth rate. This quantity is positive for modes that get excited (or modes that are unstable, as is often used as terminology), while it is negative for modes that are overdamped. Derivation of the growth rate of a mode requires the computation of the imaginary part of its eigenfrequency (see Eq. (3.282) given by Aerts et al., 2010). When considering the theoretical expression, one finds that excitation occurs whenever the compression of the gas and its heating happen in phase with each other. This is completely in line with the operation of a thermodynamical heat engine.

The perturbations to both the flux (radiative + convective, $\mathbf{F} = \mathbf{F}_{\text{rad}} + \mathbf{F}_{\text{conv}}$) and the energy generation stemming from Eq. (21) go into the overall expression for the heat. For each of these three contributions, one adopts a specific terminology. When the perturbation of the energy generation is dominant in the heat term that sets the imaginary part of the mode frequency [see Eq. (21)] the ε mechanism may operate. This can obviously happen only in the deep stellar interior. In the case in which

the radiative flux delivers most of the heat, it is often due to the increased opacity that acts as the heat engine in the thin partial ionization layers in the envelope of the star. This driving of oscillations is therefore often called the κ mechanism, giving rise to self-excited modes with infinite lifetimes. Theoretical predictions of nonradial mode excitation via the κ mechanism in intermediate-mass stars along the main sequence are generally good. Pamyatnykh (1999), Bouabid et al. (2013), and Szweczek & Daszyńska-Daszkiewicz (2017) conducted extensive studies. Yet they are not perfect: we observe more modes than predicted for OB-type pulsators, particularly in the g-mode regime. Bringing theory and observations into agreement requires either higher-than-standard opacities in the partial ionization zones of ironlike species situated in the layers with temperatures $\sim 2 \times 10^5$ K, as shown by Moravveji (2016) and Daszyńska-Daszkiewicz et al. (2017), or higher metal abundances in the local region of the excitation (for instance, as a consequence of atomic diffusion). Similarly, iron and nickel opacity enhancements are needed to explain the g modes observed in cool pulsating subdwarf B stars, as emphasized by Fontaine et al. (2003), Jeffery & Saio (2006), and Bloemen et al. (2014). Their hotter counterparts were predicted theoretically by Charpinet et al. (1997) in terms of p modes excited by the κ mechanism at about the same time as, but independently of their observational discovery by Kilkenny et al. (1997). Opacity bumps due to carbon- and oxygen in layers of $\sim 10^6$ K result in heat-driven mode excitation of helium-rich subdwarfs (Saio & Jeffery, 2019) and GW Vir variables (also known as DO white dwarfs). Córscico et al. (2019) provided a recent summary of pulsating white dwarfs, and Montgomery et al. (2020) inferred nonstatic convection zones in white dwarfs from observational limits on their mode coherence.

The perturbation to the convective flux and its contribution to the heat presents a much larger challenge than the case of radiative flux, because it is coupled to the properties of the turbulent pressure. For the deep stellar interior, one may assume that this is time independent and well described by mlt. However, for convective outer envelopes, the perturbations to the convective flux and the turbulent pressure render the modes stable, such that the heat-engine mechanism does not drive oscillations. Instead, excitation occurs through stochastic forcing, where the energy in the acoustic noise in the outer convection zone triggers some of the global eigenmodes. This stochastic forcing happens in stars with an outer convective envelope, leading to the excitation of damped and continuously reexcited oscillation modes. In this case, predictions of the excitation and properties of the modes are challenging due to the limited knowledge of the time-dependent properties of \mathbf{F}_{conv} in the equilibrium models. This propagates into theoretical uncertainty for the perturbation of the time-variable con-

vective envelope of a pulsating star.

In the limit of extremely long convective timescales relative to the periods of the oscillations, the convective flux does not react to the pulsations and convective flux blocking becomes an efficient excitation mechanism. This excites g modes in the thin convective envelopes of the γ Dor stars as shown by Guzik et al. (2000) and further elaborated upon by Dupret et al. (2005). Gravitoinertial modes in the radiative envelope of such stars may couple resonantly to inertial modes in the convective core of rapid rotators (Ouazzani et al., 2020). On the other hand, Lee & Saio (2020) found mode excitation due to resonant coupling between convective g^- modes active in the core of rapidly rotating $2M_{\odot}$ stellar models and g modes in the radiative envelope, for frequencies $|m|\Omega_{\text{core}}$. For the intermediate-mass δ Sct and γ Dor stars, the time-dependence in the pulsation-convection interaction is known as the problem of the red edge of instability strip; see Fig. 1. The convective timescales in the thin outer convection zones of DA and DB white dwarfs are much shorter than those of their g-mode pulsation periods, leading to mode excitation (e.g., Goldreich & Wu, 1999).

The general case where the convective and mode timescales are similar is much more challenging to treat in terms of stochastic mode excitation by the turbulent pressure perturbation. This was developed by Houdek et al. (1999) and Dziembowski et al. (2001). Major improvements in excitation theory were achieved for low-mass stars across stellar evolution by Belkacem et al. (2008), Dupret et al. (2009), Belkacem et al. (2012, 2011), and Grosjean et al. (2014); Houdek & Dupret (2015) provided a good summary. Despite this progress, considerable uncertainty in the predictions for mode excitation and damping properties, as well as for the amplitudes, remain due to uncertainties in the equilibrium structure of the superadiabatic outer envelope and its coupling to the atmosphere. Convection and nonadiabaticity also affect the oscillation frequencies, and despite major efforts and progress on this front for the Sun (e.g., Houdek et al., 2017), current theoretically predicted frequency values are not yet at a level such that they can be fitted to the observed frequencies. This is known as the problem of the “surface effects” in asteroseismology of stars with solarlike oscillations.

A rough global summary of the observed mode periods and amplitudes in pulsators excited by heat mechanisms and stochastic driving for the classes indicated in Fig. 1 is provided in Table A.1 given by Aerts et al. (2010). The periods range from minutes to months. While this is already a broad range, at least three more additional cases of mode excitation are in order.

2. Nonlinear resonant mode excitation

Many of the CoRoT and *Kepler* light curves reveal nonlinear effects. Combination frequencies are omnipresent in the oscillation spectra of κ -driven pulsators along the main sequence, as discussed by Degroote et al. (2009), Pápics (2012), Kurtz et al. (2015), and Bowman et al. (2016). Combination frequencies got lost in ground-based data as they often have amplitudes below ppt. They may be due to nonlinearities in the light curves due to deviations from sinusoidal variations, because the modes have amplitudes beyond the linear regime. However, given the density of g-mode eigenfrequency spectra, combination frequencies may also occur at actual eigenmode frequencies of the star that get excited by nonlinear resonant mode coupling. A distinction between these two cases is not evident when dealing with hundreds of frequencies deduced from a long-duration light curve.

Excitation of nonradial “daughter” modes via nonlinear “parent” mode coupling is expected for particular low-order combination frequencies from theoretical considerations based on the method of amplitude equations, as developed by Buchler & Goupil (1984), Goupil & Buchler (1994), Van Hoolst (1994), and Buchler et al. (1997). This mode excitation may give rise to time-variable mode amplitudes, as commonly observed in space photometry of the higher-amplitude nonradial pulsators. Mainly due to a lack of proper data, theoretical predictions on nonlinear mode excitation remained largely unexploited prior to space asteroseismology, with the notable exception of g modes in white dwarfs. For those, the phenomenon of nonlinear mode coupling was already accessible from ground-based data, thanks to their short pulsation periods. This allowed one to assess the depth of the outer convection zones following Wu (2001) and Montgomery (2005). Meanwhile, nonlinear mode interactions were detected in the short-cadence *Kepler* data in the cool pulsating DA white dwarfs KIC 4552982 (Bell et al., 2015) and PG 1149+057 (Hermes et al., 2015). Both of these DA pulsators revealed large-amplitude regular outbursts with timescales of days, which is much longer than the individual pulsation-mode periods. This nonlinear behavior in pulsating white dwarfs remained unknown prior to space asteroseismology, even though large flux variations up to $\sim 20\%$ recur. Nonlinear asteroseismology was also performed for the DB white-dwarf star KIC 8626021 (Zong et al., 2016a) and for the pulsating subdwarf B star KIC 10139564 (Zong et al., 2016b), where rotation was found to be a key actor in the detected resonances of the latter.

Nonlinear mode coupling behaves in diverse ways as predicted by theory and it is a phenomenon occurring across the entire HRD. Weinberg & Arras (2019) invoked cascades of daughter modes resulting from nonlinear mixed-mode parents as an explanation for the sup-

pression of mixed-mode amplitudes observed in about a quarter of the pulsating red giants. This study was triggered by the suggestion made by Mosser et al. (2017a) that not all suppressed dipole modes found in red-giant pulsators with this phenomenon can be explained by the magnetic greenhouse effect originally proposed by Stello et al. (2016). Indeed, some of the stochastic dipole modes with depressed amplitudes are mixed modes with a g-mode character in the stellar interior rather than p modes, as assumed in theoretical developments by Fuller et al. (2015) and Cantiello et al. (2016). Although progress in interpretations based on a strong internal magnetic field was achieved by (Loi & Papaloizou, 2020), Loi (2020), and Bugnet et al. (2021), the interpretation by Weinberg & Arras (2019) does not require core magnetism. This nonlinear theory is an alternative and complementary explanation, which is in line with *Kepler* data of intermediate-mass dwarfs revealing g modes (SPB and γ Dor stars in Fig. 1). Their period-spacing patterns would be affected by a strong magnetic field, following the theory by Prat et al. (2019) and Prat et al. (2020) and accompanying predictions by Van Beeck et al. (2020). To date there has been no observational evidence of internal magnetic fields from observed g-mode period spacings of intermediate-mass stars revealed by Van Reeth et al. (2015), Pápics et al. (2017), Li et al. (2019b), Li et al. (2019c), and Li et al. (2020).

This brings us to nonlinear nonradial asteroseismology for κ -driven main-sequence stars from *Kepler* data. This underdeveloped research field within asteroseismology holds great potential, but the theory is still to be refined up to the level of the *Kepler* data. Unraveling nonlinear effects in the light curves from nonlinear mode coupling via resonant excitation is possible in principle for modes with an infinite lifetime, as the two lead to distinguishable properties. A distinction between the two cases can be made via the phase behavior of the combination frequencies of parent and daughter modes. One expects phase locking to take place whenever low-order combination frequencies occur exactly at another eigenfrequency of the star, such that the latter gets excited by energy exchange between the two or more parent and daughter modes involved in the resonance. Such phase locking was observed in the CoRoT data of the large-amplitude β Cep star HD 180642 (Degroote et al., 2009). Energy exchange due to resonantly coupled nonradial g modes was invoked as the cause of outbursts in pulsating Be stars, a phenomenon first observed in a Be star by the CoRoT satellite (Huat et al., 2009) and later for several Be pulsators with the BRITE constellation (e.g., Baade et al., 2018). Detailed mode coupling studies are currently being undertaken from *Kepler* long-cadence data of p- and g-mode pulsators along the main sequence (e.g., Saio et al., 2018a, for a γ Dor pulsator). Given the observed amplitude and frequency modulations in numerous δ Sct and γ Dor stars (Bowman, 2017), the prospects

for data-driven nonlinear asteroseismology to be put into practice are excellent. Even if mode excitation by nonlinear resonances is not completely understood, one can take the pragmatic approach of exploiting the detected combination frequencies involved in resonance locking and, once identified, test to see whether adding them to the list of identified pulsation modes used for asteroseismic inferences improves in terms of precision of the inferred internal physics. A good target to test this is the *Kepler* eclipsing binary KIC 3230227 (Guo, 2020).

3. Convectively driven internal gravity waves

Traveling damped IGWs can be generated at the interfaces between convective and radiative zones by turbulent convective flux forcing, as studied for the Sun by (Rogers & Glatzmaier, 2005) and for solar-type stars by Dintrans et al. (2005). The pioneering study by Charbonnel & Talon (2005) showed that inward traveling IGWs in low-mass stars result in retrograde waves with the capacity to impose near-rigid rotation on timescales much shorter than the evolutionary timescale. For intermediate- and high-mass stars, IGWs travel outward from the convective core with a similar capacity (Rogers et al., 2013), which explains observed asteroseismic rotation properties (Rogers, 2015).

Although the 3D simulations of solarlike stars by Alvan et al. (2014, 2015) and of intermediate-mass stars by Edelmann et al. (2019) and Horst et al. (2020) showed clear modal structure of internal g modes, it remains unclear if and which of the internal waves become resonant modes. This depends on the profile of the wave's eigenfunction, on its propagation and dissipation properties, on the efficiency of the radiative damping, and on the onset of nonlinearity (e.g., Ratnasingam et al., 2019). A snapshot of the temperature variations accompanying the driving of IGWs and their propagation from the 3D hydrodynamical simulations by Edelmann et al. (2019) is shown in Fig. 14. This gives the reader a grasp of the large-scale fluctuations induced in the stellar interior. The theoretical predictions coupled to the setup of the 3D hydrodynamical simulations is subject of intense debate among various research teams, because it is hard to drive IGWs from convective flows by heating. For this reason, most numerical simulations adopt artificial luminosity boosting in the convective region to get the flows going into the radiative region at velocities compliant with mlt. The dependence of IGW behavior on the level of boosting remains to be studied in detail. The fully compressible 2D simulations by Horst et al. (2020) have lower numerical viscosity and a factor of 1000 lower luminosity boosting than the 3D simulations by Edelmann et al. (2019), yet lead to similar results in terms of IGW properties. Moreover, these simulations lead to appropriate predictions for p modes and for SLF variability

in agreement with space observations of high-mass stars (Bowman et al., 2019a,b, 2020).

The overall spectra of IGWs can be triggered by convective cores, convective envelopes or thin convection zones due to shell burning or opacity bumps in radiative envelopes. These various cases of IGWs generation were extensively discussed by Rogers et al. (2013), Talon & Charbonnel (2008), Fuller et al. (2014), and Cantiello et al. (2009), respectively. Because of an inability to predict which of the waves within the entire generated spectrum of IGWs could get excited as resonant g modes with observable amplitude, we are still far from pinpointing their λ_{lms} values from SLF detected in space photometry, as shown in the right panels of Fig. 4. Just as with the observed g modes, convectively triggered waves will occur mostly in the gravitoinertial regime for the majority of main-sequence intermediate- and high-mass stars, because these waves have spin parameters $s > 1$ for the measured rotation rates of such stars. In view of this, theoretical and numerical studies should consider the driving, propagation, and dissipation of stochastic gravitoinertial waves (GIWs) in rotating stars (Augustson et al., 2020), rather than IGWs in nonrotating stars. Synergies between GIWs predicted from 3D simulations and nonradial nonadiabatic oscillation modes computed in the TAR from 1D stellar equilibrium models are yet to be explored, starting with the observational constraints on the detected frequency regimes, in the spirit of Fig. 1 given by Aerts et al. (2019). In that way, one may develop asteroseismology based on the observed spectra of the GIWs. Neiner et al. (2020) offer a step in this direction with their application of GIW asteroseismology to the rapidly rotating pulsating Be star HD 49330 observed by CoRoT.

4. Tidal excitation of nonradial modes

The tidal action of a companion in a close binary is yet another way to excite nonradial oscillation modes. This was realized by Cowling (1941) when he introduced “his” Cowling approximation. Tidally excited nonradial oscillations and their effect on stellar evolution have been studied extensively in the literature from a theoretical viewpoint, for various types of close binaries; see Zahn (1975), Papaloizou & Savonije (1997), Savonije & Papaloizou (1997), Terquem et al. (1998), Witte & Savonije (1999), Willems (2003), and Fuller & Lai (2011) for studies across the stellar mass range prior to the *Kepler* mission. Fuller (2017) covered the case of eccentric binaries discovered from space photometry. For this excitation mechanism to work, the properties of the nonradial eigenmodes must be “suitable” compared to the period and the eccentricity of the binary orbit. The component masses and radii must also be in the proper regime to trigger nonradial modes by the tidal forces. The tide-

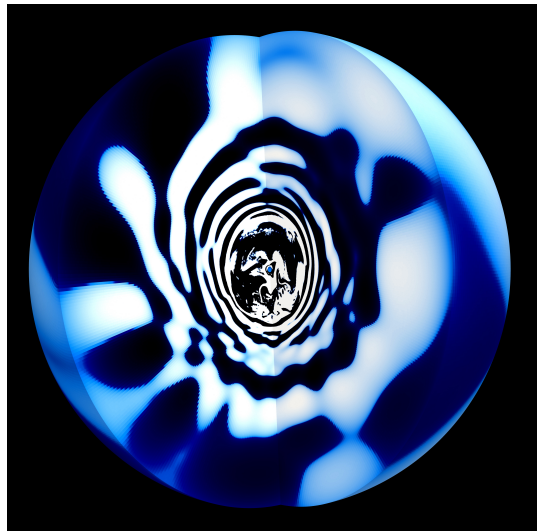


FIG. 14 Snapshot of 3D hydrodynamical simulations representing the temperature fluctuations induced by IGWs excited by stochastic forcing at the transition layer between the convective core and the bottom of the radiative envelope of a $3 M_{\odot}$ ZAMS star. The color coding represents fluctuations up to 10^5 K with respect to an equilibrium model. Figure based on data in Edelmann et al. (2019) by courtesy of Philipp Edelmann, Newcastle University.

generating potential within an eccentric binary is related to an infinite number of partial dynamic tides with forcing frequencies and it is dominated by spherical harmonics of degree $l = 2$. Whenever one of those forcing frequencies gets into resonance with an eigenfrequency of a free oscillation mode of one of the components, the tidal action exerted by the companion may excite this mode.

Tidally excited oscillations are expected to occur at exact multiples of the orbital frequency. This makes them easy to spot in the Fourier transforms of the light curves, particularly when they occur in eclipsing binaries for which the orbital period is directly accessible from the space photometry. The occurrence of resonances between partial dynamic tides and free oscillation modes is particularly relevant for the excitation of g modes, because of their similarity in period compared to orbital periods of close binaries. Just as for the g modes in single stars, CoRoT already allowed us to discover tidally excited modes in binaries, but the 4-yr-long time base of the *Kepler* mission implied the true beginnings of tidal asteroseismology. Numerous cases have meanwhile been discovered and analyzed, the most spectacular one shown in Fig. 15 (another one is discussed in Sec. IV.F and is shown in Fig. 19). The stunning light curve of KIC 8112039, also known as Kepler-Object-of-Interest number 54 (KOI-54, Welsh et al., 2011) shown in Fig. 15 was the first object of a new class of high-eccentricity pulsating binaries whose *Kepler* light curve resembles the signal of a human heartbeat measured in a cardiogram, hence this class

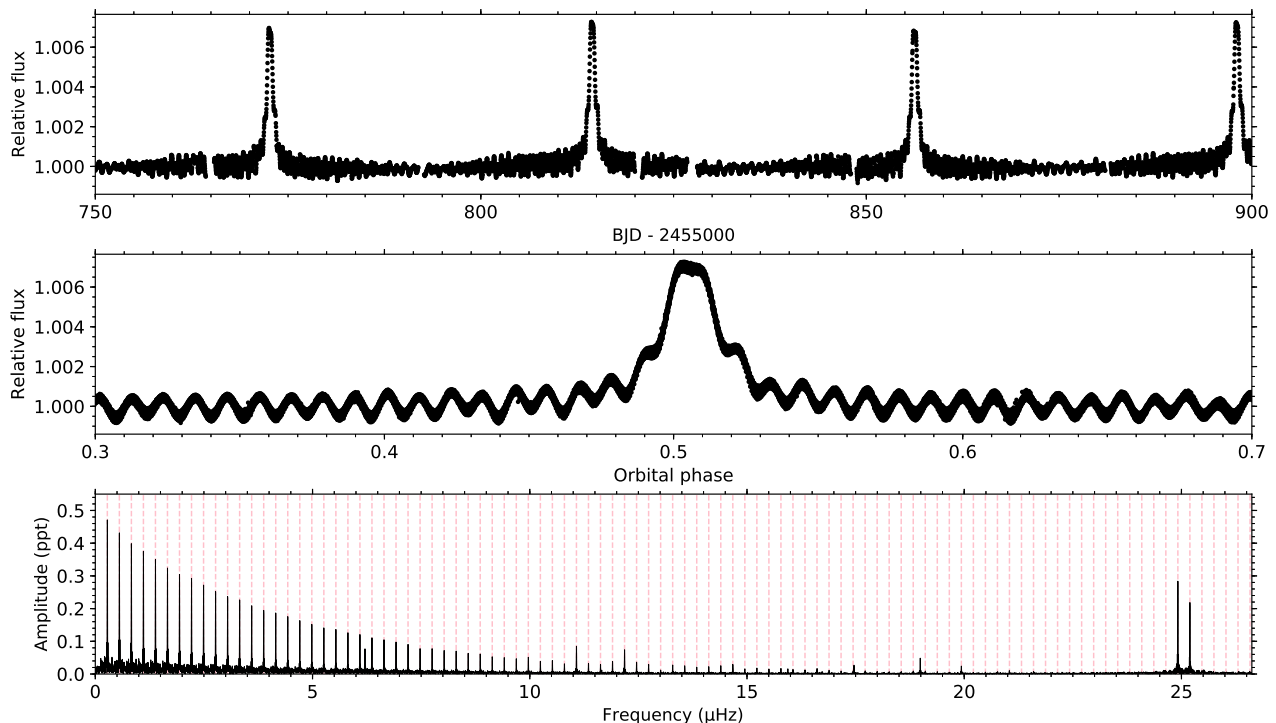


FIG. 15 Excerpt of the *Kepler* light curve (top panel), phase folded according to the orbital frequency (middle panel), and LS amplitude spectrum (bottom panel) of the eccentric eclipsing binary KIC 8112039. All but two frequencies (not indicated by a thin red vertical line) in the bottom panel are caused by tidal excitation. Figure based on data in Welsh et al. (2011) by courtesy of Timothy Van Reeth, KU Leuven.

was named “heartbeat stars” by Thompson et al. (2012). However, we prefer a naming based on the physical properties, and hence refer to the class as high-eccentric binaries. KOI-54 has more than 100 tidally excited g modes, indicated by the red vertical lines in Fig. 15. Those with dominant amplitude occur at 90 and 91 times the orbital frequency and are interpreted in terms of prograde sectoral quadrupole modes excited by dynamical tides in a system where the rotation axis of the primary star is almost aligned with the orbital axis. These two dominant modes are locked in resonance with the orbit. Such an interpretation leads to the other g modes being near-resonant quadrupole zonal modes, while the two modes whose frequency is not a multiple of the orbital frequency are due to three-mode nonlinear mode coupling (Fuller & Lai, 2012). With the discovery of numerous close binaries revealing multiple oscillation modes, tides are an important excitation mechanism for nonradial modes in binaries, while they also affect free oscillation modes that would occur if the star were single (e.g., Guo et al., 2020). The interpretation of tidally excited or tidally affected nonradial modes is a tedious job, because the tidal forces imply deformations of the mode cavities relative to the cavities for single stars (cf. Fig. 8). This bare fact has yet to be exploited in detail.

The opposite situation of having fewer modes than expected also occurs and may be connected to binarity. Evidence for suppression or even absence of solarlike oscillations in low-mass stars with convective envelopes by stellar companions was found (e.g. Derekas et al., 2011; Gaulme et al., 2016; Schonhut-Stasik et al., 2020). Systematic large-scale observational studies with spectroscopy, interferometry, or adaptive optics are required to deduce the cause(s) of the absence of expected oscillations in (unknown spectroscopic) binaries, e.g., to discriminate between tidal changes of the mode cavities versus dilution of oscillation amplitudes due to contaminating flux from visual companions. Evidence for damping of solarlike oscillations or amplitude suppression due to magnetic activity has also piled up for both single and binary low-mass stars (Mathur et al., 2019).

As a general conclusion, one cannot rely on current theory to deliver a complete list of unstable mode frequencies $\omega_{nlm}^{\text{theo}}$ to be compared with the observed ones to identify the mode wave numbers belonging to each detected frequency. We observe more eigenmodes than predicted by the current nonadiabatic nonradial oscillation theory, particularly in the g-mode regime. This observational fact points to current limitations in nonadiabatic mode excitation and damping computations, due to miss-

ing opacity, to overinterpretation of radiative damping, or to yet other unknown physical phenomena in the outer envelopes of stars. It is therefore premature to rely on nonadiabatic predictions of mode excitation when performing asteroseismic modeling. Instead, the mode excitation predictions should be used as a good but not perfect guideline of the modes to be expected from the current knowledge of input physics in equilibrium models while being aware that modes predicted not to be excited do occur in real stars and the other way around. Once the best stellar model has been found from adiabatic asteroseismic modeling, one can check its nonadiabatic mode excitation and damping predictions and use those modes that are predicted to be stable yet observed as an excellent guide to improve the input physics of the models and the excitation theory.

B. Mode identification

Inferences on stellar interiors from asteroseismology provide tighter constraints the more oscillation modes are involved in the modeling. For this reason, asteroseismic modeling takes a pragmatic data-driven approach: we thankfully use all detected frequencies offered by the stars to work with as long as we can label their wave numbers (l, m, n) or (k, m, n) from adiabatic eigenfrequency predictions. When uncertainty in the labeling occurs, the frequency can still be used but the best equilibrium model selection should be done in a Bayesian way, encapsulating the uncertain mode identification in the prior(s). Thanks to space photometry, identification of (l, m) can often be achieved from pattern recognition, notably when rotational multiplets as in Eq. (44) are detected. We now highlight a few of the current methods to deduce the mode identification. These depend on the kind of pulsator and type of mode(s).

It is noteworthy that asteroseismic modeling to estimate stellar properties other than rotation is usually done from axisymmetric ($m = 0$) modes. These tend to be available in low-mass stars with stochastically-excited modes. Such modes are often not detected in the case for p-, g-, or r-modes in heat-driven pulsators. Moderate to fast rotators tend to reveal mostly prograde or retrograde modes with $m \neq 0$ in the data. For such cases, identification of m is also needed, aside from labeling n and l (or k in the case of Rossby modes).

1. Mode identification from échelle diagrams

For low-mass stars with stochastically-excited modes, as those shown in Fig. 10, one uses so-called échelle diagrams to identify the l - and n -values of the modes. An échelle diagram is a plot of the detected mode frequencies as a function of the frequencies modulo the large

frequency separation as given in Eqs. (38) and (39) and readily accessible from the PD as illustrated in Fig. 10. In practice, an observed PD spectrum is cut into segments of length $\Delta\nu$ and these segments are subsequently stacked on top of each other to make a 2D map of ν vs $\nu/\text{mod}(\Delta\nu)$. When doing that, modes of the same degree l “line up” along quasivertical ridges. This was found to be a convenient way to represent and identify the solar oscillation frequencies by Grec et al. (1980), who introduced the terminology of échelle (French for “ladder”) diagram. Échelle diagrams are commonly used ever since to identify l and n in low-mass pulsators with stochastically excited modes (we refer to Fig. 2 given by Chaplin & Miglio, 2013, for colorful examples from *Kepler* data) and recently also for p modes of young δ Sct stars (Bedding et al., 2020).

A computationally convenient way to identify modes after derivation of the large and small frequency separation in the case of noisy data was developed by Roxburgh & Vorontsov (2006). This method relies on the autocorrelation function (ACF) and allows one to deduce the diagnostics $\Delta\nu$ and $\delta\nu$ without being capable to derive the individual mode frequencies. The ACF is defined as the Fourier spectrum of a filtered Fourier transform of the time series, where the choice of the filter function can be optimized according to the envelope of the observed signal in the PD spectrum as shown in Fig. 10. Mosser & Appourchaux (2009) provided a formal definition of the ACF and additional details. The ACF method to derive the large and small frequency separations as a way to achieve the mode identification is efficient, relies on the physical properties of the wave behavior in the mode cavities, and allows one to suppress disturbing effects of the noise in the PD spectrum. This is why the ACF is currently being used in frequency analysis pipelines, although échelle diagrams remain visually attractive and insightful.

Any departure from the asymptotic relation given by Eq. (38), such as considering the lowest frequency regime of p modes, will introduce curvature in the échelle diagrams. This curvature is also found as the star evolves and mixed modes occur, creating “bumps” in the échelle diagram. These phenomena are effectively illustrated in Fig. 13 given by García & Ballot (2019). For an enlightening discussion of a doubtful identification for the CoRoT F-type pulsator HD 49333 due to mode bumping, and how to treat this “doubt” in the context of a Bayesian prior, see Appourchaux (2014).

2. Mode identification from rotationally split multiplets

Rotational splitting following Eq. (44) gives rise to multiplet structures in the data: $l = 1$ triplets, $l = 2$ quintuplets, etc. This has long been known from ground-based data of self-excited modes and is also observed from

space photometry, e.g. Kurtz et al. (2014), Pápics et al. (2014), and Reed et al. (2014). The detection of complete multiplets with an odd $(2l + 1)$ number of components as in these examples immediately reveals the l and m values of the modes from the Fourier transform of the data. Rotational splitting also gives information on $\Omega(r)$, as discussed by Aerts et al. (2019), which includes illustrations based on *Kepler* data.

3. Mode identification from period-spacing patterns

Period spacings ΔP for low-degree zonal gravito-inertial modes of main-sequence F-type stars typically range from 2000 to 4000 s for dipole modes and from 1000 to 2500 s for quadrupole modes. These ranges are obtained when varying the mass (from 1.3 to 2.0 M_{\odot}), age, metallicity, and mixing properties of models in appropriate regimes according to the observed mode frequencies (Van Reeth et al., 2016). Main-sequence B-type g-mode pulsators, on the other hand, reveal a much broader range covering roughly $\Delta P \in [1000, 15000]$ s (Pápics et al., 2017; Szewczuk & Daszyńska-Daszkiewicz, 2017). These stars have masses between 3 and 10 M_{\odot} .

Gravity-mode period-spacing patterns such as those shown in Figs. 11, 12, and 13 immediately reveal the sign of m . Indeed, prograde modes have a $(P, \Delta P)$ pattern with a downward trend (Fig. 11), while the pattern of retrograde modes reveal an upward trend (Figs. 12 and 13). The slope of these patterns allows estimation of the rotation frequency in the region where the g-mode kernels $K_{nl}(r)$ are dominant. As shown in Fig. 9, the kernels of high-order g modes are sharply peaked near the convective core. Hence, observed gravito-inertial g modes, Rossby modes, and Yanai modes allow Ω_{core} to be assessed from the slope of the period spacing patterns by exploiting the relationship between the observed series of λ_{lms} and Π_0 , l (or k for Rossby or Yanai modes), and m . Indeed, λ_{lms} depends on the spin parameter and the value of the asymptotic period spacing, as revealed by Eq. (49). Slightly different methods to identify the mode numbers l (or k) and m , along with estimation of Ω_{core} , were developed by Van Reeth et al. (2016) based on model grids with varying M , Z , X_{ini} , and D_{ov} and by Ouazzani et al. (2017) and Christophe et al. (2018) based on stretching the ΔP patterns to obtain Π_0 . This stretching is done by searching the value of λ such that $\sqrt{\lambda} P_{lms}^{\text{co}}$ are equally spaced by Π_0 . Both methods give excellent agreement on the estimation of Ω_{core} (Ouazzani et al., 2019, Fig. 5). Takata et al. (2020) came up with yet another tool for mode identification. It is based on a diagram in which the frequency is plotted against the square root of the frequency. This allows one to identify prograde sectoral modes and deduce at once the average rotation rate and Π_0 , which is in line with the numerical method by Van Reeth et al. (2016) that delivers mode

identification along with estimation of Ω_{core} and Π_0 .

As discussed earlier, Rossby modes are always retrograde in the inertial reference frame of an observer. These modes occur at similar radial order (n typically between -10 and -80, Li et al., 2020) but have higher spins (Aerts et al., 2017b, values between 15 and 30) than gravito-inertial g modes (n roughly between -10 and -100 and spins between 1 and 15). Saio et al. (2018b) studied the observational appearances of even and odd Rossby modes by computing their visibilities. It was found that the amplitude distributions of odd ($k = -1$) modes are located at lower frequencies than those of even ($k = -2$) modes for any given m and that the amplitudes decrease strongly as m increases; see their Fig. 4. These theoretical predictions offer a good way to identify the wave numbers (k, m) for these modes.

C. Asteroseismic modeling using mode frequencies

1. Some modeling preliminaries

Seeking agreement between the detected identified oscillation mode frequencies $\omega_{nlm}^{\text{obs},i} \pm \sigma_{\omega_{nlm}^{\text{obs},i}}$ and those predicted by equilibrium models $\omega_{nlm}^{\text{theo},i}$ for $i = 1, \dots, N_{\omega}$, with N_{ω} the number of detected identified oscillation frequencies, constitutes a multivariate (nonlinear) regression problem. Fitting these identified frequencies can generally be done with or without the addition of other seismic diagnostics (such as mean frequency separations, frequency ratios, or other combinations for particular modes) or by adding other observables into the fitting process [T_{eff} , $\log g$, $\log(L/L_{\odot})$, an interferometrically deduced R_{\star} , a dynamical binary component mass M_{\star} , etc.]. In general, we consider an observed vector \mathbf{Y}^{obs} consisting of $i = 1, \dots, N_{\omega} + M$ components Y_i^{obs} derived from N_{ω} observed and identified oscillation frequencies and $M \geq 0$ additional observational constraints. Comparison of \mathbf{Y}^{obs} with the corresponding \mathbf{Y}^{theo} predicted by model computations is an extremely powerful method to determine the interior and global properties of stars, including their rotation, mixing, and composition profiles as well as their mass, radius, bulk metallicity, and age. Nonradial oscillations occur in different types of stars in almost all phases of stellar evolution; see Fig. 1. This, along with the availability of long-duration high-precision space photometry, has turned the potential of an asteroseismic calibration of the theory of stellar structure and evolution into a reality. The level of sophistication adopted for asteroseismic modeling is highly variable. Here, we summarize methodology that can handle the challenging case of pulsating stars having a convective core and rotating up to considerable fraction of their critical rate.

In our description of asteroseismic modeling via regression, we follow the notations and concepts given by Aerts

et al. (2018b); i.e., we denote equilibrium models generically as $\mathcal{M}(\boldsymbol{\theta}, \boldsymbol{\psi})$, where $\boldsymbol{\theta}$ stands for the vector containing the free parameters to be estimated for the fixed choices of the input physics $\boldsymbol{\psi}$ (i.e., frozen microscopic and macroscopic input physics). The goal is to fit as closely as possible the observed and identified oscillation frequencies and other observables by theoretical values derived from the 3D perturbation of $\mathcal{M}(\boldsymbol{\theta}, \boldsymbol{\psi})$. We keep in mind the following important aspects:

1. Theoretically predicted oscillation mode frequencies have uncertainties $\sim 0.001 \text{ d}^{-1}$ ($\sim 0.01 \mu\text{Hz}$) due to limitations in our knowledge of physics and due to numerical implementations. The observed oscillation frequencies from space asteroseismology are typically one to several orders of magnitude more precise than the theoretical predictions (see Table 1 in Aerts et al., 2019).
2. The components of \mathbf{Y}^{theo} are strongly correlated.
3. The components of \mathbf{Y}^{theo} and of \mathbf{Y}^{obs} may have very different variances, i.e., heteroscedasticity has to be included in the formalism.
4. The components of $\boldsymbol{\theta}$ may also be strongly correlated.

These four properties result in a challenging modeling problem. Indeed, the theoretical uncertainties stemming from limitations in $\boldsymbol{\psi}$ and from numerical implementation to compute the equilibrium models dominate over the measurement uncertainties. This fact is often ignored in the modeling procedure. Moreover, the correlated nature of the fitting problem implies that the uncertainty regions for the parameters in $\boldsymbol{\theta}$ tend to be of multidimensional elongated shape, and therefore hard to interpret. We provide a mathematical scheme that takes into account these challenges.

The limitations of the equilibrium models are due to restrictions to nonrotating 1D models, missing atomic physics, poor opacities, imperfect numerical schemes to solve the differential equations, etc. Some of the distributions of systematic uncertainties in the theoretical predictions of oscillation frequencies are shown in Figs. 2 to 10 given by Aerts et al. (2018b) for the case of g modes in stars with a convective core. An assessment of some of the systematic biases in the case of solarlike oscillations was provided by Gruberbauer et al. (2013). From the viewpoint of improving stellar structure and evolution theory, the aim is to select the most likely physical model $\mathcal{M}(\boldsymbol{\theta}, \boldsymbol{\psi})$ from an unbiased sample of stars without introducing *a priori* bias by restricting too narrowly the choice of the input physics $\boldsymbol{\psi}$.

The general procedure of asteroseismic modeling of an ensemble of stars is graphically depicted in the flowchart in Fig. 16. We discuss this framework in the rest of this section, but it is not necessary to digest the details of

this flowchart to understand the applications treated in Sec. IV.

2. Setup of the modeling approach

In the stellar modeling problem at hand, the choices of $\boldsymbol{\theta}$ and $\boldsymbol{\psi}$ are different for stars with a radiative versus a convective core. Moreover, the probing power of p- and g modes is different; see Fig. 9. Hence the choice of the parameters in the vector $\boldsymbol{\theta}$ to be estimated and the level of redundancy in the observables to be used also differ; see Angelou et al. (2017) for an enlightening discussion on this topic. While the observed mode frequencies in slowly rotating stars can be condensed into a few “observables” derived from asymptotic approximations as in Eq. (38) or (41), this is not the case for moderate to fast rotators because their patterns depend on the interior rotation and are different for different l and m , as revealed by Eq. (49). Even though a stretching method has been devised to transform the observed period-spacing patterns due to g modes into one observable (Christophe et al., 2018), its value depends strongly on D_{ov} and Z (Mombarg et al., 2019). One can therefore not assume that the frequencies of g modes can be transformed into simple “summary” diagnostics as in the case of solarlike oscillations in slow rotators (where $\Delta\nu$ and ν_{max} play that role). To treat asteroseismic modeling in general terms, including applications to hybrid pulsators with both p and g modes, we consider a formulation for the matching of individual mode properties. We denote it here for the frequencies, but it can be done for any observable (e.g., period spacings).

Asteroseismic modeling of an individual star is done from an observed vector \mathbf{Y}^{obs} , which includes a set of N_{ω} observables based on the observed frequencies $\omega_{nlm}^{\text{obs},i}$, where each mode has its own mode cavity, lifetime, and probing power for the interior physics; see Fig. 9. Moreover, one often chooses to add M nonseismic observables to the modeling, depending on their capacity to assess the models and their correlation with respect to other components already chosen for \mathbf{Y}^{obs} . In setting up the problem to solve, keep in mind that several observables may be measured independently from each other and occur without covariance, while they do not provide extra information about the star. Singular value decomposition (SVD) methods, among them principal component analysis (PCA), are therefore useful techniques to reduce the dimensionality or to plan or not plan follow-up data once asteroseismic information has been deduced. A SVD approach was introduced for helioseismic inversions by Christensen-Dalsgaard & Thompson (1993), while PCA applications for solarlike and g-mode oscillations were done by Angelou et al. (2017) and Mombarg et al. (2019), respectively.

The length of the vector \mathbf{Y}^{obs} is in general star specific

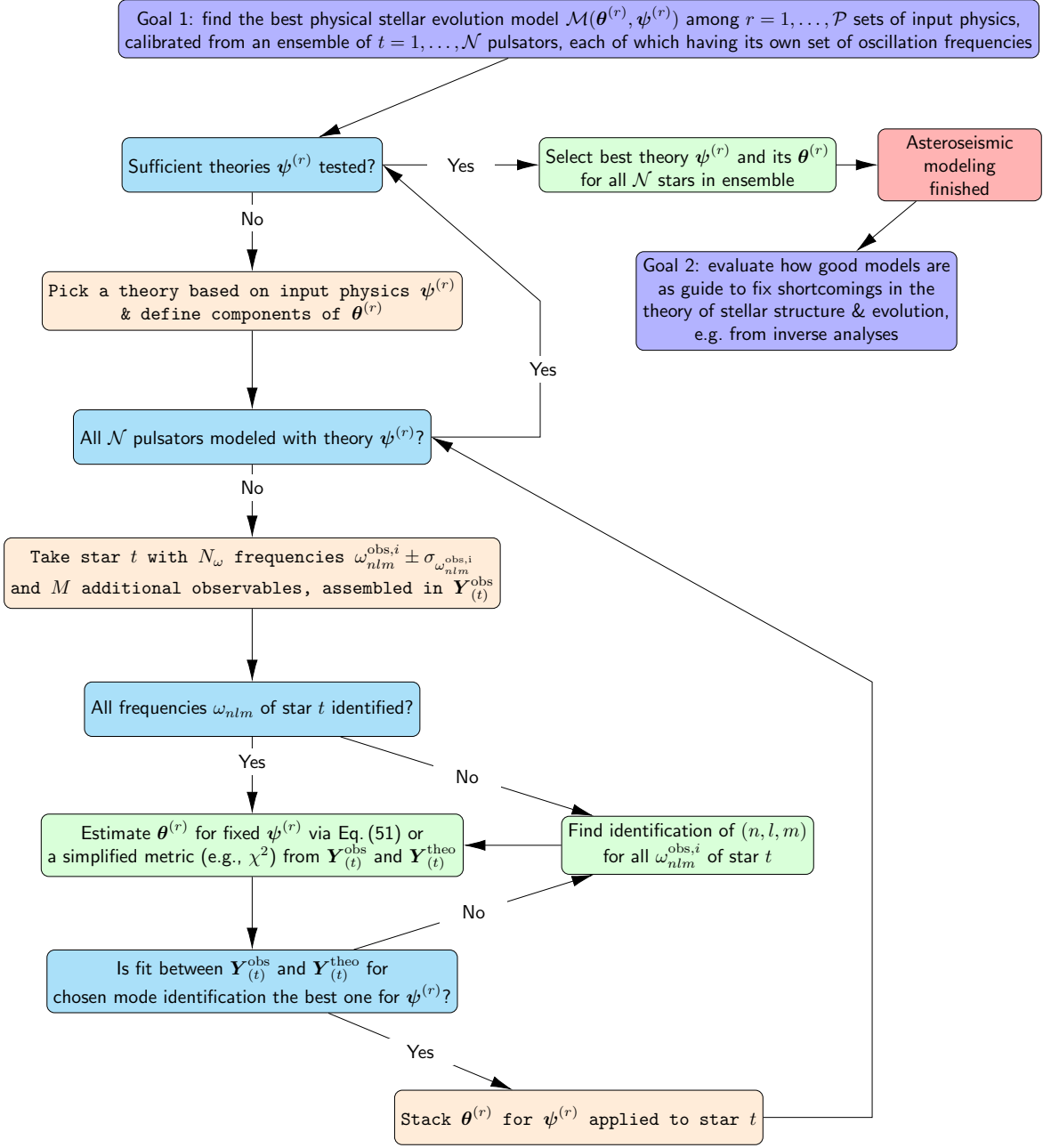


FIG. 16 Schematic representation of the procedure of asteroseismic modeling for an ensemble of stars that summarizes the steps discussed in Sec. III.C. See the text for the meaning of the notation. The green boxes involve statistical methods in the topics of maximum likelihood estimation, pattern recognition, and model selection.

and each of its components is accompanied by its own error measurement ϵ_i^{obs} , for which we assume normality, i.e., $\epsilon_i^{\text{obs}} \sim \mathcal{N}(0, \sigma_i^2)$, as justified by Gruberbauer et al. (2013), Appourchaux (2014), and Aerts et al. (2018b). For each pulsator in an ensemble of stars, the aim is to find the value for θ that best predicts the observables \mathbf{Y}^{obs} , with corresponding value $\mathbf{Y}_0 \equiv \mathbf{Y}_0(\theta_0, \psi)$. We need to select θ_0 such that the distance between \mathbf{Y}^{obs}

and \mathbf{Y}^{theo} is minimal for $\theta = \theta_0$, keeping in mind the correlated nature of the parameters and the observables, as well as any systematic uncertainties in the theoretical predictions. In such a case, a natural merit function to minimize for the estimation of θ is the Mahalanobis distance (Johnson & Wichern, 2007). This merit function represents a generalized distance. It has been introduced in stellar variability classification studies for CoRoT data

(Debosscher et al., 2007). In the current context of asteroseismic modeling, it takes the form

$$\boldsymbol{\theta}_0 = \underset{\boldsymbol{\theta}}{\operatorname{argmin}} \left\{ (\mathbf{Y}(\boldsymbol{\theta}) - \mathbf{Y}^{\text{obs}})^\top (V + \Sigma)^{-1} (\mathbf{Y}(\boldsymbol{\theta}) - \mathbf{Y}^{\text{obs}}) \right\}, \quad (51)$$

where $V = \operatorname{var}(\mathbf{Y})$ is the variance-covariance matrix of the vector $\mathbf{Y}(\boldsymbol{\theta}, \boldsymbol{\psi})$ and Σ is the matrix with diagonal elements σ_i^2 for $i = 1, \dots, N_\omega + M$. The notation X^\top stands for the transpose of X . The matrix V can be estimated so as to capture the variance for each of the components of the theoretically predicted vector \mathbf{Y}^{theo} , keeping in mind that the uncertainties due to the limitations of the input physics $\boldsymbol{\psi}$ are much larger than the measurement errors and that correlations among the vector components occur. The components of \mathbf{Y}^{theo} must cover an appropriate range due to the free parameter ranges of $\boldsymbol{\theta}$. For these reasons, the matrix V can be assessed from grids of models $\mathcal{M}(\boldsymbol{\theta}, \boldsymbol{\psi})$ covering a broad range of $\boldsymbol{\theta}$ for various $\boldsymbol{\psi}$, as illustrated by Aerts et al. (2018a) for the case of g modes. The Mahalanobis distance defined by Eq. (51) provides a more sophisticated merit function than the often used χ^2 based on an Euclidian distance, because it takes into account the variance-covariance structure connected with \mathbf{Y}^{theo} and uncertainties stemming from the limitations of $\boldsymbol{\psi}$. It also considers the overall correlated nature of $\boldsymbol{\theta}$, \mathbf{Y}^{theo} , and their interconnection.

Asteroseismic modeling has thus far mostly been done from minimizing a χ^2 merit function relying only on the measurement uncertainties ϵ_i^{obs} . This was improved upon by Gruberbauer et al. (2012) by taking into account unknown systematic uncertainties of \mathbf{Y}^{theo} in a Bayesian framework, using a χ^2 formulation. The advantage of minimization as in Eq. (51) is that it allows for heteroscedasticity in and correlation structures among the components of \mathbf{Y}^{theo} . Minimizations by Eq. (51) and χ^2 were compared by Aerts et al. (2018b, Table 3 and Fig. 12) for a case of g-mode asteroseismology of a SPB star, leading to a somewhat different best solution for $\boldsymbol{\theta}$. Care must be taken when estimating $\boldsymbol{\theta}_0$ due to the correlated nature of \mathbf{Y}^{theo} and $\boldsymbol{\theta}$, keeping in mind systematic biases in the theory of stellar interiors and ensuring that V is of proper rank.

Estimation of the uncertainty regions for the components of $\boldsymbol{\theta}_0$ is hard to achieve if only one star is modeled, even if many identified frequencies and high-precision classical observables are jointly included in \mathbf{Y}^{obs} . This is due to $\boldsymbol{\theta}$ being of high dimension and containing correlated vector components, as stressed by Angelou et al. (2017) and Aerts et al. (2018b). The multi-D error regions are usually elongated. In such a case, inference on the errors of $\boldsymbol{\theta}_0$ is conveniently achieved from a MCMC approach (see Foreman-Mackey et al., 2013, for a popular tool used in astronomy). For such applications, clever ways to sample are in order to avoid getting stuck in too few local minima in the case of strong covariances (Handberg & Campante, 2011). For this reason, nested sam-

pling in a Bayesian setting is often considered (Corsaro & De Ridder, 2014). A practical MCMC application to asteroseismology of α Cen A was made by Bazot et al. (2012).

3. Considering individual stars and ensembles

A major challenge for low-mass stars with a convective outer envelope is to deal with the 1D treatment of this envelope in the equilibrium models. The outer boundary condition adopted to compute the equilibrium model should come from a proper 3D and time-dependent treatment of convection, while it is usually simplified with time-independent mlt and a 1D atmosphere model. This aspect of asteroseismic modeling for stars with damped modes excited by turbulent convection is known as the problem of the “unknown surface effects.” Clever ways to deal with this, with the attitude of getting rid of the problem, have been developed by using specific combinations of mode frequencies, such as ratios of frequency separations (Roxburgh & Vorontsov, 2003). These ratios were shown to have probing power for the deeper layers of the star while being less sensitive to the physics in the outer layers. In the case of a star with a radiative envelope, the challenge for the modeling is not so much the outer boundary, for which the simple approximation of an Eddington gray atmosphere is fine, but rather how to deal with the near-core boundary mixing and for the high-mass stars also with mass loss due to a radiatively driven and possibly dynamical wind (for $M > 15 M_\odot$).

In the case of solarlike oscillations in low-mass stars, the input physics $\boldsymbol{\psi}$ of the models $\mathcal{M}(\boldsymbol{\theta}, \boldsymbol{\psi})$ is often taken to be similar to that of solar models calibrated from helioseismology. This is fine because one can rely on the reasonable assumption that such stars adhere to similar physics as the Sun, given that they are slow rotators with an extended convective outer envelope. In that case, one can limit the estimation to the minimal set of free parameters to compute the equilibrium models, $\boldsymbol{\theta} = (M_\star, X_{\text{ini}}, Y_{\text{ini}}, \tau)$. More sophisticated applications based on machine-learning techniques treating higher dimensions, e.g., by including α_{mlt} and D_{mix} , are done as well (Bellinger et al., 2016).

For intermediate- and high-mass stars, $\boldsymbol{\theta}$ is always more than four dimensional due to non-negligible interior rotation, core overshooting, and envelope mixing. Even when one can ignore rotation in the computation of the oscillation modes, one deals with a higher-dimensional problem compared to low-mass stars. For pulsators with a convective core, the MLE has to be done minimally with $\boldsymbol{\theta} = (M_\star, X_{\text{ini}}, Z_{\text{ini}}, D_{\text{ov}}, D_{\text{mix}}, \tau)$ in the case where rotation can be ignored (Moravveji et al., 2015). When dealing with gravito-inertial or Rossby modes, i.e., beyond the perturbative treatment of rotation, an estimation of $\Omega(r)$ has to be included in $\boldsymbol{\theta}$, increasing dimensionality

even further (see Moravveji et al., 2016; Van Reeth et al., 2016, for examples).

The multidimensional uncertainty regions of θ_0 are hard to determine for such a complex modeling problem (see Johnston et al., 2019b, for a detailed discussion). It is also challenging to discriminate among candidate theories ψ from the modeling of only one or a few stars. This is why applications optimally consider ensembles of stars. In that case, one has the opportunity to derive the error regions for the individual members or to consider one global average error estimate for each of the components of θ for the entire population. This approach was applied by Silva Aguirre et al. (2017) and Mombarg et al. (2019) to solarlike and γ Dor pulsators, respectively.

As graphically shown in Fig. 16, an important aspect of the ensemble modeling is to assess the quality of a collection of candidate theories, i.e., to consider the following:

- observables $\mathbf{Y}_{(t)}^{\text{obs}}$ for $t = 1, \dots, Q$ members of a representative sample of pulsators, and
- theories $\mathcal{M}(\theta^{(r)}, \psi^{(r)})$, $r = 1, \dots, \mathcal{P}$, each of which delivering predicted values $\mathbf{Y}_{(r)}^{\text{theo}}$.

In such a setting, the goal is to select the most appropriate theory among the \mathcal{P} candidate theories after applying Eq. (51) or a simplified version of it (e.g., χ^2) to every star t . This can be done using a grid-based approach where extensive grids of models $\mathcal{M}(\theta^{(r)}, \psi^{(r)})$ are computed (e.g. Pedersen et al., 2021), or from optimizations “on the fly” via a genetic algorithm approach (Metcalf et al., 2014), or via Bayesian methods coupled to MCMC (Bazot et al., 2012). Akaike or Bayesian information criteria are proper statistical tools to select the best physical model ψ (Claeskens & Hjort, 2008). Care should always be taken to penalize for higher degrees of freedom when doing the model selection, keeping in mind the dimension of θ .

The ultimate goal of ensemble asteroseismology is to have a pathway to improve the input physics of the theoretical models (indicated as second goal in Fig. 16). Hence, once the best of the currently available model sets ψ is chosen according to the first goal in the scheme in Fig. 16, one should evaluate how good or bad it represents the data in the details of each of the individual stars in the sample and for the sample as a whole. Stellar models can subsequently be improved, from inversion methods originally developed in the framework of helioseismology (Gough, 1985a). Such methods are usually applied on a star-by-star basis once the best 1D model for the appropriate θ_0 has been found (see Basu & Chaplin, 2017, for a discussion of the methodology). Initial applications of this technique have led to the interior rotation profiles of six subgiants and young red giants (Deheuvels et al., 2014) and in core-helium-burning red giants (Deheuvels et al., 2015). Detailed analyses resulting in profiles $\Omega(r)$

were obtained for the SPB star KIC 10526294 from g-mode triplets (Triana et al., 2015), the red-giant star KIC 4448777 from dipole mixed modes (Di Mauro et al., 2016), and the differential envelope rotation of 16 Cyg A and B by Bazot et al. (2019). Inversion methods have led to an evaluation of the interior structure for 16 Cyg A and B, revealing discrepancies between the sound speed in the cores of these two stars with respect to those in the 1D models at the level of $\sim 5\%$ (Bellinger et al., 2017), although this binary-exoplanet system is the best calibrated solar analog (Davies et al., 2015). Inversions applied to the exoplanet host star *Kepler*-444 (also known as KOI-3158) resulted in high-precision mass and radius estimates of $M_\star = 0.75 \pm 0.03 M_\odot$, $R_\star = 0.75 \pm 0.01 R_\odot$ and revealed that this star must have had a convective core during the first 8 Gyr of its 11-Gyr lifetime (Buldgen et al., 2019).

IV. APPLICATIONS OF ASTEROSEISMIC MODELING

At least four reviews and a book have recently been published on the topic of asteroseismic applications based on *Kepler* or K2 data. Low- or intermediate-mass stars with an outer convective envelope reveal p modes or mixed modes. The solarlike oscillations of these stars were reviewed by Chaplin & Miglio (2013), Hekker & Christensen-Dalsgaard (2017), García & Ballot (2019), and a book on the data analysis methodology was written by Basu & Chaplin (2017). We revisit some general results based on solarlike oscillations, focusing on what asteroseismology of such stars can deliver to other fields in astrophysics and on opportunities to improve the theory of stellar interiors. The evolution and g modes of white dwarfs were recently reviewed by Córscico et al. (2019), to which we refer for asteroseismic modeling applications to the stellar remnants of low- and intermediate-mass stars. All of these reviews focused on “fast” modes, i.e., high-frequency modes in the sense that their periods are much shorter than the rotation period of the star. In such a case, the Coriolis force can be ignored or treated using a perturbative approach. For this reason, such applications are relatively easy compared to cases where the rotation and oscillation-mode periods are comparable, demanding a nonperturbative treatment.

We start this section with the simplest applications of asteroseismology and gradually increase the level of complexity, putting more emphasis on applications that have been less summarized in reviews thus far. We focus here on “convenience of use” for the nonexpert while highlighting selected striking results and opportunities to improve stellar physics. The topics of Secs. IV.A–IV.F were chosen without any attempt to be exhaustive because that would fill up an entire encyclopedia.

A. Sizing, weighing, and aging stars with convective envelopes

The rotation of stars with $M \lesssim 1.3 M_{\odot}$ slows down efficiently, as first reported by Skumanich (1972) and studied from space photometry (e.g., Meibom et al., 2015). Although the details of their rotational evolution are not yet fully understood (e.g. van Saders et al., 2016), this efficient slowdown is interpreted in terms of magnetic braking induced by the dynamo created in their convective envelope and angular momentum loss via a thin stellar wind. These stars, as well as all evolved stars, have extended convective envelopes that are the seeds of stochastic driving of modes by turbulent convection. Chaplin et al. (2014) provided a summary of the asteroseismic properties of the ensemble of dwarfs and subgiants observed with the *Kepler* spacecraft and found the modes occurring near the frequency of maximum power in the PD spectra to have radial orders ranging from $n = 17$ to 19 for dwarfs and from $n = 15$ to 19 for subgiants. For stars born with a radiative core ($M \lesssim 1.1 M_{\odot}$) and similar metallicity as the Sun, the transition from hydrogen-core to hydrogen-shell burning occurs near $\nu_{\max} \simeq 2000 \mu\text{Hz}$. This transition gradually shifts to lower frequencies for larger and more massive stars. The transition from core to shell burning occurs at $\nu_{\max} \simeq 800 \mu\text{Hz}$ for stars near the upper mass for which solarlike oscillations still occur ($M \simeq 1.5 M_{\odot}$).

Basic key ingredients of asteroseismic applications based on solarlike oscillations are the global seismic scaling relations relying on solar values. These were derived prior to space asteroseismology by Kjeldsen & Bedding (1995). These scaling relations are based on the large frequency separation defined in Eq. (39) and the frequency of maximum power ν_{\max} already discussed in Sec. I:

$$\frac{\Delta\nu}{\Delta\nu_{\odot}} \approx \left(\frac{M}{M_{\odot}}\right)^{1/2} \cdot \left(\frac{R}{R_{\odot}}\right)^{-3/2}, \quad (52)$$

$$\frac{\nu_{\max}}{\nu_{\max,\odot}} \approx \left(\frac{M}{M_{\odot}}\right) \cdot \left(\frac{R}{R_{\odot}}\right)^{-2} \cdot \left(\frac{T_{\text{eff}}}{T_{\text{eff},\odot}}\right)^{-1/2}.$$

In Eqs. 52), the solar reference values have to be computed using the same methodology as for the star(s) under study to achieve meaningful and consistent results. In their Table 1, Pinsonneault et al. (2018) listed solar reference values for various asteroseismic pipelines in use today. It is seen in Eqs. (52) that the large frequency separation scales with the square-root of the mean density of the star. Because one relies on the mass, radius, and oscillations of the Sun for a particular choice of input physics, ψ_{Sun} , one has a quick and easy way to deduce the mass and radius of the star under study. This type of stellar weighing and sizing implies a major simplification: none of the steps in the procedure shown in Fig. 16 have to be taken, because one assumes that the input physics to model the Sun, ψ_{Sun} , is also valid for the star(s) un-

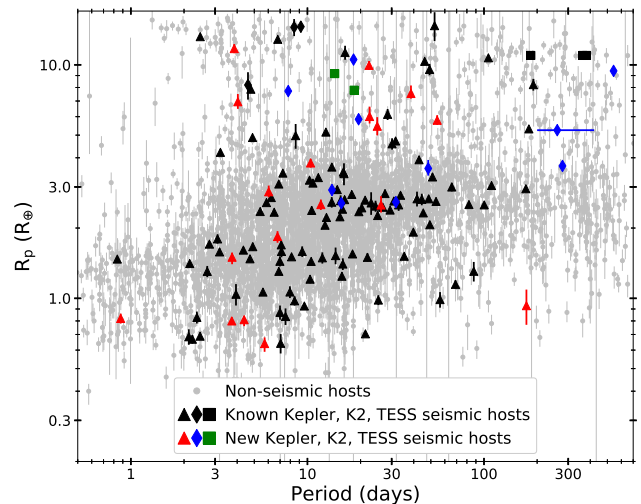


FIG. 17 Planetary radii as a function of orbital period, where the properties of exoplanet host stars with and without asteroseismic estimation are compared. Asteroseismology of the host star not only provides the age of the exoplanetary system but also improves the planetary radii by a factor of ~ 2 compared to the case where such data are not available. Figure based on the sample study by Chontos et al. (2019) and Chontos et al. (in preparation) by courtesy of Ashley Chontos, University of Hawaii.

der study and one does not test any models with other choices for the input physics ψ . This does not allow one to perform model selection among candidate theories ψ , as one freezes the latter to the solar one calibrated from helioseismology. Moreover, by relying on the solar values $\Delta\nu_{\odot}$ and $\nu_{\max,\odot}$ one implicitly assumes that the star under study has the same metallicity and chemical mixture as the Sun. By using the scaling relations in this way, there is no such thing as asteroseismic modeling in the sense of Fig. 16.

For frozen ψ_{Sun} , it follows from the scaling relations in Eq. (52) that a measurement of T_{eff} , $\Delta\nu$, and ν_{\max} suffices to deduce the mass and radius of a star. For such an application, it is not even necessary to know the identification of the individual p modes, as long as one can estimate $\Delta\nu$ and ν_{\max} from the PD spectrum, with or without the help from an ACF. This has major applications, as asteroseismic M_{\star} and R_{\star} values can be computed easily for use in various fields of astrophysics, even from short and/or gapped time series. For this reason, substantial effort has been put into testing the scaling relations from independent methods, notably from an interferometric radius, as done by Huber et al. (2012) and White et al. (2013) or from an astrometric radius, as treated by Silva Aguirre et al. (2012), Huber et al. (2017), and Zinn et al. (2019). Overall agreements are excellent for stars with a fairly large range in radii, from about $0.8 R_{\odot}$ to above $10 R_{\odot}$: this is a tribute to the trio

of asteroseismology, astrometry, and interferometry.

Thanks to their simplicity, the scaling relations in Eq. (52) have been used extensively to deduce the masses and radii of stars with solarlike oscillations observed with space photometry. Aside from the recent *Kepler* catalog papers on dwarfs and subgiants (Chaplin et al., 2014) and red giants (Yu et al., 2018), we refer the interested reader to earlier CoRoT catalogs for red giants by Kallinger et al. (2010) and Mosser et al. (2010, 2012), as well as to the K2 catalog by Stello et al. (2017). The scaling relations were even expanded to the extremely low frequencies of solarlike oscillations in M giants belonging to the class of Semi-Regular Variables; see Fig. 1. This allowed researchers to assess and interpret the period-luminosity relations derived from ground-based microlensing surveys in terms of the interior structure of such highly evolved stars (Mosser et al., 2013). Analyses of M giants observed with *Kepler* led to the discovery of nonradial oscillations of low inertia in such stars, interpreted as f modes by Stello et al. (2014). This discovery holds major potential and has yet to be explored further. In particular, it paves the way to perform extragalactic asteroseismology from observations of M giants in the Magellanic Clouds.

As another key application, masses and radii for exoplanet hosts based on the scaling relations have been published in a number of studies, among them Huber et al. (2013), Van Eylen et al. (2014), Silva Aguirre et al. (2015), Lundkvist et al. (2016), Campante et al. (2016a), and Van Eylen et al. (2018). A radius estimate of an exoplanet host star from the scaling relations propagates directly into a radius estimate of its exoplanets for which a transit has been measured. Asteroseismic sizing from scaling relations is therefore particularly convenient for exoplanet studies. Once an exoplanet has been detected in space photometry, the latter can be revisited in an attempt to measure its host star’s values of $\Delta\nu$ and ν_{\max} (Chontos et al., 2019). Figure 17 shows the planet radii versus orbital periods for an assembly of *Kepler*, K2, and TESS exoplanets, comparing those with and without asteroseismology of the host star. As highlighted in the figure, more measurements of $\Delta\nu$ and ν_{\max} from the PD spectra are achieved as detection methods are refined and spectroscopy (to estimate T_{eff}) are assembled. The gain in precision of the exoplanetary radius is typically a factor of ~ 2 when asteroseismic sizing of the host star from scaling relations can be done relative to the case where no oscillations are detected.

Once the mass and radius of a star have been estimated from the scaling relations, its age and hence its evolutionary stage can be assessed. This requires evolutionary models and was originally done for the Sun. Christensen-Dalsgaard (1988) introduced the so-called CD diagram to estimate the age of solar-type stars from their large and small frequency separations. Chaplin et al. (2014) made a thorough analysis to estimate the ages of the more than 500 dwarfs and subgiants observed with *Ke-*

pler. This ensemble analysis was based on six different data analysis pipelines and 11 stellar model grids in order to assess the combined effect of observational and model uncertainties by taking into account $V + \Sigma$, as discussed after Eq. (51). This is an application of Fig. 16 where one does not use the individual frequencies $\omega_{nlm}^{\text{obs},i} \pm \sigma_{\omega_{nlm}^{\text{obs},i}}$ as input, but rather $\mathbf{Y}^{\text{obs}} = (\nu_{\max}, \Delta\nu, \delta\nu, T_{\text{eff}}, [\text{Fe}/\text{H}])$ to estimate the parameters $\boldsymbol{\theta} = (M, R, \tau)$ and quantities that can be derived from these three (such as the mean density and gravity). For this application, Chaplin et al. assumed that the components of \mathbf{Y}^{theo} are not subject to uncertainties and are not correlated with each other, such that χ^2 can be used as a merit function. Under these assumptions, this ensemble modeling led to average relative precisions of approximately 5.4% in mass, 2.2% in radius, and $\sim 10\% - 20\%$ in age. Such relative precisions are within reach when spectroscopic estimates of T_{eff} and $[\text{Fe}/\text{H}]$ are available. If only ν_{\max} and $\Delta\nu$ are available, the relative precisions are downgraded by about a factor of 2, which is still excellent and often the only way to get an age estimate of isolated stars in the Milky Way.

Bellinger (2019, 2020) derived scaling relations for the ages of dwarfs, subgiants and red giants from $\mathbf{Y}^{\text{obs}} = (\nu_{\max}, \Delta\nu, \delta\nu, T_{\text{eff}}, [\text{Fe}/\text{H}])$. For the dwarfs, the relations were deduced from fits to these quantities for 80 stars whose measurement uncertainties for $\delta\nu$ and ν_{\max} are better than 10% and 5%, respectively. This leads to age precision estimates of about 10% for dwarfs. These formulas are easy to use (e.g., for exoplanet host aging), but users have to keep in mind that the relations explicitly rely on the solar input physics via homology relations. Thus, the fact that the interior rotation, mixing, and magnetism of the stars might be different than those of the Sun is ignored.

A major breakthrough in asteroseismology was achieved upon the detection of mixed dipole modes in *Kepler* data of evolved low-mass stars (Beck et al., 2011; Bedding et al., 2011) after they had been theoretically predicted in the context of CoRoT by Dupret et al. (2009). The mixed modes can have a gravity-dominated or a pressure-dominated character, depending on the extent and shape of their propagation cavity. Such dipole mixed modes in evolved stars occur together with radial and quadrupole p modes, which obey the asymptotic relation in Eq. (39) and probe the convective envelope of the star. Measurement of $\Delta\nu_{nl}$ and ΔP_{nl} thus allows one to derive the mass and radius of the star from scaling relations, as well as its evolutionary stage (Bedding et al., 2011). Indeed, the gravity-dominated mixed modes probe the deep stellar interior and have different values for hydrogen-shell-burning red giants than for core-helium-burning red giants. This allows to deduce the nuclear burning stage of these two types of red giants, while their surface properties are the same. Period spacings

of dipole mixed modes lead to higher-precision age estimates than the large frequency separation from p modes. Moreover, the period spacings are a sensitive probe for internal mixing in intermediate-mass dwarfs and allow one to calibrate the core overshooting efficiency using low-luminosity red-giant stars (Hjørringgaard et al., 2017). We return to this capacity for g modes in Sec. IV.E.

Estimation of R_* from asteroseismology combined with a spectroscopic measurement of T_{eff} allows one to deduce the luminosity of the star and hence derive an asteroseismic parallax (Silva Aguirre et al., 2012). Comparisons between such asteroseismic parallax with the one from Gaia astrometry reveals excellent agreement for dwarfs (e.g., De Ridder et al., 2016) and red giants (e.g. Huber et al., 2017). This allows one to probe the deep end of the Milky Way with luminous pulsating stars (Mathur et al., 2016). The capacity of joint asteroseismic aging, sizing, and distance estimation opened up the field of galactic archaeology, which had already been jump-started prior to the Gaia era by Miglio et al. (2009). Their study of various populations of core-helium-burning red giants in the galactic disk observed with CoRoT opened a new field of mapping and dating stellar populations from red-giant asteroseismology (Miglio et al., 2013). Meanwhile, extensive progress has been made in archaeological studies for the pointing directions in the Milky Way covered by CoRoT, *Kepler*, and K2 coupled with large spectroscopic surveys and/or Gaia data; see Stello et al. (2015, 2017), Anders et al. (2017a,b), Serenelli et al. (2017), Pinsonneault et al. (2018), Silva Aguirre et al. (2018), Sahlholdt & Silva Aguirre (2018), Rendle et al. (2019), Zinn et al. (2019), and Sharma et al. (2019). Major potential for extending this topic toward all-sky coverage is being offered by the ongoing TESS mission (Ricker et al., 2016) and the future PLATO mission (Rauer et al., 2014). These surveys should optimally be coupled with spectroscopic surveys with multiobject spectrographs to target hundreds of thousands of asteroseismically aged and sized red giants. The beginnings of such large-scale asteroseismic archaeology have already revealed abundances and distances that allowed one to separate high- and low- $[\alpha/\text{Fe}]$ populations in the Milky Way disk (Chiappini et al., 2015). In this way, asteroseismology has become a key ingredient in the study of the multiple populations and of the chemical evolution of our Milky Way.

To circumvent computationally intensive age derivation from evolutionary models, age scaling relations were derived by Bellinger (2020). These rely on the asteroseismic properties of ~ 1000 red giants and are convenient for galactic archaeologists. These age relations assume that stars adhere to ψ_{Sun} . Their quoted precision of $\sim 15\%$ does not take into account systematic uncertainty due to the unknown evolutionary properties on the main sequence. As highlighted by Fig. 7, uncalibrated descriptions of internal mixing in dwarfs with a convective core are used in the models. Moreover, asteroseismology re-

vealed the theory of angular momentum transport to be limited (Aerts et al., 2019); see also Fig. 6. As long as users of “recipe-type” aging recognize this major culprit stemming from fixing the input physics, the scaling relations are a convenient tool for initial asteroseismic and comparative stellar aging of populations, preventing us from having to go through *à la carte* modeling, a term introduced by Lebreton & Goupil (2014) and Lebreton et al. (2014) that is represented by Fig. 16. To get the maximum precision out of the data of a particular star, including aging to better than 10%, detailed modeling according to Fig. 16 is in order. Treating populations of \mathcal{N} stars in this way is much more cumbersome than applying age scaling relations, but it is the only way to properly take into account the fact that the internal mixing of stars can be diverse (see Fig. 7), even for a population of stars born with the same metallicity and similar rotation; see Table I.

B. Assessing sharp features in stellar structure

Fitting the frequencies or periods of oscillations for individual stars and particularly for an ensemble of stars allows one to learn more about the quality of the input physics ψ of stellar models following Fig. 16. This can be done from fitting (some of) the individual detected and identified oscillation frequencies and periods, rather than simply using the measured averages of global patterns based on the asymptotic theory as in Eqs. (38) and (39) or Eqs. (41) and (42). An intermediate step between the exploitation of only the average value of the frequency or period spacing and the full-blown fitting of all measured individual oscillation modes is offered by modeling deviations from the expected constant spacings due to so-called structural glitches. Sharp features in the sound speed are called acoustic glitches while those in the Brunt-Väisälä frequency are termed buoyancy glitches. These glitches may lead to oscillatory deviations in the patterns of p-mode frequencies or g-mode periods. Interpretation of such measured deviations goes beyond the simple use of scaling relations and provides a good opportunity to derive detailed properties of stellar structure.

Studies of acoustic glitches in the Sun from helioseismology led to the overshoot properties at the base of the solar convective envelope (Monteiro et al., 1994) and to the capacity to position the second ionization zone of helium (Monteiro & Thompson, 2005). Following those solar studies, the potential of exploiting measured oscillatory deviations due to acoustic glitches was investigated further by Monteiro et al. (2000), Basu et al. (2004), and Houdek & Gough (2007) for Sun-like stars covering a mass range of $M_* \in [0.85, 1.2] M_{\odot}$. This led to methods to infer the size of the convective envelope and to derive properties of the overshoot transition layer at the bottom of the convective envelope (Hekker

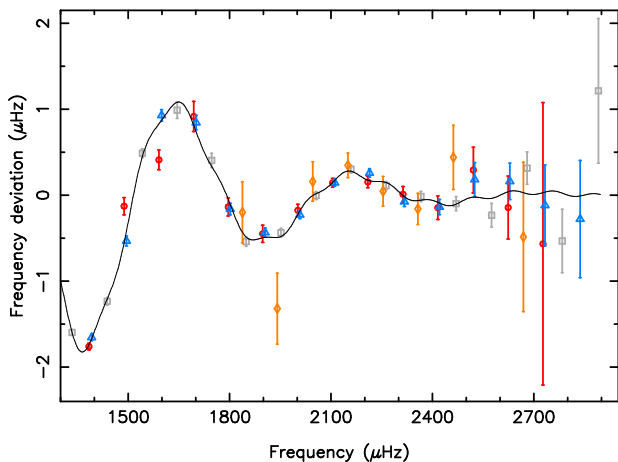


FIG. 18 Frequency deviations with respect to a fourth-order polynomial fit to the measured frequencies for the modes of degree $l = 0$ (blue triangles), $l = 1$ (gray squares), $l = 2$ (red circles), and $l = 3$ (orange diamonds) of 16 Cyg A, based on the PD shown in Fig. 10. The full line represents a fit to the oscillatory signal caused by sharp features in the star’s sound speed in the second ionization zone of helium. Figure produced from data in Verma et al. (2014) kindly made available in electronic format by Kuldeep Verma, Aarhus University.

& Christensen-Dalsgaard, 2017, for an extensive discussion). This methodology was put into practice for *Kepler* data of Sun-like stars by Mazumdar et al. (2014). Figure 18 illustrates the measured oscillatory frequency deviations due to acoustic glitches in the structure of 16 Cyg A, following its PD in Fig. 10. In a series of papers exploiting the measured periodic deviations from constant spacings, Verma et al. (2014, 2017) measured the locations of the base of the convection zone and of the helium ionization zones for Sun-like stars observed by *Kepler*, as well as their helium abundance (Verma et al., 2019) and the level of helium settling due to atomic diffusion (Verma & Silva Aguirre, 2019). In these studies, analytical modeling was compared to numerical asteroseismic modeling following the scheme in Fig. 16 by estimating $\theta = (M_*, Y_{\text{ini}}, [\text{Fe}/\text{H}], \alpha_{\text{MLT}}, \alpha_{\text{ov}})$ for equilibrium models with and without helium settling (i.e., for two different ψ ’s in Fig. 16). The results of such numerical modeling for 16 Cyg A are shown as a solid line in Fig. 18. This led to $Y_{\text{ini}} \in [0.231, 0.251]$, while a similar application to 16 Cyg B revealed $Y_{\text{ini}} \in [0.218, 0.266]$. The differences in helium mass fraction ΔY derived from models with and without helium settling were found to be $\Delta Y \sim 0.038$ for both stars. This result is representative for an additional ~ 30 Sun-like stars analyzed in the same way. As such, frequency deviations due to acoustic glitches offer a unique way to derive the helium composition of stars too cool to reveal helium spectral lines.

For the solar analogs 16 Cyg A and B, even more details on the physics of the envelope could be derived, notably

latitudinal differential rotation due to a dynamo effect. In an updated study based on the same light curve as the one used by Davies et al. (2015), the measured rotational splitting of 16 Cyg A and B led to envelope rotation rates that are higher at the equator than at the pole. Bazot et al. (2019) found the differences of the rotation frequencies between the equator and the pole to be 320 ± 269 nHz and 440 ± 370 nHz for 16 Cyg A and B, respectively, while the equatorial rotation frequencies were 535 ± 75 nHz and 565 ± 140 nHz. This envelope rotation behavior of both binary components is similar to that of the Sun. The results on turbulence and rotation of this solar-analog binary and exoplanet system illustrate how modeling of individual frequencies provides an opportunity to improve the treatment of envelope convection in cool stars.

Mode trapping due to transition zones with compositional changes is omnipresent in stars at evolved stages. This phenomenon has already been detected from ground-based white-dwarf asteroseismology (e.g., Winget et al., 1991, 1994). It was found in large ensembles of *Kepler* γ Dor and SPB stars analyzed by Li et al. (2020) and Pápics et al. (2017), of red giants by Mosser et al. (2015) and of subdwarf B pulsators by Reed et al. (2011), Østensen et al. (2014), Uzundag et al. (2017), and Kern et al. (2018), while it was also confirmed in white dwarfs from K2 photometry (Hermes et al., 2017a). The trapping of g modes or mixed modes was theoretically investigated for red giants by Cunha et al. (2015), for subdwarfs by Charpinet et al. (2000), and much earlier for white dwarfs in the seminal paper by Brassard et al. (1992). Hence, modeling of mode trapping due to structural glitches can now be done across the entire HRD (Cunha et al., 2019b).

During the main-sequence phase, buoyancy glitches occur due to the shrinking convective core of intermediate- and high-mass dwarfs. These glitches lead to deviations from the constant period spacing of high-order g modes for stars with limited chemical mixing in their radiative envelope. Such periodic deviations were first observed in a SPB observed with CoRoT (Degroote et al., 2010a). The signature of buoyancy glitches was also found in the period-spacing patterns of γ Dor stars (Van Reeth et al., 2015), as illustrated in Fig. 11 for one of them (KIC 11721304). A sharp deviation from a period-spacing pattern can also occur when a pure inertial mode in the convective core of a rapid rotator couples resonantly to a heat-driven gravito-inertial mode in the radiative zone (Ouazzani et al., 2020). Such resonances appear at specific mode frequencies. For evolved dwarfs with a shrinking convective core, the signal due to sharp features in the structure of the equilibrium model or due to resonances with inertial modes may be intertwined with mode bumping or avoid crossings (Smeyers & Van Hoolst, 2010, for a mathematical description of these phenomena). A single resonance between a gravito-inertial

mode in the envelope and a pure inertial mode in the core, or a single avoided crossing leads to just one dip in the period-spacing pattern, as observed in Fig. 12. A μ -gradient zone in the near-core region instead gives rise to recurring quasiperiodic deviations. Modeling of such regular deviations provides an excellent opportunity to derive properties of $D_{\text{mix}}(r)$ in the deep stellar interior. Analytical predictions for the oscillatory deviations due to a receding convective core were derived for high-order g modes of nonrotating γ Dor and SPB stars by Miglio et al. (2008). Bouabid et al. (2013) generalized this to a numerical framework for rapidly rotating γ Dor stars. These theoretical studies have been put into practice for dwarfs to estimate their levels of chemical mixing from asteroseismic modeling following Fig. 16, with adopted $D_{\text{mix}}(r)$ profiles as in Fig. 7. We discuss such recent applications in Sec. IV.E.

Moving beyond the main sequence, periodic components in the oscillation frequencies due to sharp features in the convective envelope of the red giant HR 7349 were found in its CoRoT data. The signal is due to a local depression of the sound speed in the second ionization zone of helium (Miglio et al., 2010). Similar studies from *Kepler* observations of red giants were summarized by Hekker & Christensen-Dalsgaard (2017). A powerful analysis to derive the helium abundance for red giants was presented by McKeever et al. (2019) for an ensemble of 27 pulsating red-giant branch (RGB) stars in the metal-rich open cluster NGC 6791 observed by *Kepler*. The helium abundances and ages for each individual cluster RGB star were combined to create a distribution for the cluster’s age and helium abundance, resulting in $Y_{\text{mi}} = 0.297 \pm 0.003$ and $\tau = 8.2 \pm 0.3$ Gyr. Such precision for aging and helium abundance determination is beyond the reach of classical cluster studies involving isochrone fitting (e.g., An et al., 2007), even in the Gaia era (Bossini et al., 2019).

Dipole mixed modes in red giants offer additional opportunities. Structural glitches and mode trapping result in deviations from the asymptotic relations of period spacings of g modes as in Eq. (41), or of gravito-inertial modes as in Eq. (49). Mixed modes comply with a more complex asymptotic spacing pattern due to their mixed g- and p-mode nature. Red giants are slow enough rotators to ignore the Coriolis force for the derivation of their period-spacing expression, of which Eqs. (38) and (41) are the limiting cases for pure pressure and pure gravity modes, respectively. The asymptotic expression for dipole mixed modes depends on the evanescent zone between the g-mode cavity determined by buoyancy as the dominant restoring force and the p-mode cavity where the pressure force is the dominant restoring force. The location, shape, and width of this evanescent zone all play a role in the coupling between these two cavities. The coupling factor, q , reaches extreme values of zero for no coupling and 1 for full coupling. The asymptotic

expression for mixed dipole modes was discussed by Unno et al. (1989). Generalized versions and their use in space asteroseismology were given by Mosser et al. (2014), Takata (2016a), Takata (2016b), and Pinçon et al. (2019). Observational estimations of q from *Kepler* data were made by Buysschaert et al. (2016), Mosser et al. (2017b), Mosser et al. (2018), Jiang et al. (2018), and Hekker et al. (2018). Hekker et al. (2018) used a description that explicitly relies on the radial order of the modes and allows one to constrain the p-mode and g-mode frequency or period offsets observationally. This work revealed the g-mode period offsets to correlate with the core boundary for RGB stars, while the p-mode offsets for core-helium-burning stars require additional mixing in line with the suggestions by Constantino et al. (2015) and Bossini et al. (2017). Hekker et al. (2018) also found that $\ln q$ relates linearly to the width of the evanescent zone normalized by its position. These findings provide observational guidance to tweak $N(r)$ and deduce the core mass of red giants in various evolutionary stages. Pinçon et al. (2019) demonstrated that q is tightly connected with the width of the evanescent zone and showed how this zone changes when stars evolve from the sub-giant to the RGB and further towards the red clump. This study highlighted the capacity of q to probe the dynamics of the zone between the hydrogen-burning shell and the bottom of the convective envelope. To date, this analytical work has focused on stars with masses below $1.2 M_{\odot}$. It needs to be extended to stars born with a well-developed convective core, for one to understand the full structural and evolutionary properties of the evanescent zone for such stars, including those with $M_{\star} \gtrsim 2 M_{\odot}$, which will end up in the secondary clump.

C. Improving the physics of cool-star surface convection

In the case of low-mass stars, one can go beyond the analytical modeling of acoustic glitches, which is in itself an improvement over the use of scaling relations. A major aim of asteroseismology is to let go of the assumption that low-mass stars adhere to ψ_{Sun} . This can be done by comparing the choice of the solar input physics with any other choice of ψ from evaluations between predicted and measured values of the individual oscillation frequencies. Modeling according to Fig. 16 then requires one to “overcome” the surface effects in the case of cool stars with a convective envelope. Indeed, for those stars, the adiabatic approximation of the oscillation frequencies and the use of simplified boundary conditions based on 1D atmosphere models are not good enough relative to reality, as such approaches lead to inappropriate frequency predictions $\omega_{nlm}^{\text{theo},i}$. Relying on equilibrium models with model atmospheres based on mlt to describe the envelope convection rather than taking full account of the turbulent pressure in the superadiabatic near-surface regions leads

to p-mode frequencies that are too high (Christensen-Dalsgaard, 2002). The offset is larger for higher radial orders, i.e., for higher mode frequencies. For the solar oscillations, this leads to offsets for $\Delta\nu_{\odot}$ of the order $10\ \mu\text{Hz}$. Similar offsets are expected to occur for the oscillations of all Sun-like stars with solarlike oscillations. The values of the offsets are much larger than typical uncertainties of the measured oscillation frequencies. The surface effects must hence be assessed to prevent errors in the estimation of θ , even for fixed ψ_{Sun} , when going through Fig. 16.

Methods have been devised to “correct for” or “minimize” the unknown surface effects, guided by their properties regarding the Sun. One way to deal with the surface effects was originally proposed by Roxburgh & Vorontsov (2003), who came up with combinations of p-mode frequencies (the so-called r_{02} and r_{01} indices) that suppress the sensitivity to the outermost layers, decreasing in this way the influence of the limitations of the 1D models in the asteroseismic modeling. More complex indices were subsequently defined with the same aim (e.g. Roxburgh, 2005). Several other methods to fit the surface effects with a statistical model, with the aim of “getting rid” of the differences between the measured and model frequencies, were developed. These adopted various levels of sophistication in the fitting following the pioneering paper by Kjeldsen et al. (2008). Ball & Gizon (2014, 2017), Basu & Kinnane (2018), Compton et al. (2018), and Jørgensen & Weiss (2019) studied this topic.

Even with the simple pragmatic approach by Kjeldsen et al. (2008), the gain between modeling based on the scaling relations versus fitting the actual frequencies is roughly a factor of 2 in the precision of the mass, radius, and age. Such asteroseismic modeling was done for the CoRoT exoplanet host HD 52265 by Lebreton & Goupil (2014), showcasing how aging (and weighing and sizing) of the host star by individual oscillation frequency fitting can be done at the level of 10%. While this study was applied to an individual CoRoT target star according to the principles of Fig. 16, Lund et al. (2017) and Silva Aguirre et al. (2017) applied this full scheme to an ensemble of 66 stars observed in 1-min cadence *Kepler* photometry with a time base of up to 4-yr in the so-called legacy sample of the mission. This study covered the following values for θ : stellar masses between 0.8 and $1.6\ M_{\odot}$, $Y_{\text{ini}} \in [0.2, 0.4]$, $Z_{\text{ini}} \in [0.0025, 0.05]$, $\alpha_{\text{conv}}/\alpha_{\odot} \in [0.5, 1.3]$, and ages between 1 and 12 Gyr. Silva Aguirre et al. (2017) considered seven different choices for the input physics ψ , all of which are nonrotating nonmagnetic 1D models ignoring radiative levitation in the treatment of the microscopic atomic diffusion; see their Table 1. All pulsation computations were done in the adiabatic approximation and ignored the Coriolis and Lorentz forces. The asteroseismic modeling led to average relative uncertainties of 2% in radius, 4% in mass, and 10% in age, and revealed degeneracies between

the stellar mass M_{\star} and initial helium abundance Y_{ini} . All seven adopted ψ led to comparable fit quality when considering calibrations from the Sun, angular diameter measurements, Gaia parallaxes, and binarity. An initiative to assess the differences in stellar models computed with various evolution codes by adopting the same input physics with the aim of evaluating the level of numerical uncertainties and comparing them to asteroseismic uncertainties was provided by Silva Aguirre et al. (2020) and Christensen-Dalsgaard et al. (2020), where the results may be found. Such activities are an important aspect of the model uncertainties at play when one performs modeling via Fig. 16.

Currently, the focus in asteroseismology of low-mass stars adopts a true asteroseismic spirit: rather than shifting the measured frequencies to remove the surface effects, the latter are considered an “observational gift” to improve the weaknesses in the physics of 1D models. This shift in spirit of the asteroseismologists rather than in the measured oscillation frequencies offers great potential. Indeed, the asteroseismic modeling of stars with an outer convective envelope can be further improved by using the measured surface effect as an opportunity rather than a nuisance. A common procedure adopted in 1D models of low-mass stars is to calibrate an interior model and an atmosphere model so as to be consistent with the Sun for one single value of α_{mlt} and do the stitching of the two deep enough in the adiabatic part of the atmosphere. However, this procedure has limitations for evolved stars (e.g., Choi et al., 2018). Asteroseismology of a variety of stars permits one to do better. Indeed, the shift between the measured oscillation frequencies and those predicted by 3D hydrodynamical simulations of convection relevant for the outer envelopes of low-mass stars is informative when evaluating such simulations (e.g., Zhou et al., 2019), assessing nonadiabatic stability analyses (e.g., Houdek et al., 2019), and finding out how to “patch” 3D atmosphere models to 1D models of stellar interiors.

Following initial achievement to match a 3D atmosphere model to a 1D solar interior model by Rosenthal et al. (1999), detailed studies were conducted to achieve optimal patching. The measured surface terms from helioseismology by Magic & Weiss (2016) and from asteroseismology by Sonoi et al. (2015), Ball et al. (2016), and Trampedach et al. (2017) were exploited from the patching of 3D atmosphere models to 1D interior models. This led to improved boundary conditions based on 3D convection simulations. Guidance from measured surface effects and adiabatic predictions of solarlike oscillation frequencies was used to derive the optimal connection depth in the atmosphere. Although this approach does not yet take into account nonadiabatic effects, it offers good potential to come to a better treatment of the 3D simulations of envelope convection and their use for stellar evolution computations. Jørgensen

et al. (2018), Jørgensen et al. (2019), Jørgensen & Weiss (2019), and Mosumgaard et al. (2020) presented detailed procedures to include the mean structure of 3D hydrodynamical simulations as the boundary condition of 1D models to improve their outer stratification. In these studies of patched models, an appropriately calibrated solar model with a structure similar to the underlying 3D simulations is achieved from helioseismology. Houdek et al. (2017) included a full treatment of the interaction between convection and the oscillations.

The measured oscillation frequencies of *Kepler* targets across stellar evolution are now being used to investigate how the convection-oscillation interaction and the transition between envelope and interior can be achieved from 3D convection simulations for stellar evolution models. Such improvements to stellar structure models partly eliminates the structural contribution to the surface effect, with discrepancies having decreased from about 10 to some $2\ \mu\text{Hz}$. Hence the patched models do not yet perform to the level of precision of the asteroseismic data. Moreover, the patching procedures do not deliver reliable post-main-sequence evolution models when performed near the bottom of the convective envelope in currently available 3D simulations. More refined 3D simulations for deeper convective envelopes are needed to improve stellar evolution theory of evolved low-mass stars even further, keeping in mind numerical restrictions (cf., Silva Aguirre et al., 2020).

In addition to global frequency shifts due to surface effects, the p-mode frequencies also undergo time-dependent variability connected with magnetic activity. For the Sun this effect was summarized by Christensen-Dalsgaard (2002). Magnetic effects were found for the solarlike p modes detected in CoRoT data of the F5V star HD 49933 (García et al., 2010). The *Kepler* data allowed such activity [pulsation connections studied in samples of F-type stars (Mathur et al., 2014) and in the legacy sample (Santos et al., 2019)], revealing that the p-mode frequency shifts increase with increasing chromospheric activity, increasing metallicity, and increasing effective temperature. Young rapid rotators reveal larger frequency shifts than old stars. Moreover, the nonspherical nature of the magnetic activity in the stellar convective envelope changes the frequencies of gravitoacoustic modes (Pérez Hernández et al., 2019). While asteroseismic assessments of the physics of stellar activity in terms of its effect on pulsation-mode behavior has progressed significantly, the improved knowledge is not at a level at which it can be used to encode temporal magnetic activity in the theory of stellar evolution. In this sense, the inclusion of the physics of surface convection via patching of time-averaged 3D stellar atmosphere models to 1D stellar interiors across the evolution of low-mass stars, via calibrations of solarlike oscillations based on space asteroseismology, advances more steadily and more targeted than the inclusion of magnetic activity.

D. Improving the theory of angular momentum transport

A major asset of mixed and g modes is their probing power of the deep stellar interior. While this opportunity does not occur for the Sun and Sun-like dwarfs, we now have thousands of stars with the appropriate g modes delivering their interior rotation rates from measured rotational frequency shifts. Such measurements give quasi-direct information about Ω_{core} without having to go through Fig. 16. In that sense, the internal rotation of stars has become observational astronomy. Once the *Kepler* data reached a duration of 2 yr, prominent detections of rotational splitting for dipole mixed modes were found in subgiants by Deheuvels et al. (2012), Deheuvels et al. (2014), and Deheuvels et al. (2020) and in red giants by Beck et al. (2012), Mosser et al. (2012), and Deheuvels et al. (2015). For intermediate-mass dwarfs, both dipole and quadrupole modes with rotationally split multiplets were detected soon after the nominal 4-yr *Kepler* light curves became available, with initial exploitations by Kurtz et al. (2014), Pápics et al. (2014), Pápics et al. (2015), Saio et al. (2015), and Van Reeth et al. (2015). These studies of internal rotation immediately made it clear that the theory of angular momentum transport as we knew it prior to *Kepler* failed to explain the asteroseismic data, with discrepancies of up to 2 orders of magnitude in the measured Ω_{core} .

Many observational derivations of Ω_{core} have been done in recent years, confirming the early findings. For red giants these were summarized by Mosser et al. (2014) and Gehan et al. (2018). The discrepancy between theory and observations turned out to be independent of the measured rotation rate during the core-hydrogen burning, i.e., the problem regarding slower than expected near-core rotation is derived for both the perturbative and TAR regimes of rotation. A summary of the asteroseismic results from mixed and g modes, as well as ways to improve the theory, was offered in the review by Aerts et al. (2019) and is not repeated here. One major conclusion of that paper, which summarized data covering all stages of stellar evolution, is that low- and intermediate-mass stars are to a good approximation quasirigid rotators during their core-hydrogen-burning phase, while Ω_{core} and Ω_{env} values differ by less than a factor of 10 during the RGB phase. The theory of local conservation of angular momentum transport does not explain this. The asteroseismic rotation estimates for 1210 stars across stellar evolution assembled by Aerts et al. (2019) reveal that the CO cores built up inside red giants and subdwarfs by the end of their core-helium-burning phase have the same angular momentum as their white-dwarf successors.

Major updates since the summary by Aerts et al. (2019) have become available and are shown in Fig. 6. A large increase in the sample of dwarfs was achieved by Li et al. (2019b,c, 2020), who derived the near-core rotation

frequencies for more than 600 F-type g-mode pulsators. These are shown in gray in Fig. 6. Almost all of the newly included F-type dwarfs reveal dipole ($l = 1$) prograde modes, while about 30% show quadrupole ($l = 2$) modes, and 16% of them show retrograde Rossby modes. Core rotation rates of 72 core-helium-burning stars have been derived from their dipole mixed modes (Tayar et al., 2019, indicated in blue in Fig. 6). For both of the new samples, there is no asteroseismic estimate of $\log g$, as is the case for all 1210 stars in Fig. 4 given by Aerts et al. (2019), hence Fig. 6 was constructed differently. For the red giants addressed by Tayar et al. (2019), $\log g$ was derived from near-IR APOGEE spectroscopy, while Li et al. (2020) relied on T_{eff} values from Mathur et al. (2017), luminosity estimates from Gaia astrometry computed in Murphy et al. (2019), and a grid of stellar models to derive the gravity. Although this leads to much larger and more systematic uncertainties for $\log g$ than for the asteroseismic $\log g$ values used by Aerts et al. (2019), with uncertainties between 0.2 and 0.5 dex for the stars in Fig. 6 (omitted for clarity), the conclusions by Aerts et al. (2019) are fully confirmed by these additional recent studies, representing a tenfold increase in the number of dwarfs with Ω_{core} .

Following Aerts et al. (2019), two major paths have been followed to try to fix the theory of stellar rotation, given the prominent results from asteroseismology. On the one hand, angular momentum transport by IGWs as proposed by Kumar & Quataert (1997), Rogers et al. (2013), and Rogers (2015), by mixed modes as studied by Belkacem et al. (2015a,b), and by g modes as in Townsend et al. (2018) was considered. On the other hand, instabilities due to magnetic fields, termed the magnetic Tayler instability, were considered an explanation by Fuller et al. (2019), Goldstein et al. (2019), and Eggenberger et al. (2019). Both physical processes lead to a more efficient evacuation of angular momentum from the core to the envelope of the star than any of the processes that were considered in stellar evolution computations prior to space asteroseismology. While these new theoretical ingredients improve the discrepancies between the asteroseismic measurements of Ω_{core} and stellar evolution theory, they still require one to tweak the amount of angular momentum transported from the core to the surface with a free parameter in order to achieve compliance with the measured core rotation rates. Currently, none of the theories are able to explain the quasirigid rotation measured for stars with ratios of $\Omega/\Omega_{\text{crit}} \in [0, 75\%]$ during the core-hydrogen burning phase, as displayed in the right panel of Fig. 6.

Van Reeth et al. (2016), Ouazzani et al. (2017), Van Reeth et al. (2018), Christophe et al. (2018), and Li et al. (2020) measured Ω_{core} for a sample of ~ 650 γ Dor stars. A dedicated study by Van Reeth et al. (2018) on 37 of those pulsators with high-precision spectroscopy allowed them to assess whether the stars have differential enve-

lope rotation while relying on the theoretical formalism derived by Mathis (2009) as a generalization of the TAR. Van Reeth et al. (2018) combined g-mode estimation of Ω_{core} with either a p-mode estimation of Ω_{env} or a derivation of Ω_{surf} from rotational modulation. Li et al. (2020) added 58 more stars to conclude that the rotation is almost rigid to within 5% for all 95 single F-type dwarfs.

Ongoing modeling work considers two more improvements in addition to the TAR with differential rotation. One generalization takes into account the occurrence of an axisymmetric magnetic field with poloidal and toroidal components following the perturbative approach for the magnetism and was elaborated upon by Prat et al. (2019). The new dispersion relation derived by Prat et al. (2019) allows one to assess how such a field affects the g-mode period-spacing pattern. It was found that an interior magnetic field with strength above 10^5 G leads to pertinent spiky deviations from the tilted period-spacing patterns (Van Beeck et al., 2020) that are in principle detectable. These deviating signals have not yet been identified in *Kepler* data on g-mode pulsators such as those shown in Figs. 11 and 12. Another generalization of the TAR was derived by Mathis & Prat (2019), who computed a new dispersion relation for slightly deformed stars including the centrifugal acceleration. The impact of this inclusion is limited relative to the magnetic effects for rotation rates up to $\sim 70\% \Omega_{\text{crit}}$ (Henneco et al., 2021).

E. Inference of internal mixing from g modes

In this section we concentrate on stars of intermediate mass with a radiative envelope. Such stars are much more rapid rotators than low-mass stars with a convective envelope because they do not experience magnetic braking. Models of intermediate-mass stars computed by relying on the Schwarzschild or Ledoux criteria of convection, without extra mixing in the near-core region, have convective core masses that are too low. This is deduced from comparing high-accuracy model-independent dynamical masses of double-lined eclipsing binaries to those of stellar evolution models across a wide mass range of $M_{\star} \in [1.2; 17] M_{\odot}$ covered by Torres et al. (2010), Claret & Torres (2019), and Tkachenko et al. (2020). The need for higher convective core masses for eclipsing binaries stands, irrespective of how $D_{\text{ov}}(r)$ is treated in the isochrone fitting (see Fig. 7), as discussed by Constantino & Baraffe (2018), Costa et al. (2019), and Johnston et al. (2019b). Masses of fully mixed convective cores may also be derived from a model-dependent isochrone fitting of the observed extended main-sequence turn-offs (eMSTO). This was done for numerous young open clusters observed by the Hubble and Gaia space telescopes (Goudfrooij et al., 2018; Li et al., 2019a). Interpretation of the shape and diversity of observed eMSTOs was

done mainly by including rotational mixing (e.g., Bastian et al., 2018; Gossage et al., 2018) or magnetism (Georgy et al., 2019) in the stellar evolution models. Other causes of mixing, such as the pulsational or tidal wave mixing discussed in Sec. II.A, are usually ignored. Inclusion of $D_{\text{ov}}(r)$ and $D_{\text{mix}}(r)$ profiles calibrated by asteroseismology of single field stars can explain some of the eMSTO properties of young open clusters, thereby impacting their aging. Imposing the asteroseismic results on cluster isochrone fitting allows for higher convective core masses for all stars with $M_{\star} \geq 1.2 M_{\odot}$ (Johnston et al., 2019a). Cluster aging is a typical area where asteroseismology can be of interest to other fields in astrophysics.

Asteroseismology has provided evidence for the need of higher-than-standard masses of convective cores, in all evolutionary stages and for a large range of stellar masses covering $M_{\star} \in [1.1, 25] M_{\odot}$. Backtracking the asteroseismic masses of white dwarfs to earlier evolutionary phases requires more massive helium cores, as discussed by Hermes et al. (2014), Hermes et al. (2017a), and Hermes et al. (2017b). The detailed derivation of the larger-than-expected inferred CO core mass of $M_{\text{cc}} = 0.45 M_{\odot}$ of the pulsating white dwarf KIC 08626021 (Giannichele et al., 2018) is exemplary of the details that can be derived on the chemical stratification (in this case of oxygen, carbon, and helium) from the exploitation of g modes. The core mass of this white dwarf is about 40% higher than expected from standard evolution models and points to the need for more CBM at earlier phases of stellar evolution. The immediate progenitors of the white dwarfs, i.e., the red-giant and subdwarf stars, also reveal the need for CBM and higher core masses than those predicted in stellar evolution theory. This was quantified for three subdwarf B pulsators by Van Grootel et al. (2010a), Van Grootel et al. (2010b), and Charpinet et al. (2011). These case studies resulted in constraints on the inner He/C/O core from their g modes. Thus, stars not only transport more angular momentum when they have a convective core, they also have CBM resulting in more massive mixed cores than anticipated. This need is most outspoken during the core-hydrogen-burning phase of stellar evolution, so we focus on dwarfs in the rest of this section.

Prior to space asteroseismology, estimation of $D_{\text{ov}}(r)$ assuming convective penetration in Zahn’s prescription (Zahn, 1991) led to a wide range of values covering $d_{\text{pen}} \in [0.1, 0.5] H_p$ for β Cep pulsators (Aerts, 2015), but uncertainties from ground-based asteroseismology remained large ($\gtrsim 0.1$). At the low-mass end, an extreme case requiring a large overshoot is the F5-type $M_{\star} \simeq 1.5 M_{\odot}$ solarlike p-mode pulsator Procyon. Guenther et al. (2014) modeled its p modes from equilibrium models with various prescriptions for $D_{\text{ov}}(r)$ as of the ZAMS, considering a radiative or adiabatic temperature gradient and penetration as well as diffusive overshoot. This led to a fully mixed convective core mass

of $M_{\text{cc}}/M_{\star} = 12.4\%$. Space asteroseismology delivered a better estimation of $D_{\text{ov}}(r)$ and $D_{\text{env}}(r)$ from an application of the method in Fig. 16. Most studies had not yet been able to deduce the functional form of the profiles for $D_{\text{ov}}(r)$ and $D_{\text{mix}}(r)$ but had assessed the global level of internal mixing using a forward method, adopting parametrized profiles such as those shown in Fig. 7. The CBM levels and M_{cc} estimates from *Kepler* g-mode asteroseismology of a sample of 37 γ Dor stars for which high-resolution spectroscopy is available revealed equally well explained internal mixing by convective penetration as by diffusive overshooting when using the observational trio $\mathbf{Y}^{\text{obs}} = (\Pi_0, \log T_{\text{eff}}, \log g)$ in the modeling via Fig. 16, after estimation of Ω_{core} as shown in Fig. 6 (gray circles). The results for the asteroseismic estimation of the stellar parameters $\theta = (M_{\star}, \Omega_{\text{core}}, D_{\text{ov}}, \tau, Z_{\text{ini}})$ revealed $M_{\text{cc}}/M_{\star} \in [8, 12]\%$ for the sample, which covers the mass range $M_{\star} \in [1.3, 1.9] M_{\odot}$, rotation rates $\Omega_{\text{core}} \in [0, 25] \mu\text{Hz}$ (i.e., $\Omega_{\text{core}}/\Omega_{\text{crit}} \in [0, 70]\%$), and the entire core-hydrogen-burning phase (Fig. 7 in Mombarg et al., 2019). On the other hand, asteroseismology based on solarlike p modes of nine stars analyzed by Deheuvels et al. (2016) and Hj\o rringgaard et al. (2017) covering $M_{\star} \in [1.12, 1.58] M_{\odot}$ resulted in $M_{\text{cc}}/M_{\star} \in [3, 18]\%$, again with equally good results for convective penetration and exponential diffusive overshooting and for models without and with atomic diffusion (the latter without radiative levitation). Angelou et al. (2020) revisited aspects of the methodology to derive M_{cc} and applied it to 13 stars with solarlike oscillations to arrive at $M_{\text{cc}}/M_{\star} \leq 14\%$, covering the mass range $M_{\star} \in [0.75, 1.45] M_{\odot}$.

Pedersen et al. (2021) fitted measured dipole g-mode period spacings for a sample of 26 *Kepler* SPB pulsators, using eight grids of stellar models with different CBM and envelope mixing profiles (shown in Fig. 7). This homogeneous asteroseismic study, via application of the method in Fig. 16 for $\mathcal{P} = 8$ and $\mathcal{N} = 26$, is the first of its kind for this mass regime, covering stars with a convective core and radiative envelope. It covers the entire main-sequence phase and allowed to infer the overall mixing levels calibrated by the detected dipole g modes for each of the stars and for each of the eight model grids, limiting the solutions for each star to its measured spectroscopic and astrometric values of T_{eff} , $\log g$, and $\log(L/L_{\odot})$. Pedersen et al. (2021) found that 17 of the 26 stars were best modeled via convective penetration and 9 out of 26 with exponential diffusive overshooting; see Fig. 7. Moreover, stellar models with a stratified envelope mixing profile (due to vertical shear or IGWs as graphically depicted in Fig. 7) deliver better asteroseismic fits to the data than unstructured mixing profiles. This study revealed asteroseismic estimates $M_{\text{cc}}/M_{\star} \in [6, 29]\%$ for the mass range $M_{\star} \in [3.3, 8.9] M_{\odot}$ and rotation rates covering $\Omega_{\text{core}} \in [0.35, 21.8] \mu\text{Hz}$ corresponding to $\Omega_{\text{core}}/\Omega_{\text{crit}} \in [3, 96]\%$. The level of envelope mixing at the bottom of the radiative envelope, where

TABLE I Inferred convective core masses from estimation of $D_{\text{ov}}(r)$ and $D_{\text{mix}}(r)$ via Fig. 16 for three samples of single dwarf pulsators discussed in the text. The level of mixing at the bottom of the radiative envelope D_{env} covers a wide range for B stars.

Sample	Spectral Type	Mass range	M_{cc}/M_{\star} range	$\Omega/\Omega_{\text{crit}}$ range	D_{env} range
~20 solarlike pulsators	Later than F2	[1.1, 1.6] M_{\odot}	[3, 18] %	< 10 %	?
~40 g-mode pulsators	F0 – F2	[1.3, 1.9] M_{\odot}	[7, 12] %	[0, 70] %	< 10 $\text{cm}^2 \text{s}^{-1}$
~30 g-mode pulsators	B3 – B9	[3.3, 8.9] M_{\odot}	[6, 29] %	[3, 96] %	[12.0, 8.7×10^5] $\text{cm}^2 \text{s}^{-1}$

the outer boundary of the $D_{\text{ov}}(r)$ profile occurs (i.e., at the interface of the purple and pink profiles in Fig. 7) reveals a large range for this sample of 26 stars, with values between 12.0 and $8.7 \times 10^5 \text{cm}^2 \text{s}^{-1}$. In contrast to the results for F-type g-mode pulsators, this highlights the need for considerable envelope mixing in several of these B-type stars. It is found that the level of mixing at the bottom of the envelope is mildly correlated (correlation coefficient of 0.61) with the rotation frequency in that region. A summary of the asteroseismic inferences of M_{cc}/M_{\star} , via an estimation of $D_{\text{ov}}(r)$ and $D_{\text{env}}(r)$ from imposed profiles as in Fig. 7, is provided in Table I.

Further improvements in asteroseismic modeling can come from the inclusion of microscopic atomic diffusion in the equilibrium models. Deal et al. (2017), Deal et al. (2018), and Deal et al. (2020) assessed the impact of adding radiative accelerations to model p-mode pulsators with a convective envelope. They compared frequency predictions from 1D models based on atomic diffusion to those from 1D models without diffusion or where it is treated in a simplified way such as by restricting to gravitational settling (of helium or heavier elements). Their studies are based on 1D equilibrium models computed with the CESTAM code (Marques et al., 2013), including an advective and diffusive treatment of rotation. Deal et al. (2020) found that the inclusion of radiative levitation is necessary to achieve reliable values for the p modes of the F-type stars in the *Kepler* legacy sample with $M_{\star} > 1.45 M_{\odot}$, even in the presence of macroscopic rotational mixing. The latter was found to be the dominant element transport process in stars with $M < 1.3 M_{\odot}$, while microscopic and macroscopic mixing are of equal importance for the mass range $1.3 M_{\odot} < M < 1.45 M_{\odot}$. The importance of radiative levitation for g-mode asteroseismology has been assessed only for two slowly pulsating γ Dor stars so far. This also points to the need to include this process (Mombarg et al., 2020, see also Fig. 5).

The capacity to infer internal mixing profiles, as well as the thermal structure in the CBM region of stars with a convective core was assessed for dwarfs by Pedersen et al. (2018) and Michielsen et al. (2019) and for core-helium-burning stars by Constantino et al. (2017). These studies have yet to be put into practice. The full potential

of the *Kepler* data on this front remains underexploited, given that g-mode asteroseismology of dwarfs only saw its beginnings since five years and that modeling for ensembles of stars following the scheme in Fig. 16 is a tedious and time-consuming task. Nevertheless, Table I reveals a large range of envelope mixing in stars of similar mass, metallicity, and evolutionary stage during the main sequence, reflecting the fact that nonlinear interactions between rotation, waves, microscopic atomic diffusion, and magnetism may be at work. Refined calibrations of the mixing due to this multitude of phenomena requires ensemble modeling of g-mode pulsators for hundreds of stars treated in a homogeneous way, instead of the few tens addressed thus far.

F. The beginnings of tidal asteroseismology

In all of the previous cases, we considered oscillations based upon 1D equilibrium models computed under the assumption of a single star. However, a large fraction of stars occurs in binaries, where tidal forces and tidal interactions come into play. The binary fraction among stars increases as the stellar birth mass increases. On average, half of the stars occur in binaries but the occurrence rate for high-mass stars is much higher than for low-mass stars, as high as $\sim 80\%$ for O-type stars. Their evolution is dominated by binary interactions (Sana et al., 2012).

As long as the orbital separation of the two components or the mass ratio is such that tides can be ignored, the asteroseismic modeling can be done as with single pulsators. The orbital motion may offer stringent and model-independent dynamical masses, particularly for detached double-lined spectroscopic eclipsing binaries. Some wide binaries reveal two pulsating components in the Fourier transform such that isochrone fitting offers extra constraints compared to the case of a single pulsator. The α Cen system is a prototypical example of this (e.g. Miglio & Montalbán, 2005). Other binaries with space photometry covering a variety of pulsating components treated as if concerning a single star were analyzed by Telting et al. (2012), Frandsen et al. (2013), Maxted et al. (2013), Beck et al. (2014), Appourchaux et al. (2015), Gaulme et al. (2016), Baran et al. (2016),

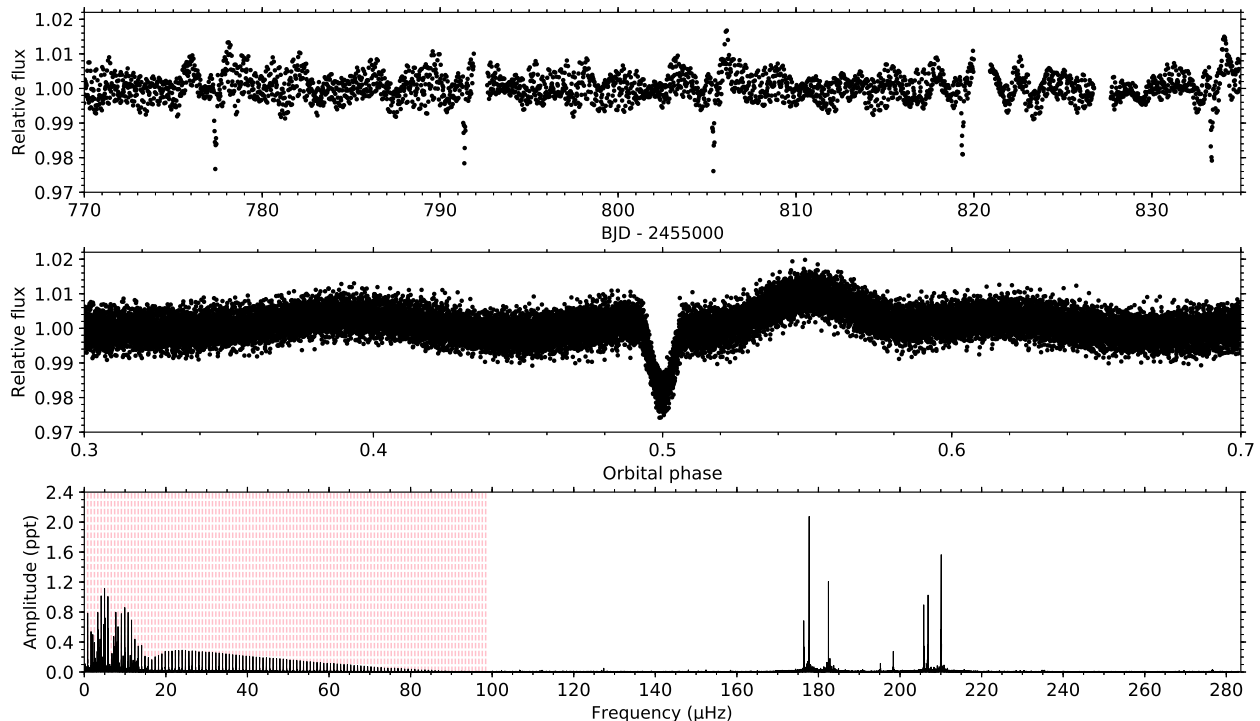


FIG. 19 Excerpt of the *Kepler* light curve (top), phase folded according to an orbital period of 14 d (middle panel), and the corresponding LS amplitude spectrum (bottom panel) of KIC 4142768. This eclipsing binary reveals self-excited κ -driven p modes and tidally excited g modes occurring at exact multiples of the orbital frequency (indicated in red). Figure based on data in Guo et al. (2019) by courtesy of Timothy Van Reeth, KU Leuven.

Themeßl et al. (2018), Kern et al. (2018), and Brogaard et al. (2018). These studies led to stringent constraints on the global stellar parameters thanks to the binarity.

Tidal asteroseismology treats the case of binaries for which the tide-generating potential cannot be ignored in the force balance. For a close binary in which the tidal forces occur in the term \mathbf{f} in Eq. (19), the tides come into play at the level of the equilibrium models and for the computation of the oscillations. In such a case, the binarity of a pulsating component implies a complication for an asteroseismic analysis. At the same time, it may offer unique opportunities to test the effects of tidal forces on stellar structure and evolution from tidally excited or tidally affected oscillations. The properties of such oscillations differ from those of self-excited or stochastically excited oscillations in that they are connected with the orbital frequency, and they therefore offer additional opportunities to probe stellar interiors than modes in single stars. Moreover, tidally excited oscillations may get locked into resonance with the orbit and have a major effect on the evacuation of orbital energy, efficiently changing the binary evolution (e.g., Papaloizou & Savonije, 1997; Savonije & Papaloizou, 1997; Witte & Savonije, 1999). Given that the tides come into play and that orbital periods are of the order of days, tidally ex-

cited oscillations usually are g modes. However, tidally affected oscillations may also occur among p modes, as found in the close binaries U Gru (Bowman et al., 2019c) and V453 Cyg (Southworth et al., 2020).

Currently, asteroseismic probing to improve the internal structure from tidal oscillations remains limited. This is not due to a lack of candidate pulsators, as systematic searches for oscillations in eclipsing binaries with CoRoT and *Kepler* revealed hundreds of cases (Gaulme & Guzik, 2019). Rather, the data analysis to deduce the oscillatory properties is extremely challenging. Iterative schemes have to be devised to unravel the frequencies due to the orbital motion, synchronous, subsynchronous or supersynchronous rotation, and pulsations. Once again, CoRoT paved the way to the first proper monitoring and iterative orbital and pulsational light-curve modeling of close binaries with g modes by (Maceroni et al., 2009) and Maceroni et al. (2013) and with p modes (da Silva et al., 2014).

The real breakthrough in the discovery and analysis of tidal oscillations in numerous close binaries came for the 4-yr nominal *Kepler* light curves. We already showed and discussed the light curve and Fourier transform of the prototype of high-eccentric binaries with tidally excited modes found by Welsh et al. (2011) in Sec. III.A (Fig. 15).

That was a case where almost all detected frequencies are exact multiples of the orbital frequency, as expected for dynamical tides. Another situation occurs for the binary KIC 4142768 whose light curve is illustrated in Fig. 19 and discussed by Guo et al. (2019). This is an eclipsing binary with two evolved A-type stars in an eccentric orbit with a period of 14 d. This pulsating binary reveals low-frequency g modes, some but not all of which occur at exact multiples of the orbital frequency (indicated with the red vertical lines in Fig. 19). The binary also undergoes κ -driven δ Sct-type p modes in the frequency range 170–220 μ Hz. Spectroscopic follow-up with the HIRES spectrograph at Keck revealed a surface rotation rate only one-fifth of the pseudosynchronous rate at periastron. The tidally excited modes were identified as quadrupole prograde sectoral modes, as anticipated from the theory of dynamical tides (see, Fuller, 2017, for a highly didactical paper on tidally excited oscillations). The frequency range of the detected self-excited modes is compliant with theoretical predictions for the fundamental parameters of the primary, which is a fairly evolved star close to the terminal-age main sequence. The near-core rotation rate derived from the fitting of the data to Eq. (49) corresponds to $\Omega_{\text{core}} = 0.07 \pm 0.03 \mu\text{Hz}$ and points to an extremely slow rotator, which is in agreement with the spectroscopic surface velocity projected on the line of sight.

Various binaries discovered from *Kepler* photometry have revealed an oscillation signal at the equilibrium tide, in addition to g modes triggered by dynamical tides (e.g., KIC 8719324, which was addressed by Thompson et al., 2012). Detailed observational analyses were made for several systems similar to KIC 4142768 that is shown in Fig. 19. Examples are available in Pápics et al. (2013), Murphy et al. (2013a), Debosscher et al. (2013), Hambleton et al. (2013), Borkovits et al. (2014), Hambleton et al. (2016), Guo et al. (2017a,b), Fuller et al. (2017), Hambleton et al. (2018), Guo & Li (2019), Bowman et al. (2019c), Southworth et al. (2020), Handler et al. (2020), and Kurtz et al. (2020), where the latter two papers reported the first cases of tip-tilted oblique binary pulsators. Hardly any of these binary systems have yet been modeled asteroseismically, according to Fig. 16, with the exception of the double hybrid p- and g-mode F-type pulsators KIC 10080943A and KIC 10080943B. Asteroseismic isochrone modeling of the two components revealed the need for extra CBM and higher convective core masses than in standard evolution models for both components, which is in line with Table I (Schmid & Aerts, 2016).

Space photometry continues to deliver a plethora of close binary pulsators, with new discoveries by the day. A large diversity of orbital periods, eccentricities, synchronicities, and oscillation properties have already been found. The extensive paper by Fuller (2017) revisited theories of tidal excitation of nonradial oscillations and

provided predictions for flux variations, mode amplitudes, frequencies, phases, and spin-orbit misalignment based on a nonadiabatic treatment of the equations, including the Coriolis force. Yet, we are only at the beginnings of tidal asteroseismology, because so few systems have been modeled via the scheme in Fig. 16 and we do not yet know how common resonance locking is, nor how important it is in practise for binary evolution and for angular momentum loss. Future modeling work to understand tidal wave transport phenomena in close binaries is in order. Searches for oscillation modes in numerous eclipsing binaries in the TESS data are ongoing. These will undoubtedly uncover objects suitable for better understanding the evolution of massive binaries, including progenitors of future gravitational wave emitters. The TESS sample of high-mass stars observed in its two CVZs holds great potential in this respect.

V. GLORIOUS ROAD MAP FOR THE FUTURE

The past decade has sparked immense interest in asteroseismology. Following the detection of nonradial oscillation modes in ground-based radial-velocity and/or light curves of a few tens of stars, we have moved on to asteroseismology of tens of thousands of stars covering all evolutionary phases. This success results from uninterrupted long-duration space photometric light curves having ppm-level precision. Asteroseismology is delivering an observational calibration of internal rotation and mixing across stellar evolution, as a guide for improving the theory of angular momentum and element transport inside stars. The stellar evolution community is currently digesting this flood of asteroseismic information, given the surprises and challenges that it brought. This will eventually lead to better stellar evolution models, as important input for studies of exoplanetary systems and for the chemical evolution of galaxies.

Much more is to come. While past space missions focused on low- and intermediate-mass stars, the current all-sky TESS mission already delivered data for high-mass stars in the Milky Way and LMC during its first two years of operation, covering masses up to $\sim 50 M_{\odot}$. Prospects are excellent that we may embark upon asteroseismology of high-mass binaries on their way to becoming gravitational wave sources, and of blue supergiants nearing their supernova explosion. The methodology in Fig. 16 is in place but applications should be generalized to a nonadiabatic framework for the oscillations. Moreover, dissection of the maximum amount of information present in the Fourier transforms of the TESS light curves is in order. Asteroseismology based on stochastically excited GIWs looks appealing now that TESS is delivering proper data to guide such a development for high-mass stars. The art will be to distinguish the signatures of coherent gravito-inertial modes and of stochastic GIW as

input for modeling of the stellar interior. Similarly, asteroseismology of pre-main-sequence stars has yet to be put into practice for representative ensembles. Initial studies were based on just a few short light curves (Zwintz et al., 2014), but improvements in the physics of accretion, rotational spin-up, magnetic activity during contraction, and internal mixing of elements as protostars approach their birth are now within reach for asteroseismic scrutiny.

The ongoing NASA TESS and future ESA PLATO missions lift the probing of stellar interiors to all masses and evolutionary stages. With that glorious prospect, asteroseismology is entering the big data era. Machine-learning methods are advantageous for interpreting the massive flux of data but must be applied with proper mathematical modeling, including parameter degeneracies and correlated diagnostics, so as to ascertain appropriate precision estimation of the stellar parameters, among them stellar ages. Ensemble asteroseismology will become ever more powerful when combined with independent and homogeneous nonasteroseismic information coming from all-sky spectroscopic surveys with multi-object spectrographs such as SDSS-V (all-sky, near IR, Kollmeier et al., 2017, time frame 2020–2024), WEAVE (Northern Hemisphere, optical, Dalton et al., 2018, time frame 2020+), and 4MOST (Southern Hemisphere, optical, de Jong et al., 2019, time frame 2022–2026), along with the final Gaia all-sky space astrometry.

On the theory front, nonlinear asteroseismology has to be redeveloped in this space era. This has major potential given that a high percentage of pulsators reveal departures from linearity and evidence for nonlinear resonant mode coupling. Such coupling occurs in oscillation spectra across all masses and evolutionary stages. Having been found in CoRoT data of B and Be stars by Degroote et al. (2009) and Huat et al. (2009), it has also been detected in BRITe data of Be stars (Baade et al., 2018) and in *Kepler* photometry of young intermediate-mass stars (Bowman et al., 2016), of subdwarf pulsators (Baran et al., 2012), and in various white dwarfs (Hermes et al., 2015). This observational gold mine is awaiting exploitation in terms of the nonlinear probing of stellar interiors once a modern theoretical framework gets developed, as in Zong et al. (2016a). Similarly, magnetoasteroseismology is still in its infancy. Mode predictions for stellar models with strongly magnetic cores have been triggered to explain mode suppression in red giants by Loi (2020) and Bugnet et al. (2021). Backtracking the results for red giants, their intermediate-mass main-sequence progenitors should also have strong internal magnetic fields. Such fields have a non-negligible effect on g modes, as shown by the theoretical developments in Prat et al. (2020) and their magnetic signatures predicted by Van Beeck et al. (2020). While these have not yet been found in g-mode period-spacing patterns of *Kepler* dwarfs, this might be because they have not been looked for with dedicated eyes or with machine-learning

artillery.

Finally, we come back to the use of 1D equilibrium models. Several of the stars in Fig. 6 rotate faster than 70% of their critical rotation frequency. Their asteroseismic modeling will benefit from a 2D treatment. The code ROTORC by Deupree (2001) delivers 2D equilibrium models and was used to make pulsation predictions for p modes of β Cep pulsators (see Fig. 1) by Lovekin & Deupree (2008) and Lovekin et al. (2009). These predictions were not used in asteroseismic modeling so far. The public code ESTER (Évolution STEllaire en Rotation, Rieutord et al., 2016) is under active development and is advanced in terms of the treatment of transport processes. This code has great potential given the need for improvements in models of the fastest rotating intermediate- and high-mass dwarfs. ESTER delivers 2D axisymmetric static structure models but does not yet treat the chemical evolution of the star, nor 2D mass loss or envelope convection. Proper boundary conditions, including a dynamical wind via 2D nonlocal thermodynamic equilibrium atmosphere models (e.g., Petrenz & Puls, 2000), are necessary to improve pulsation predictions for fast rotators. While the current limitations of ESTER can be partially circumvented by fixing the hydrogen mass fraction in the convective core to a seismic estimate of X_c as in a recent application to the δ Sct star Altair (rotating at $\sim 74\%$ of its critical velocity, Bouchaud et al., 2020), future developments to turn the code into a full-blown 2D stellar evolution tool would be highly beneficial. This would allow researchers to perform 2D asteroseismic modeling of the most rapid rotators in Fig. 6, and of the high-mass pulsators discovered by Pedersen et al. (2019), Burssens et al. (2020), Bowman et al. (2020), and Dorn-Wallenstein et al. (2020), in addition to new ones yet to be discovered.

Tremendous progress in our understanding of stellar interiors has been achieved, thanks to the beauty of non-radial oscillation theory coupled with space photometry of ppm-level precision for thousands of stars. Asteroseismology turned the study of stellar interiors into an observational science. Its future is extremely bright in all aspects of this research field, from instrumentation and ongoing or planned surveys all the way up to fundamental theory. Major improvements for stellar evolution theory based on asteroseismology are under way for single stars, binaries, and star clusters. We thus end with a kind invitation to those readers whose curiosity might be triggered but who have not yet been active in this field: it is never too late to become an asteroseismologist. . .

ACKNOWLEDGMENTS

The writing of this review was initiated while I was lecturing as the 2019 Oort Professor at Leiden Observatory, the Netherlands, and at the Max Planck Institute of As-

tronomy in Heidelberg, Germany. I am grateful for the kind hospitality at both places, and for the genuine interest in my lectures expressed by young and not-so-young attendees; this made those stays particularly enjoyable. I am also grateful to many colleagues, too numerous to mention, whose inspiring lectures and tutorials educated me in astrophysics in general, and in the computation of numerical stellar models and their oscillation frequencies in particular. Trained as a pure theoretician at master level, I benefited greatly from practical introductions to astronomical observing with various telescopes during my PhD and postdoctorate trajectories. Undertaking the full journey from early instrument concepts to detailed modeling of stellar interiors, in a multicultural and inclusive team spirit, has been crucial for my motivation and inspirational for my supervision and training of the next generations of astrophysicists. The PhD students and postdoctoral researchers in the Leuven asteroseismology team, colleagues from the community, and three referees are thanked for their comments on early versions of the manuscript. I am particularly grateful to my local python-artists-in-residence, Dominic Bowman, Cole Johnston, Joey Mombarg, Péter Pápics, May Gade Pedersen, and Timothy Van Reeth for having produced figures for this review. Appreciation is also given to Ashley Chontos, Philipp Edelmann, Sylvia Ekström, Gang Li, Tami Rogers, Jamie Tayar, and Kuldeep Verma for providing data or figures in electronic form. Those participants of the conference “*Stars and Their Variability Observed from Space*” held in Vienna, Austria, in August 2019, who took part in the end-of-conference poll on how our research field should progress, are thanked for their cooperation; the outcome of the poll shaped the final section of this review.

I acknowledge funding from the KU Leuven Research Council (grant C16/18/005: PARADISE). The funding received from the European Research Council (ERC) under the European Union’s Seventh Framework (FP7/2007–2013/ERC Grant Agreement No. 227224: PROSPERITY, 2009–2013) and Horizon 2020 Research and Innovation Programme (Grant Agreement No. 670519: MAMSIE, 2016–2020) has been essential for the development of my long-term research goals and aspirations in gravity-mode asteroseismology. The ERC has allowed me to transform my narrow, bumpy, unconventional path into a broad, royal road.

REFERENCES

- Aerts, C. 2015, in IAU Symposium, Vol. 307, New Windows on Massive Stars, ed. G. Meynet, C. Georgy, J. Groh, & P. Stee, 154–164
- Aerts, C., Bowman, D. M., Símón-Díaz, S., et al. 2018a, *MNRAS*, 476, 1234
- Aerts, C., Christensen-Dalsgaard, J., & Kurtz, D. W. 2010, *Asteroseismology*, Astronomy and Astrophysics Library, Springer Berlin Heidelberg
- Aerts, C., De Cat, P., Kuschnig, R., et al. 2006, *Astrophys. J. Lett.*, 642, L165
- Aerts, C., Mathis, S., & Rogers, T. M. 2019, *Annu. Rev. Astron. Astrophys.*, 57, 35
- Aerts, C., Molenberghs, G., Michielsen, M., et al. 2018b, *Astrophys. J. Suppl. Ser.*, 237, 15
- Aerts, C. & Rogers, T. M. 2015, *Astrophys. J. Lett.*, 806, L33
- Aerts, C., Símón-Díaz, S., Bloemen, S., et al. 2017a, *Astron. Astrophys.*, 602, A32
- Aerts, C., Van Reeth, T., & Tkachenko, A. 2017b, *Astrophys. J. Lett.*, 847, L7
- Alvan, L., Brun, A. S., & Mathis, S. 2014, *Astron. Astrophys.*, 565, A42
- Alvan, L., Strugarek, A., Brun, A. S., Mathis, S., & Garcia, R. A. 2015, *Astron. Astrophys.*, 581, A112
- An, D., Terndrup, D. M., Pinsonneault, M. H., et al. 2007, *Astrophys. J.*, 655, 233
- Anders, F., Chiappini, C., Minchev, I., et al. 2017a, *Astron. Astrophys.*, 600, A70
- Anders, F., Chiappini, C., Rodrigues, T. S., et al. 2017b, *Astron. Astrophys.*, 597, A30
- Anderson, R. I. & Riess, A. G. 2018, *Astrophys. J.*, 861, 36
- Angelou, G. C., Bellinger, E. P., Hekker, S., & Basu, S. 2017, *Astrophys. J.*, 839, 116
- Angelou, G. C., Bellinger, E. P., Hekker, S., et al. 2020, *MNRAS*, 493, 4987
- Appourchaux, T. 2014, A crash course on data analysis in asteroseismology, 123
- Appourchaux, T., Antia, H. M., Ball, W., et al. 2015, *Astron. Astrophys.*, 582, A25
- Appourchaux, T., Benomar, O., Gruberbauer, M., et al. 2012a, *Astron. Astrophys.*, 537, A134
- Appourchaux, T., Chaplin, W. J., García, R. A., et al. 2012b, *Astron. Astrophys.*, 543, A54
- Appourchaux, T., Michel, E., Auvergne, M., et al. 2008, *Astron. Astrophys.*, 488, 705
- Arnett, W. D., Meakin, C., Hirschi, R., et al. 2019, *Astrophys. J.*, 882, 18
- Asplund, M., Grevesse, N., Sauval, A. J., & Scott, P. 2009, *Annu. Rev. Astron. Astrophys.*, 47, 481
- Augustson, K. C. & Mathis, S. 2019, *Astrophys. J.*, 874, 83
- Augustson, K. C., Mathis, S., & Astoul, A. 2020, *Astrophys. J.*, 903, 90
- Auvergne, M., Bodin, P., Boissard, L., Buey, J. T., & Chaintreuil, S. 2009, *Astron. Astrophys.*, 506, 411
- Baade, D., Pigulski, A., Rivinius, T., et al. 2018, *Astron. Astrophys.*, 610, A70
- Baade, D., Rivinius, T., Pigulski, A., et al. 2016, *Astron. Astrophys.*, 588, A56
- Baglin, A., Auvergne, M., Barge, P., et al. 2009, in IAU Symposium, Vol. 253, Transiting Planets, ed. F. Pont, D. Sasselov, & M. J. Holman, 71–81
- Ball, W. H., Beeck, B., Cameron, R. H., & Gizon, L. 2016, *Astron. Astrophys.*, 592, A159
- Ball, W. H. & Gizon, L. 2014, *Astron. Astrophys.*, 568, A123
- Ball, W. H. & Gizon, L. 2017, *Astron. Astrophys.*, 600, A128
- Ballot, J., Gizon, L., Samadi, R., et al. 2011, *Astron. Astrophys.*, 530, A97
- Ballot, J., Lignières, F., Reese, D. R., & Rieutord, M. 2010, *Astron. Astrophys.*, 518, A30
- Balona, L. A. 2014, *MNRAS*, 439, 3453
- Baran, A. S., Reed, M. D., Stello, D., et al. 2012, *MNRAS*, 424, 2686

- Baran, A. S., Telting, J. H., Németh, P., et al. 2016, *Astron. Astrophys.*, 585, A66
- Barban, C., Deheuvels, S., Baudin, F., et al. 2009, *Astron. Astrophys.*, 506, 51
- Barban, C., Matthews, J. M., De Ridder, J., et al. 2007, *Astron. Astrophys.*, 468, 1033
- Bastian, N., Kamann, S., Cabrera-Ziri, I., et al. 2018, *MNRAS*, 480, 3739
- Bastien, F. A., Stassun, K. G., Basri, G., & Pepper, J. 2013, *Nature*, 500, 427
- Basu, S. & Chaplin, W. J. 2017, *Asteroseismic Data Analysis: Foundations and Techniques*
- Basu, S. & Kinnane, A. 2018, *Astrophys. J.*, 869, 8
- Basu, S., Mazumdar, A., Antia, H. M., & Demarque, P. 2004, *MNRAS*, 350, 277
- Bazot, M., Benomar, O., Christensen-Dalsgaard, J., et al. 2019, *Astron. Astrophys.*, 623, A125
- Bazot, M., Bourguignon, S., & Christensen-Dalsgaard, J. 2012, *MNRAS*, 427, 1847
- Bazot, M., Ireland, M. J., Huber, D., et al. 2011, *Astron. Astrophys.*, 526, L4
- Beck, P. G., Bedding, T. R., Mosser, B., et al. 2011, *Science*, 332, 205
- Beck, P. G., Hambleton, K., Vos, J., et al. 2014, *Astron. Astrophys.*, 564, A36
- Beck, P. G., Montalbán, J., Kallinger, T., et al. 2012, *Nature*, 481, 55
- Bedding, T. R., Butler, R. P., Kjeldsen, H., et al. 2001, *Astrophys. J. Lett.*, 549, L105
- Bedding, T. R., Huber, D., Stello, D., et al. 2010, *Astrophys. J. Lett.*, 713, L176
- Bedding, T. R., Mosser, B., Huber, D., et al. 2011, *Nature*, 471, 608
- Bedding, T. R., Murphy, S. J., Colman, I. L., & Kurtz, D. W. 2015, in *European Physical Journal Web of Conferences*, Vol. 101, *European Physical Journal Web of Conferences*, 01005
- Bedding, T. R., Murphy, S. J., Hey, D. R., et al. 2020, *Nature*, 581, 147
- Belkacem, K., Dupret, M. A., Baudin, F., et al. 2012, *Astron. Astrophys.*, 540, L7
- Belkacem, K., Goupil, M. J., Dupret, M. A., et al. 2011, *Astron. Astrophys.*, 530, A142
- Belkacem, K., Marques, J. P., Goupil, M. J., et al. 2015a, *Astron. Astrophys.*, 579, A31
- Belkacem, K., Marques, J. P., Goupil, M. J., et al. 2015b, *Astron. Astrophys.*, 579, A30
- Belkacem, K., Samadi, R., Goupil, M. J., & Dupret, M. A. 2008, *Astron. Astrophys.*, 478, 163
- Belkacem, K., Samadi, R., Goupil, M.-J., et al. 2009, *Science*, 324, 1540
- Bell, K. J., Hermes, J. J., Bischoff-Kim, A., et al. 2015, *Astrophys. J.*, 809, 14
- Bellinger, E. P. 2019, *MNRAS*, 486, 4612
- Bellinger, E. P. 2020, *MNRAS*, 492, L50
- Bellinger, E. P., Angelou, G. C., Hekker, S., et al. 2016, *Ap. J.*, 830, 31
- Bellinger, E. P., Basu, S., Hekker, S., & Ball, W. H. 2017, *Astrophys. J.*, 851, 80
- Benomar, O., Baudin, F., Campante, T. L., et al. 2009, *Astron. Astrophys.*, 507, L13
- Bigot, L. & Dziembowski, W. A. 2002, *Astron. Astrophys.*, 391, 235
- Bildsten, L., Ushomirsky, G., & Cutler, C. 1996, *Astrophys. J.*, 460, 827
- Bloemen, S., Hu, H., Aerts, C., et al. 2014, *Astron. Astrophys.*, 569, A123
- Blomme, R., Mahy, L., Catala, C., et al. 2011, *Astron. Astrophys.*, 533, A4
- Borkovits, T., Derekas, A., Fuller, J., et al. 2014, *MNRAS*, 443, 3068
- Bossini, D., Miglio, A., Salaris, M., et al. 2017, *MNRAS*, 469, 4718
- Bossini, D., Vallenari, A., Bragaglia, A., et al. 2019, *Astron. Astrophys.*, 623, A108
- Bouabid, M.-P., Dupret, M.-A., Salmon, S., et al. 2013, *MNRAS*, 429, 2500
- Bouchaud, K., Domiciano de Souza, A., Rieutord, M., Reese, D. R., & Kervella, P. 2020, *Astron. Astrophys.*, 633, A78
- Bouchy, F. & Carrier, F. 2001, *Astron. Astrophys.*, 374, L5
- Bowman, D. M. 2017, *Amplitude Modulation of Pulsation Modes in Delta Scuti Stars*, Jeremiah Horrocks Institute, University of Central Lancashire, Preston, UK. PhD Thesis published in Springer Theses series
- Bowman, D. M., Aerts, C., Johnston, C., et al. 2019a, *Astron. Astrophys.*, 621, A135
- Bowman, D. M., Burssens, S., Pedersen, M. G., et al. 2019b, *Nature Astronomy*, 3, 760
- Bowman, D. M., Burssens, S., Simón-Díaz, S., et al. 2020, *Astron. Astrophys.*, 640, A36
- Bowman, D. M., Johnston, C., Tkachenko, A., et al. 2019c, *Astrophys. J. Lett.*, 883, L26
- Bowman, D. M., Kurtz, D. W., Breger, M., Murphy, S. J., & Holdsworth, D. L. 2016, *MNRAS*, 460, 1970
- Brassard, P., Fontaine, G., Billères, M., et al. 2001, *Astrophys. J.*, 563, 1013
- Brassard, P., Fontaine, G., Wesemael, F., & Hansen, C. J. 1992, *Astrophys. J. Suppl. Ser.*, 80, 369
- Breger, M. 2000, in *Astronomical Society of the Pacific Conference Series*, Vol. 210, *Delta Scuti and Related Stars*, ed. M. Breger & M. Montgomery, 3
- Breger, M., Lenz, P., Antoci, V., et al. 2005, *Astron. Astrophys.*, 435, 955
- Breger, M., Stich, J., Garrido, R., et al. 1993, *Astron. Astrophys.*, 271, 482
- Briquet, M., Aerts, C., Baglin, A., et al. 2011, *Astron. Astrophys.*, 527, A112
- Brogaard, K., Hansen, C. J., Miglio, A., et al. 2018, *MNRAS*, 476, 3729
- Brown, T. M. & Gilliland, R. L. 1994, *Annu. Rev. Astron. Astrophys.*, 32, 37
- Brown, T. M., Gilliland, R. L., Noyes, R. W., & Ramsey, L. W. 1991, *Astrophys. J.*, 368, 599
- Brown, T. M., Latham, D. W., Everett, M. E., & Esquerdo, G. A. 2011, *Astron. J.*, 142, 112
- Buchler, J. R. & Goupil, M. J. 1984, *Astrophys. J.*, 279, 394
- Buchler, J. R., Goupil, M.-J., & Hansen, C. J. 1997, *Astron. Astrophys.*, 321, 159
- Bugnet, L., Prat, V., Mathis, S., et al. 2021, *Astron. Astrophys.*, submitted
- Buldgen, G., Farnir, M., Pezzotti, C., et al. 2019, *Astron. Astrophys.*, 630, A126
- Burgers, J. M. 1969, *Flow Equations for Composite Gases*
- Burssens, S., Bowman, D. M., Aerts, C., et al. 2019, *MNRAS*, 489, 1304
- Burssens, S., Simón-Díaz, S., Bowman, D. M., et al. 2020, *Astron. Astrophys.*, 639, A81
- Buyschaert, B., Aerts, C., Bowman, D. M., et al. 2018, *As-*

- tron. Astrophys.*, 616, A148
- Buyschaert, B., Beck, P. G., Corsaro, E., et al. 2016, *Astron. Astrophys.*, 588, A82
- Buzasi, D. L. 2000, in *The Third MONS Workshop: Science Preparation and Target Selection*, ed. T. Teixeira & T. Bedding, 9
- Buzasi, D. L., Bruntt, H., Bedding, T. R., et al. 2005, *Astrophys. J.*, 619, 1072
- Cameron, C., Saio, H., Kuschnig, R., et al. 2008, *Astrophys. J.*, 685, 489
- Campante, T. L., Lund, M. N., Kuzlewicz, J. S., et al. 2016a, *Astrophys. J.*, 819, 85
- Campante, T. L., Schofield, M., Kuzlewicz, J. S., et al. 2016b, *Astrophys. J.*, 830, 138
- Cantiello, M., Fuller, J., & Bildsten, L. 2016, *Astrophys. J.*, 824, 14
- Cantiello, M., Langer, N., Brott, I., et al. 2009, *Astron. Astrophys.*, 499, 279
- Chaboyer, B., Demarque, P., & Pinsonneault, M. H. 1995, *Astrophys. J.*, 441, 876
- Chaboyer, B. & Zahn, J. P. 1992, *Astron. Astrophys.*, 253, 173
- Chaplin, W. J., Basu, S., Huber, D., et al. 2014, *Astrophys. J. Suppl. Ser.*, 210, 1
- Chaplin, W. J., Houdek, G., Karoff, C., Elsworth, Y., & New, R. 2009, *Astron. Astrophys.*, 500, L21
- Chaplin, W. J. & Miglio, A. 2013, *Annu. Rev. Astron. Astrophys.*, 51, 353
- Charbonnel, C. & Talon, S. 2005, *Science*, 309, 2189
- Charpinet, S., Brassard, P., Giammichele, N., & Fontaine, G. 2019, *Astron. Astrophys.*, 628, L2
- Charpinet, S., Fontaine, G., Brassard, P., et al. 1997, *Astrophys. J. Lett.*, 483, L123
- Charpinet, S., Fontaine, G., Brassard, P., & Dorman, B. 2000, *Astrophys. J. Suppl. Ser.*, 131, 223
- Charpinet, S., Van Grootel, V., Fontaine, G., et al. 2011, *Astron. Astrophys.*, 530, A3
- Chayer, P., Fontaine, G., & Wesemael, F. 1995, *Ap. J. Suppl. Ser.*, 99, 189
- Chiappini, C., Anders, F., Rodrigues, T. S., et al. 2015, *Astron. Astrophys.*, 576, L12
- Chieffi, A. & Limongi, M. 2013, *Astrophys. J.*, 764, 21
- Choi, J., Dotter, A., Conroy, C., & Ting, Y.-S. 2018, *Astrophys. J.*, 860, 131
- Chontos, A., Huber, D., Latham, D. W., et al. 2019, *Astron. J.*, 157, 192
- Christensen-Dalsgaard, J. 1984, in *Space Research in Stellar Activity and Variability*, ed. A. Mangeney & F. Praderie, 11
- Christensen-Dalsgaard, J. 1988, in *IAU Symposium, Vol. 123, Advances in Helio- and Asteroseismology*, ed. J. Christensen-Dalsgaard & S. Frandsen, 295
- Christensen-Dalsgaard, J. 2002, *Rev. of Modern Phys.*, 74, 1073
- Christensen-Dalsgaard, J., Proffitt, C. R., & Thompson, M. J. 1993, *Astrophys. J.*, 403, L75
- Christensen-Dalsgaard, J., Silva Aguirre, V., Cassisi, S., et al. 2020, *Astron. Astrophys.*, 635, A165
- Christensen-Dalsgaard, J. & Thompson, M. J. 1993, *Astron. Astrophys.*, 272, L1
- Christophe, S., Ballot, J., Ouazzani, R. M., Antoci, V., & Salmon, S. J. A. J. 2018, *Astron. Astrophys.*, 618, A47
- Claeskens, G. & Hjort, N. L. 2008, *Model Selection and Model Averaging*, Cambridge Series in Statistical and Probabilistic Mathematics
- Claret, A. & Torres, G. 2019, *Astrophys. J.*, 876, 134
- Compton, D. L., Bedding, T. R., Ball, W. H., et al. 2018, *MNRAS*, 479, 4416
- Constantino, T. & Baraffe, I. 2018, *Astron. Astrophys.*, 618, A177
- Constantino, T., Campbell, S. W., Christensen-Dalsgaard, J., Lattanzio, J. C., & Stello, D. 2015, *MNRAS*, 452, 123
- Constantino, T., Campbell, S. W., & Lattanzio, J. C. 2017, *MNRAS*, 472, 4900
- Corsaro, E. & De Ridder, J. 2014, *Astron. Astrophys.*, 571, A71
- Corsaro, E., De Ridder, J., & García, R. A. 2015, *Astron. Astrophys.*, 579, A83
- Córsico, A. H., Althaus, L. G., Miller Bertolami, M. M., & Kepler, S. O. 2019, *Astron. Astrophys. Rev.*, 27, 7
- Costa, G., Girardi, L., Bressan, A., et al. 2019, *MNRAS*, 485, 4641
- Cowling, T. G. 1941, *MNRAS*, 101, 367
- Cox, J. P. 1980, *Theory of stellar pulsation*, Princeton University Press
- Cox, J. P. & Giuli, R. T. 1968, *Principles of stellar structure*
- Cristini, A., Meakin, C., Hirschi, R., et al. 2016, *Physica Scripta*, 91, 034006
- Cunha, M. S., Aerts, C., Christensen-Dalsgaard, J., et al. 2007, *Astron. Astrophys. Rev.*, 14, 217
- Cunha, M. S., Antoci, V., Holdsworth, D. L., et al. 2019a, *MNRAS*, 487, 3523
- Cunha, M. S., Avelino, P. P., Christensen-Dalsgaard, J., et al. 2019b, *MNRAS*, 490, 909
- Cunha, M. S., Stello, D., Avelino, P. P., Christensen-Dalsgaard, J., & Townsend, R. H. D. 2015, *Astrophys. J.*, 805, 127
- Cuyper, J., Aerts, C., De Cat, P., et al. 2009, *Astron. Astrophys.*, 499, 967
- da Silva, R., Maceroni, C., Gandolfi, D., Lehmann, H., & Hatzes, A. P. 2014, *Astron. Astrophys.*, 565, A55
- Dalton, G., Trager, S., Abrams, D. C., et al. 2018, in *Society of Photo-Optical Instrumentation Engineers (SPIE) Conference Series, Vol. 10702, Proc. SPIE*, 107021B
- Daszyńska-Daszkiewicz, J., Dziembowski, W. A., Pamyatnykh, A. A., & Goupil, M.-J. 2002, *Astron. Astrophys.*, 392, 151
- Daszyńska-Daszkiewicz, J., Pamyatnykh, A. A., Walczak, P., et al. 2017, *MNRAS*, 466, 2284
- Davies, G. R., Chaplin, W. J., Farr, W. M., et al. 2015, *MNRAS*, 446, 2959
- Davies, G. R., Silva Aguirre, V., Bedding, T. R., et al. 2016, *MNRAS*, 456, 2183
- De Cat, P. & Aerts, C. 2002, *Astron. Astrophys.*, 393, 965
- De Gerónimo, F. C., Battich, T., Miller Bertolami, M. M., Althaus, L. G., & Córsico, A. H. 2019, *Astron. Astrophys.*, 630, A100
- de Jong, R. S., Agertz, O., Berbel, A. A., et al. 2019, *The Messenger*, 175, 3
- De Ridder, J., Barban, C., Baudin, F., et al. 2009, *Nature*, 459, 398
- De Ridder, J., Molenberghs, G., Eyer, L., & Aerts, C. 2016, *Astron. Astrophys.*, 595, L3
- Deal, M., Alecian, G., Lebreton, Y., et al. 2018, *Astron. Astrophys.*, 618, A10
- Deal, M., Escobar, M. E., Vauclair, S., et al. 2017, *Astron. Astrophys.*, 601, A127
- Deal, M., Goupil, M. J., Marques, J. P., Reese, D. R., &

- Lebreton, Y. 2020, *Astron. Astrophys.*, 633, A23
- Deal, M., Richard, O., & Vauclair, S. 2016, *Astron. Astrophys.*, 589, A140
- Debosscher, J., Aerts, C., Tkachenko, A., et al. 2013, *Astron. Astrophys.*, 556, A56
- Debosscher, J., Sarro, L. M., Aerts, C., et al. 2007, *Astron. Astrophys.*, 475, 1159
- Deeming, T. J. 1975, *Astrophys. Space sci.*, 36, 137
- Degroote, P., Aerts, C., Baglin, A., et al. 2010a, *Nature*, 464, 259
- Degroote, P., Briquet, M., Auvergne, M., et al. 2010b, *Astron. Astrophys.*, 519, A38
- Degroote, P., Briquet, M., Catala, C., et al. 2009, *Astron. Astrophys.*, 506, 111
- Deheuvels, S., Ballot, J., Beck, P. G., et al. 2015, *Astron. Astrophys.*, 580, A96
- Deheuvels, S., Ballot, J., Eggenberger, P., et al. 2020, *Astron. Astrophys.*, 641, A117
- Deheuvels, S., Brandão, I., Silva Aguirre, V., et al. 2016, *Astron. Astrophys.*, 589, A93
- Deheuvels, S., Bruntt, H., Michel, E., et al. 2010, *Astron. Astrophys.*, 515, A87
- Deheuvels, S., Doğan, G., Goupil, M. J., et al. 2014, *Astron. Astrophys.*, 564, A27
- Deheuvels, S., García, R. A., Chaplin, W. J., et al. 2012, *Astrophys. J.*, 756, 19
- Derekas, A., Kiss, L. L., Borkovits, T., et al. 2011, *Science*, 332, 216
- Deupree, R. G. 2001, *Astrophys. J.*, 552, 268
- Di Mauro, M. P., Ventura, R., Cardini, D., et al. 2016, *Astrophys. J.*, 817, 65
- Dintrans, B., Brandenburg, A., Nordlund, Å., & Stein, R. F. 2005, *Astron. Astrophys.*, 438, 365
- Domiciano de Souza, A., Bouchard, K., Rieutord, M., Espinosa Lara, F., & Putigny, B. 2018, *Astronomy and Astrophysics*, 619, A167
- Domiciano de Souza, A., Kervella, P., Jankov, S., et al. 2003, *Astronomy and Astrophysics*, 407, L47
- Domiciano de Souza, A., Kervella, P., Moser Faes, D., et al. 2014, *Astronomy and Astrophysics*, 569, A10
- Dorn-Wallenstein, T. Z., Levesque, E. M., Neugent, K. F., et al. 2020, *Astrophys. J.*, in press, arXiv:2008.11723
- Dotter, A., Conroy, C., Cargile, P., & Asplund, M. 2017, *Ap. J.*, 840, 99
- Dupret, M.-A., Belkacem, K., Samadi, R., et al. 2009, *Astron. Astrophys.*, 506, 57
- Dupret, M.-A., Grigahcène, A., Garrido, R., Gabriel, M., & Scuflaire, R. 2005, *Astron. Astrophys.*, 435, 927
- Dziembowski, W. A. 1971, *Acta Astron.*, 21, 289
- Dziembowski, W. A. & Goode, P. R. 1992, *Astrophys. J.*, 394, 670
- Dziembowski, W. A., Gough, D. O., Houdek, G., & Sienkiewicz, R. 2001, *MNRAS*, 328, 601
- Dziembowski, W. A. & Pamyatnykh, A. A. 1991, *Astron. Astrophys.*, 248, L11
- Eckart, C. 1960, *Physics of Fluids*, 3, 421
- Edelmann, P. V. F., Ratnasingam, R. P., Pedersen, M. G., et al. 2019, *Astrophys. J.*, 876, 4
- Eggenberger, P., den Hartogh, J. W., Buldgen, G., et al. 2019, *Astron. Astrophys.*, 631, L6
- Fontaine, G., Brassard, P., Charpinet, S., et al. 2003, *Astrophys. J.*, 597, 518
- Foreman-Mackey, D., Hogg, D. W., Lang, D., & Goodman, J. 2013, *Pub. Astron. Soc. Pac.*, 125, 306
- Frandsen, S., Carrier, F., Aerts, C., et al. 2002, *Astron. Astrophys.*, 394, L5
- Frandsen, S., Lehmann, H., Hekker, S., et al. 2013, *Astron. Astrophys.*, 556, A138
- Freytag, B., Ludwig, H.-G., & Steffen, M. 1996, *Astron. Astrophys.*, 313, 497
- Fuller, J. 2017, *MNRAS*, 472, 1538
- Fuller, J., Cantiello, M., Stello, D., Garcia, R. A., & Bildsten, L. 2015, *Science*, 350, 423
- Fuller, J., Hambleton, K., Shporer, A., Isaacson, H., & Thompson, S. 2017, *MNRAS*, 472, L25
- Fuller, J. & Lai, D. 2011, *MNRAS*, 412, 1331
- Fuller, J. & Lai, D. 2012, *MNRAS*, 420, 3126
- Fuller, J., Lecoanet, D., Cantiello, M., & Brown, B. 2014, *Astrophys. J.*, 796, 17
- Fuller, J., Piro, A. L., & Jermyn, A. S. 2019, *MNRAS*, 485, 3661
- Gagnier, D., Rieutord, M., Charbonnel, C., Putigny, B., & Espinosa Lara, F. 2019, *Astronomy and Astrophysics*, 625, A88
- Gaia Collaboration, Babusiaux, C., van Leeuwen, F., Barstow, M. A., et al. 2018, *Astron. Astrophys.*, 616, A10
- Gaia Collaboration, Brown, A. G. A., Vallenari, A., Prusti, T., et al. 2018, *Astron. Astrophys.*, 616, A1
- Gaia Collaboration, Eyer, L., Rimoldini, L., Audard, M., et al. 2019, *Astron. Astrophys.*, 623, A110
- García, R. A. & Ballot, J. 2019, *Living Reviews in Solar Physics*, 16, 4
- García, R. A., Hekker, S., Stello, D., et al. 2011, *MNRAS*, 414, L6
- García, R. A., Mathur, S., Pires, S., et al. 2014, *Astron. Astrophys.*, 568, A10
- García, R. A., Mathur, S., Salabert, D., et al. 2010, *Science*, 329, 1032
- García, R. A., Régulo, C., Samadi, R., et al. 2009, *Astron. Astrophys.*, 506, 41
- García, R. A., Turck-Chièze, S., Jiménez-Reyes, S. J., et al. 2007, *Science*, 316, 1591
- Gaulme, P. & Guzik, J. A. 2019, *Astron. Astrophys.*, 630, A106
- Gaulme, P., McKeever, J., Jackiewicz, J., et al. 2016, *Astrophys. J.*, 832, 121
- Gautschy, A. & Saio, H. 1995, *Annu. Rev. Astron. Astrophys.*, 33, 75
- Gautschy, A. & Saio, H. 1996, *Annu. Rev. Astron. Astrophys.*, 34, 551
- Gehan, C., Mosser, B., Michel, E., Samadi, R., & Kallinger, T. 2018, *Astron. Astrophys.*, 616, A24
- Georgy, C., Charbonnel, C., Amard, L., et al. 2019, *Astron. Astrophys.*, 622, A66
- Georgy, C., Ekström, S., Granada, A., et al. 2013, *Astron. Astrophys.*, 553, A24
- Giammichele, N., Charpinet, S., Fontaine, G., et al. 2018, *Nature*, 554, 73
- Gilliland, R. L., Brown, T. M., Christensen-Dalsgaard, J., et al. 2010, *Pub. Astron. Soc. Pac.*, 122, 131
- Goldreich, P. & Wu, Y. 1999, *Astrophys. J.*, 511, 904
- Goldstein, J., Townsend, R. H. D., & Zweibel, E. G. 2019, *Astrophys. J.*, 881, 66
- Gossage, S., Conroy, C., Dotter, A., et al. 2018, *Astrophys. J.*, 863, 67
- Goudfrooij, P., Girardi, L., Bellini, A., et al. 2018, *Astrophys. J. Lett.*, 864, L3
- Gough, D. 1985a, *Sol. Phys.*, 100, 65

- Gough, D. 1985b, *Nature*, 314, 14
- Gough, D. O. 1996, *The Observatory*, 116, 313
- Gough, D. O. & Thompson, M. J. 1990, *MNRAS*, 242, 25
- Goupil, M.-J. & Buchler, J. R. 1994, *Astron. Astrophys.*, 291, 481
- Grassitelli, L., Fossati, L., Simón-Díaz, S., et al. 2015, *The Astrophys. J. Lett.*, 808, L31
- Grec, G., Fossat, E., & Pomerantz, M. 1980, *Nature*, 288, 541
- Grosjean, M., Dupret, M. A., Belkacem, K., et al. 2014, *Astron. Astrophys.*, 572, A11
- Gruber, D., Saio, H., Kuschnig, R., et al. 2012, *MNRAS*, 420, 291
- Gruberbauer, M., Guenther, D. B., & Kallinger, T. 2012, *Ap. J.*, 749, 109
- Gruberbauer, M., Guenther, D. B., MacLeod, K., & Kallinger, T. 2013, *MNRAS*, 435, 242
- Guenther, D. B., Demarque, P., & Gruberbauer, M. 2014, *Astrophys. J.*, 787, 164
- Guo, Z. 2020, *Astrophys. J.*, 896, 161
- Guo, Z., Fuller, J., Shporer, A., et al. 2019, *Astrophys. J.*, 885, 46
- Guo, Z., Gies, D. R., & Fuller, J. 2017a, *Astrophys. J.*, 834, 59
- Guo, Z., Gies, D. R., & Matson, R. A. 2017b, *Astrophys. J.*, 851, 39
- Guo, Z. & Li, G. 2019, *Astrophys. J. Lett.*, 882, L5
- Guo, Z., Shporer, A., Hambleton, K., & Isaacson, H. 2020, *Astrophys. J.*, 888, 95
- Guzik, J. A., Kaye, A. B., Bradley, P. A., Cox, A. N., & Neuforge, C. 2000, *Astrophys. J. Lett.*, 542, L57
- Hambleton, K., Fuller, J., Thompson, S., et al. 2018, *MNRAS*, 473, 5165
- Hambleton, K., Kurtz, D. W., Prša, A., et al. 2016, *MNRAS*, 463, 1199
- Hambleton, K. M., Kurtz, D. W., Prša, A., et al. 2013, *MNRAS*, 434, 925
- Handberg, R. & Campante, T. L. 2011, *Astron. Astrophys.*, 527, A56
- Handler, G., Jerzykiewicz, M., Rodríguez, E., et al. 2006, *MNRAS*, 365, 327
- Handler, G., Kurtz, D. W., Rappaport, S. A., et al. 2020, *Nature Astronomy*, 4, 684
- Handler, G., Pigulski, A., Daszyńska-Daszkiewicz, J., et al. 2019, *Astrophys. J. Lett.*, 873, L4
- Handler, G., Rybicka, M., Popowicz, A., et al. 2017, *MNRAS*, 464, 2249
- Hansen, C. J., Kawaler, S. D., & Trimble, V. 2004, *Stellar interiors: physical principles, structure, and evolution*, Astronomy and Astrophysics Library, Springer-Verlag New York
- Heger, A., Langer, N., & Woosley, S. E. 2000, *Astrophys. J.*, 528, 368
- Hekker, S. & Christensen-Dalsgaard, J. 2017, *Astron. Astrophys. Rev.*, 25, 1
- Hekker, S., Elsworth, Y., & Angelou, G. C. 2018, *Astron. Astrophys.*, 610, A80
- Hekker, S., Elsworth, Y., De Ridder, J., et al. 2011, *Astron. Astrophys.*, 525, A131
- Hekker, S., Elsworth, Y., Mosser, B., et al. 2012, *Astron. Astrophys.*, 544, A90
- Hekker, S., Kallinger, T., Baudin, F., et al. 2009, *Astron. Astrophys.*, 506, 465
- Henneco, J., Van Reeth, T., Mathis, S., Mombarg, J. S. G., & Aerts, C. 2021, *Astron. Astrophys.*, submitted
- Hermes, J. J., Charpinet, S., Barclay, T., et al. 2014, *Astrophys. J.*, 789, 85
- Hermes, J. J., Gänsicke, B. T., Kawaler, S. D., et al. 2017a, *Astrophys. J. Suppl. Ser.*, 232, 23
- Hermes, J. J., Kawaler, S. D., Romero, A. D., et al. 2017b, *Astrophys. J. Lett.*, 841, L2
- Hermes, J. J., Montgomery, M. H., Bell, K. J., et al. 2015, *Astrophys. J. :ett.*, 810, L5
- Herwig, F. 2000, *Astron. Astrophys.*, 360, 952
- Hjørringgaard, J. G., Silva Aguirre, V., White, T. R., et al. 2017, *MNRAS*, 464, 3713
- Holdsworth, D. L., Kurtz, D. W., Smalley, B., et al. 2016, *MNRAS*, 462, 876
- Hon, M., Stello, D., García, R. A., et al. 2019, *MNRAS*, 485, 5616
- Horne, J. H. & Baliunas, S. L. 1986, *Astrophys. J.*, 302, 757
- Horst, L., Edelmann, P. V. F., Andrásy, R., et al. 2020, *Astron. Astrophys.*, 641, A18
- Houdek, G., Balmforth, N. J., Christensen-Dalsgaard, J., & Gough, D. O. 1999, *Astron. Astrophys.*, 351, 582
- Houdek, G. & Dupret, M.-A. 2015, *Living Reviews in Solar Physics*, 12, 8
- Houdek, G. & Gough, D. O. 2007, *MNRAS*, 375, 861
- Houdek, G., Lund, M. N., Trampedach, R., et al. 2019, *MNRAS*, 487, 595
- Houdek, G., Trampedach, R., Aarslev, M. J., & Christensen-Dalsgaard, J. 2017, *MNRAS*, 464, L124
- Howell, S. B., Sobek, C., Haas, M., et al. 2014, *Pub. Astron. Soc. Pac.*, 126, 398
- Hu, H., Tout, C. A., Glebbeek, E., & Dupret, M.-A. 2011, *MNRAS*, 418, 195
- Huat, A. L., Hubert, A. M., Baudin, F., et al. 2009, *Astron. Astrophys.*, 506, 95
- Huber, D., Chaplin, W. J., Christensen-Dalsgaard, J., et al. 2013, *Astrophys. J.*, 767, 127
- Huber, D., Ireland, M. J., Bedding, T. R., et al. 2012, *Astrophys. J.*, 760, 32
- Huber, D., Saio, H., Gruberbauer, M., et al. 2008, *Astron. Astrophys.*, 483, 239
- Huber, D., Zinn, J., Bojsen-Hansen, M., et al. 2017, *Astrophys. J.*, 844, 102
- Jeffery, C. S. & Saio, H. 2006, *MNRAS*, 372, L48
- Jiang, C., Christensen-Dalsgaard, J., & Cunha, M. 2018, *MNRAS*, 474, 5413
- Johnson, R. A. & Wichern, D. W. 2007, *Applied Multivariate Statistical Analysis*, 6th Edition, Englewood Cliffs, Prentice-Hall
- Johnston, C., Aerts, C., Pedersen, M. G., & Bastian, N. 2019a, *Astron. Astrophys.*, 632, A74
- Johnston, C., Tkachenko, A., Aerts, C., et al. 2019b, *MNRAS*, 482, 1231
- Jørgensen, A. C. S., Mosumgaard, J. R., Weiss, A., Silva Aguirre, V., & Christensen-Dalsgaard, J. 2018, *MNRAS*, 481, L35
- Jørgensen, A. C. S. & Weiss, A. 2019, *MNRAS*, 488, 3463
- Jørgensen, A. C. S., Weiss, A., Angelou, G., & Silva Aguirre, V. 2019, *MNRAS*, 484, 5551
- Joyce, M. & Chaboyer, B. 2018, *Astrophys. J.*, 856, 10
- Kallinger, T., De Ridder, J., Hekker, S., et al. 2014, *Astron. Astrophys.*, 570, A41
- Kallinger, T., Weiss, W. W., Barban, C., et al. 2010, *Astron. Astrophys.*, 509, A77
- Kallinger, T., Weiss, W. W., Beck, P. G., et al. 2017, *Astron. Astrophys.*, 603, A13

- Karoff, C., Campante, T. L., Ballot, J., et al. 2013, *Astrophys. J.*, 767, 34
- Keen, M. A., Bedding, T. R., Murphy, S. J., et al. 2015, *MNRAS*, 454, 1792
- Kern, J. W., Reed, M. D., Baran, A. S., Telting, J. H., & Østensen, R. H. 2018, *MNRAS*, 474, 4709
- Kervella, P. & Domiciano de Souza, A. 2006, *Astronomy and Astrophysics*, 453, 1059
- Kilkenny, D., Koen, C., O'Donoghue, D., & Stobie, R. S. 1997, *MNRAS*, 285, 640
- Kilkenny, D., Koen, C., O'Donoghue, D., et al. 1999, *MNRAS*, 303, 525
- Kippenhahn, R., Weigert, A., & Weiss, A. 2012, *Stellar Structure and Evolution*, Astronomy and Astrophysics Library, Springer Berlin Heidelberg
- Kjeldsen, H. & Bedding, T. R. 1995, *Astron. Astrophys.*, 293, 87
- Kjeldsen, H., Bedding, T. R., & Christensen-Dalsgaard, J. 2008, *Astrophys. J. Lett.*, 683, L175
- Kjeldsen, H., Bedding, T. R., Viskum, M., & Frandsen, S. 1995, *Astron. J.*, 109, 1313
- Koch, D. G., Borucki, W. J., Basri, G., et al. 2010, *Astrophys. J. Lett.*, 713, L79
- Kollmeier, J. A., Zasowski, G., Rix, H.-W., et al. 2017, ArXiv e-prints (arXiv1711.03234)
- Krtićka, J. & Feldmeier, A. 2018, *Astron. Astrophys.*, 617, A121
- Kumar, P. & Quataert, E. J. 1997, *Astrophys. J. Lett.*, 475, L143
- Kurtz, D. W. 1985, *MNRAS*, 213, 773
- Kurtz, D. W. 1990, *Annu. Rev. Astron. Astrophys.*, 28, 607
- Kurtz, D. W., Cameron, C., Cunha, M. S., et al. 2005, *MNRAS*, 358, 651
- Kurtz, D. W., Cunha, M. S., Saio, H., et al. 2011, *MNRAS*, 414, 2550
- Kurtz, D. W., Handler, G., Rappaport, S. A., et al. 2020, *MNRAS*, 494, 5118
- Kurtz, D. W., Saio, H., Takata, M., et al. 2014, *MNRAS*, 444, 102
- Kurtz, D. W., Shibahashi, H., Murphy, S. J., Bedding, T. R., & Bowman, D. M. 2015, *MNRAS*, 450, 3015
- Laplace, P. S. 1799, *Traité de Mécanique Céleste*, Imprimerie de Crapelet, Paris
- Lebreton, Y. & Goupil, M. J. 2014, *Astron. Astrophys.*, 569, A21
- Lebreton, Y., Goupil, M. J., & Montalbán, J. 2014, in *EAS Publications Series*, Vol. 65, EAS Publications Series, 177–223
- Ledoux, P. 1951, *Astrophys. J.*, 114, 373
- Ledoux, P. 1962, *Bulletin de l'Académie Royale de Belgique*, 48, 240
- Ledoux, P. & Walraven, T. 1958, *Handbuch der Physik*, 51, 353
- Lee, U. & Baraffe, I. 1995, *Astron. Astrophys.*, 301, 419
- Lee, U. & Saio, H. 1987a, *MNRAS*, 224, 513
- Lee, U. & Saio, H. 1987b, *MNRAS*, 225, 643
- Lee, U. & Saio, H. 1989, *MNRAS*, 237, 875
- Lee, U. & Saio, H. 1997, *Astrophys. J.*, 491, 839
- Lee, U. & Saio, H. 2020, *MNRAS*, 497, 4117
- Lefever, K., Puls, J., & Aerts, C. 2007, *Astron. Astrophys.*, 463, 1093
- Li, C., Sun, W., de Grijs, R., et al. 2019a, *Astrophys. J.*, 876, 65
- Li, G., Bedding, T. R., Murphy, S. J., et al. 2019b, *MNRAS*, 482, 1757
- Li, G., Van Reeth, T., Bedding, T. R., Murphy, S. J., & Antoci, V. 2019c, *MNRAS*, 487, 782
- Li, G., Van Reeth, T., Bedding, T. R., et al. 2020, *MNRAS*, 491, 3586
- Lignières, F., Rieutord, M., & Reese, D. 2006, *Astron. Astrophys.*, 455, 607
- Loi, S. T. 2020, *MNRAS*, 496, 3829
- Loi, S. T. & Papaloizou, J. C. B. 2020, *MNRAS*, 491, 708
- Longair, M. 2001, *Pub. Astron. Soc. Pac.*, 113, 1
- Loumos, G. L. & Deeming, T. J. 1978, *Astrophys. Space Science.*, 56, 285
- Lovekin, C. C. & Deupree, R. G. 2008, *Astrophys. J.*, 679, 1499
- Lovekin, C. C., Deupree, R. G., & Clement, M. J. 2009, *Astrophys. J.*, 693, 677
- Lund, M. N., Silva Aguirre, V., Davies, G. R., et al. 2017, *Astrophys. J.*, 835, 172
- Lundkvist, M. S., Kjeldsen, H., Albrecht, S., et al. 2016, *Nature Communications*, 7, 11201
- Maceroni, C., Montalbán, J., Gandolfi, D., Pavlovski, K., & Rainer, M. 2013, *Astron. Astrophys.*, 552, A60
- Maceroni, C., Montalbán, J., Michel, E., et al. 2009, *Astron. Astrophys.*, 508, 1375
- Maeder, A. 1999, *Astronomy and Astrophysics*, 347, 185
- Maeder, A. 2003, *Astron. Astrophys.*, 399, 263
- Maeder, A. 2009, *Physics, Formation and Evolution of Rotating Stars*, Astronomy and Astrophysics Library, Springer Berlin Heidelberg
- Magic, Z. & Weiss, A. 2016, *Astron. Astrophys.*, 592, A24
- Maia, M. T., Meléndez, J., Lorenzo-Oliveira, D., Spina, L., & Jofré, P. 2019, *Astron. Astrophys.*, 628, A126
- Marques, J. P., Goupil, M. J., Lebreton, Y., et al. 2013, *Astron. Astrophys.*, 549, A74
- Martins, F. & Palacios, A. 2013, *Astron. Astrophys.*, 560, A16
- Mathias, P., Le Contel, J. M., Chapellier, E., et al. 2004, *Astron. Astrophys.*, 417, 189
- Mathis, S. 2009, *Astron. Astrophys.*, 506, 811
- Mathis, S. 2013, in *Lecture Notes in Physics*, Berlin Springer Verlag, ed. M. Goupil, K. Belkacem, C. Neiner, F. Lignières, & J. J. Green, Vol. 865, 23
- Mathis, S. & Prat, V. 2019, *Astron. Astrophys.*, 631, A26
- Mathur, S., García, R. A., Ballot, J., et al. 2014, *Astron. Astrophys.*, 562, A124
- Mathur, S., García, R. A., Bugnet, L., et al. 2019, *Frontiers in Astronomy and Space Sciences*, 6, 46
- Mathur, S., García, R. A., Catala, C., et al. 2010, *Astron. Astrophys.*, 518, A53
- Mathur, S., García, R. A., Huber, D., et al. 2016, *Astrophys. J.*, 827, 50
- Mathur, S., Hekker, S., Trampedach, R., et al. 2011, *Astrophys. J.*, 741, 119
- Mathur, S., Huber, D., Batalha, N. M., et al. 2017, *Astrophys. J. Suppl. Ser.*, 229, 30
- Matthews, J. M. 2007, *Communications in Asteroseismology*, 150, 333
- Maxted, P. F. L., Serenelli, A. M., Miglio, A., et al. 2013, *Nature*, 498, 463
- Mazumdar, A., Monteiro, M. J. P. F. G., Ballot, J., et al. 2014, *Astrophys. J.*, 782, 18
- McKeever, J. M., Basu, S., & Corsaro, E. 2019, *Astrophys. J.*, 874, 180
- Meakin, C. A. & Arnett, D. 2007, *Astrophys. J.*, 667, 448
- Meibom, S., Barnes, S. A., Platais, I., et al. 2015, *Nature*,

- 517, 589
- Metcalfe, T. S., Creevey, O. L., Doğan, G., et al. 2014, *Astrophys. J. Suppl. Ser.*, 214, 27
- Michaud, G., Alecian, G., & Richer, J. 2015, Atomic Diffusion in Stars
- Michaud, G., Richard, O., Richer, J., & VandenBerg, D. A. 2004, *Ap. J.*, 606, 452
- Michel, E., Baglin, A., Auvergne, M., et al. 2008, *Science*, 322, 558
- Michielsen, M., Pedersen, M. G., Augustson, K. C., Mathis, S., & Aerts, C. 2019, *Astron. Astrophys.*, 628, A76
- Miglio, A., Chiappini, C., Morel, T., et al. 2013, *MNRAS*, 429, 423
- Miglio, A. & Montalbán, J. 2005, *Astron. Astrophys.*, 441, 615
- Miglio, A., Montalbán, J., Baudin, F., et al. 2009, *Astron. Astrophys.*, 503, L21
- Miglio, A., Montalbán, J., Carrier, F., et al. 2010, *Astron. Astrophys.*, 520, L6
- Miglio, A., Montalbán, J., Noels, A., & Eggenberger, P. 2008, *MNRAS*, 386, 1487
- Mombarg, J. S. G., Dotter, A., Van Reeth, T., et al. 2020, *Astrophys. J.*, 895, 51
- Mombarg, J. S. G., Van Reeth, T., Pedersen, M. G., et al. 2019, *MNRAS*, 485, 3248
- Monteiro, M. J. P. F. G., ed. 2009, Ed., Evolution and Seismic Tools for Stellar Astrophysics, Vol. 316
- Monteiro, M. J. P. F. G., Christensen-Dalsgaard, J., & Thompson, M. J. 1994, *Astron. Astrophys.*, 283, 247
- Monteiro, M. J. P. F. G., Christensen-Dalsgaard, J., & Thompson, M. J. 2000, *MNRAS*, 316, 165
- Monteiro, M. J. P. F. G. & Thompson, M. J. 2005, *MNRAS*, 361, 1187
- Montgomery, M. H. 2005, *Astrophys. J.*, 633, 1142
- Montgomery, M. H., Hermes, J. J., Winget, D. E., Dunlap, B. H., & Bell, K. J. 2020, *Astrophys. J.*, 890, 11
- Montgomery, M. H. & O'Donoghue, D. 1999, *Delta Scuti Star Newsletter*, 13, 28
- Moravveji, E. 2016, *MNRAS*, 455, L67
- Moravveji, E., Aerts, C., Pápics, P. I., Triana, S. A., & Vandoren, B. 2015, *Astron. Astrophys.*, 580, A27
- Moravveji, E., Moya, A., & Guinan, E. F. 2012, *Astrophys. J.*, 749, 74
- Moravveji, E., Townsend, R. H. D., Aerts, C., & Mathis, S. 2016, *Astrophys. J.*, 823, 130
- Moskalik, P. & Dziembowski, W. A. 1992, *Astron. Astrophys.*, 256, L5
- Mosser, B. & Appourchaux, T. 2009, *Astron. Astrophys.*, 508, 877
- Mosser, B., Belkacem, K., Goupil, M. J., et al. 2010, *Astron. Astrophys.*, 517, A22
- Mosser, B., Belkacem, K., Pinçon, C., et al. 2017a, *Astron. Astrophys.*, 598, A62
- Mosser, B., Benomar, O., Belkacem, K., et al. 2014, *Astron. Astrophys.*, 572, L5
- Mosser, B., Dziembowski, W. A., Belkacem, K., et al. 2013, *Astron. Astrophys.*, 559, A137
- Mosser, B., Gehan, C., Belkacem, K., et al. 2018, *Astron. Astrophys.*, 618, A109
- Mosser, B., Goupil, M. J., Belkacem, K., et al. 2012, *Astron. Astrophys.*, 548, A10
- Mosser, B., Pinçon, C., Belkacem, K., Takata, M., & Vrad, M. 2017b, *Astron. Astrophys.*, 600, A1
- Mosser, B., Vrad, M., Belkacem, K., Deheuvels, S., & Goupil, M. J. 2015, *Astron. Astrophys.*, 584, A50
- Mosumgaard, J. R., Jørgensen, A. C. S., Weiss, A., Silva Aguirre, V., & Christensen-Dalsgaard, J. 2020, *MNRAS*, 491, 1160
- Murphy, S. J., Hey, D., Van Reeth, T., & Bedding, T. R. 2019, *MNRAS*, 485, 2380
- Murphy, S. J., Pigulski, A., Kurtz, D. W., et al. 2013a, *MNRAS*, 432, 2284
- Murphy, S. J., Shibahashi, H., & Kurtz, D. W. 2013b, *MNRAS*, 430, 2986
- Neiner, C., Floquet, M., Samadi, R., et al. 2012, *Astron. Astrophys.*, 546, A47
- Neiner, C., Lee, U., Mathis, S., et al. 2020, *Astron. Astrophys.*, arXiv:2007.08977
- North, J. R., Davis, J., Bedding, T. R., et al. 2007, *MNRAS*, 380, L80
- Østensen, R. H., Telting, J. H., Reed, M. D., et al. 2014, *Astron. Astrophys.*, 569, A15
- Ouazzani, R.-M., Dupret, M.-A., & Reese, D. R. 2012, *Astron. Astrophys.*, 547, A75
- Ouazzani, R. M., Lignières, F., Dupret, M. A., et al. 2020, *Astron. Astrophys.*, 640, A49
- Ouazzani, R. M., Marques, J. P., Goupil, M. J., et al. 2019, *Astron. Astrophys.*, 626, A121
- Ouazzani, R.-M., Salmon, S. J. A. J., Antoci, V., et al. 2017, *MNRAS*, 465, 2294
- Pablo, H., Whittaker, G. N., Popowicz, A., et al. 2016, *Pub. Astron. Soc. Pac.*, 128, 125001
- Pamyatnykh, A. A. 1999, *Acta Astron.*, 49, 119
- Papaloizou, J. & Pringle, J. E. 1978, *MNRAS*, 182, 423
- Papaloizou, J. C. B. & Savonije, G. J. 1997, *MNRAS*, 291, 651
- Pápics, P. I. 2012, *Astron. Nachrichten*, 333, 1053
- Pápics, P. I. 2013, PhD thesis, Instituut voor Sterrenkunde, KU Leuven, Celestijnenlaan 200D, B-3001 Leuven, Belgium
- Pápics, P. I., Moravveji, E., Aerts, C., et al. 2014, *Astron. Astrophys.*, 570, A8
- Pápics, P. I., Tkachenko, A., Aerts, C., et al. 2013, *Astron. Astrophys.*, 553, A127
- Pápics, P. I., Tkachenko, A., Aerts, C., et al. 2015, *Ap. J. Lett.*, 803, L25
- Pápics, P. I., Tkachenko, A., Van Reeth, T., et al. 2017, *Astron. Astrophys.*, 598, A74
- Paquette, C., Pelletier, C., Fontaine, G., & Michaud, G. 1986, *Ap. J. Suppl. Ser.*, 61, 177
- Paxton, B., Bildsten, L., Dotter, A., et al. 2011, *Ap. J. Suppl.*, 192, 3
- Paxton, B., Cantiello, M., Arras, P., et al. 2013, *Ap. J. Suppl.*, 208, 4
- Paxton, B., Marchant, P., Schwab, J., et al. 2015, *Ap. J. Suppl.*, 220, 15
- Paxton, B., Schwab, J., Bauer, E. B., et al. 2018, *Ap. J. Suppl.*, 234, 34
- Paxton, B., Smolec, R., Schwab, J., et al. 2019, *Astrophys. J. Suppl. Ser.*, 243, 10
- Pedersen, M. G., Aerts, C., Pápics, P. I., et al. 2021, *under review*
- Pedersen, M. G., Aerts, C., Pápics, P. I., & Rogers, T. M. 2018, *Astron. Astrophys.*, 614, A128
- Pedersen, M. G., Chowdhury, S., Johnston, C., et al. 2019, *Astrophys. J. Lett.*, 872, L9
- Pérez Hernández, F., García, R. A., Mathur, S., Santos, A. R. G., & Régulo, C. 2019, *Frontiers in Astronomy and*

- Space Sciences*, 6, 41
- Petrenz, P. & Puls, J. 2000, *Astron. Astrophys.*, 358, 956
- Pigulski, A., Cugier, H., Popowicz, A., et al. 2016, *Astron. Astrophys.*, 588, A55
- Pinçon, C., Goupil, M. J., & Belkacem, K. 2019, *Astron. Astrophys.*, arXiv:1912.06008
- Pinsonneault, M. 1997, *Ann. Rev. Astron. Astrophys.*, 35, 557
- Pinsonneault, M. H., Elsworth, Y. P., Tayar, J., et al. 2018, *Astrophys. J. Suppl. Ser.*, 239, 32
- Pope, B. J. S., White, T. R., Farr, W. M., et al. 2019, *Astrophys. J. Suppl. Ser.*, 245, 8
- Prat, V., Mathis, S., Augustson, K., et al. 2018, *Astron. Astrophys.*, 615, A106
- Prat, V., Mathis, S., Buyschaert, B., et al. 2019, *Astron. Astrophys.*, 627, A64
- Prat, V., Mathis, S., Lignières, F., Ballot, J., & Culpin, P.-M. 2017, *Astron. Astrophys.*, 598, A105
- Prat, V., Mathis, S., Neiner, C., et al. 2020, *Astron. Astrophys.*, 636, A100
- Przybilla, N., Nieva, M. F., Irrgang, A., & Butler, K. 2013, in *EAS Pub. Ser.*, Vol. 63, , 13–23
- Ramiaramanantsoa, T., Moffat, A. F. J., Harmon, R., et al. 2018, *MNRAS*, 473, 5532
- Ratnasingam, R. P., Edelmann, P. V. F., & Rogers, T. M. 2019, *MNRAS*, 482, 5500
- Rauer, H., Catala, C., Aerts, C., et al. 2014, *Exp. Astron.*, 38, 249
- Reed, M. D., Baran, A., Quint, A. C., et al. 2011, *MNRAS*, 414, 2885
- Reed, M. D., Foster, H., Telting, J. H., et al. 2014, *MNRAS*, 440, 3809
- Reese, D., Lignières, F., & Rieutord, M. 2006, *Astron. Astrophys.*, 455, 621
- Reese, D. R., Prat, V., Barban, C., van 't Veer-Menneret, C., & MacGregor, K. B. 2013, *Astronomy and Astrophysics*, 550, A77
- Rendle, B. M., Miglio, A., Chiappini, C., et al. 2019, *MNRAS*, 490, 4465
- Richard, O., Michaud, G., & Richer, J. 2002a, *Ap. J.*, 580, 1100
- Richard, O., Michaud, G., Richer, J., et al. 2002b, *Ap. J.*, 568, 979
- Richer, J., Michaud, G., & Turcotte, S. 2000, *Ap. J.*, 529, 338
- Ricker, G. R., Vanderspek, R., Winn, J., et al. 2016, in Society of Photo-Optical Instrumentation Engineers (SPIE) Conference Series, Vol. 9904, *Proc. SPIE*, 99042B
- Rieutord, M., Espinosa Lara, F., & Putigny, B. 2016, *Journal of Computational Physics*, 318, 277
- Rogers, T. & Glatzmaier, G. 2005, *MNRAS*, 364, 1135
- Rogers, T. M. 2015, *Astrophys. J. Lett.*, 815, L30
- Rogers, T. M., Lin, D. N. C., McElwaine, J. N., & Lau, H. H. B. 2013, *Astrophys. J.*, 772, 21
- Rogers, T. M. & McElwaine, J. N. 2017, *Astrophys. J. Lett.*, 848, L1
- Romero, A. D., Córscico, A. H., Castanheira, B. G., et al. 2017, *Ap. J.*, 851, 60
- Rosenthal, C. S., Christensen-Dalsgaard, J., Nordlund, Å., Stein, R. F., & Trampedach, R. 1999, *Astron. Astrophys.*, 351, 689
- Rowe, J. F., Matthews, J. M., Cameron, C., et al. 2006, *Communications in Asteroseismology*, 148, 34
- Roxburgh, I. W. 2005, *Astron. Astrophys.*, 434, 665
- Roxburgh, I. W. & Vorontsov, S. V. 2003, *Astron. Astrophys.*, 411, 215
- Roxburgh, I. W. & Vorontsov, S. V. 2006, *MNRAS*, 369, 1491
- Sahlholdt, C. L. & Silva Aguirre, V. 2018, *MNRAS*, 481, L125
- Saio, H. 1981, *Astrophys. J.*, 244, 299
- Saio, H. 1982, *Astrophys. J.*, 256, 717
- Saio, H. 2014, in IAU Symposium, Vol. 301, Precision Asteroseismology, ed. J. A. Guzik, W. J. Chaplin, G. Handler, & A. Pigulski, 197–204
- Saio, H., Bedding, T. R., Kurtz, D. W., et al. 2018a, *MNRAS*, 477, 2183
- Saio, H., Cameron, C., Kuschnig, R., et al. 2007, *Astrophys. J.*, 654, 544
- Saio, H. & Jeffery, C. S. 2019, *MNRAS*, 482, 758
- Saio, H., Kurtz, D. W., Murphy, S. J., Antoci, V. L., & Lee, U. 2018b, *MNRAS*, 474, 2774
- Saio, H., Kurtz, D. W., Takata, M., et al. 2015, *MNRAS*, 447, 3264
- Saio, H., Kuschnig, R., Gautschi, A., et al. 2006, *Ap. J.*, 650, 1111
- Salaris, M. & Cassisi, S. 2017, *Roy. Soc. Open Science*, 4, 170192
- Sana, H., de Mink, S. E., de Koter, A., et al. 2012, *Science*, 337, 444
- Santos, A. R. G., Campante, T. L., Chaplin, W. J., et al. 2019, *Astrophys. J.*, 883, 65
- Savonije, G. J. & Papaloizou, J. C. B. 1997, *MNRAS*, 291, 633
- Scargle, J. D. 1982, *Astrophys. J.*, 263, 835
- Schmid, V. S. & Aerts, C. 2016, *Astron. Astrophys.*, 592, A116
- Schofield, M., Chaplin, W. J., Huber, D., et al. 2019, *Astrophys. J. Suppl.*, 241, 12
- Schonhut-Stasik, J., Huber, D., Baranec, C., et al. 2020, *Astrophys. J.*, 888, 34
- Schwarzenberg-Czerny, A. 1991, *MNRAS*, 253, 198
- Schwarzenberg-Czerny, A. 1998, *MNRAS*, 301, 831
- Serenelli, A., Johnson, J., Huber, D., et al. 2017, *Astrophys. J. Suppl.*, 233, 23
- Serenelli, A., Weiss, A., Aerts, C., et al. 2021, *Astron. Astrophys. Rev.*, under review, arXiv:2006.10868
- Sharma, S., Stello, D., Bland-Hawthorn, J., et al. 2019, *MNRAS*, 490, 5335
- Shibahashi, H. 1979, *Pub. Astron. Soc. Japan*, 31, 87
- Shibahashi, H. & Takata, M. 1993, *Pub. Astron. Soc. Japan*, 45, 617
- Silva Aguirre, V., Bojsen-Hansen, M., Slumstrup, D., et al. 2018, *MNRAS*, 475, 5487
- Silva Aguirre, V., Casagrande, L., Basu, S., et al. 2012, *Astrophys. J.*, 757, 99
- Silva Aguirre, V., Christensen-Dalsgaard, J., Cassisi, S., et al. 2020, *Astron. Astrophys.*, 635, A164
- Silva Aguirre, V., Davies, G. R., Basu, S., et al. 2015, *MNRAS*, 452, 2127
- Silva Aguirre, V., Lund, M. N., Antia, H. M., et al. 2017, *Astrophys. J.*, 835, 173
- Skumanich, A. 1972, *Astrophys. J.*, 171, 565
- Smeyers, P. & Moya, A. 2007, *Astron. Astrophys.*, 465, 509
- Smeyers, P. & Van Hoolst, T. 2010, *Astrophysics and Space Science Library*, Vol. 371, Linear Isentropic Oscillations of Stars: Theoretical Foundations
- Sódor, Á., Chené, A. N., De Cat, P., et al. 2014, *Astron. Astrophys.*, 568, A106
- Sonoi, T., Samadi, R., Belkacem, K., et al. 2015, *Astron. Astrophys.*, 583, A112
- Soszyński, I., Udalski, A., Szymański, M. K., et al. 2016, *Acta Astron.*, 66, 131

- Soufi, F., Goupil, M. J., & Dziembowski, W. A. 1998, *Astron. Astrophys.*, 334, 911
- Southworth, J., Bowman, D. M., Tkachenko, A., & Pavlovski, K. 2020, *MNRAS*, 497, L19
- Southworth, J., Bruntt, H., & Buzasi, D. L. 2007, *Astron. Astrophys.*, 467, 1215
- Stello, D., Bruntt, H., Preston, H., & Buzasi, D. 2008, *Astrophys. J. Lett.*, 674, L53
- Stello, D., Cantiello, M., Fuller, J., et al. 2016, *Nature*, 529, 364
- Stello, D., Compton, D. L., Bedding, T. R., et al. 2014, *Astrophys. J. Lett.*, 788, L10
- Stello, D., Huber, D., Sharma, S., et al. 2015, *Astrophys. J. Lett.*, 809, L3
- Stello, D., Zinn, J., Elsworth, Y., et al. 2017, *Astrophys. J.*, 835, 83
- Suárez, J. C., Goupil, M. J., & Morel, P. 2006, *Astron. Astrophys.*, 449, 673
- Suárez, J. C., Goupil, M. J., Reese, D. R., et al. 2010, *Astrophys. J.*, 721, 537
- Sundqvist, J. O., Petit, V., Owocki, S. P., et al. 2013, *MNRAS*, 433, 2497
- Szewczuk, W. & Daszyńska-Daszkiewicz, J. 2017, *MNRAS*, 469, 13
- Szewczuk, W. & Daszyńska-Daszkiewicz, J. 2018, *MNRAS*, 478, 2243
- Takata, M. 2012, *Pub. Astron. Soc. Japan*, 64, 66
- Takata, M. 2016a, *Pub. Astron. Soc. Japan*, 68, 109
- Takata, M. 2016b, *Pub. Astron. Soc. Japan*, 68, 91
- Takata, M., Ouazzani, R. M., Saio, H., et al. 2020, *Astron. Astrophys.*, 635, A106
- Talon, S. & Charbonnel, C. 2008, *Astron. Astrophys.*, 482, 597
- Tassoul, M. 1980, *Astrophys. J. Suppl. Ser.*, 43, 469
- Tassoul, M. 1990, *Astrophys. J.*, 358, 313
- Tayar, J., Beck, P. G., Pinsonneault, M. H., García, R. A., & Mathur, S. 2019, *Astrophys. J.*, 887, 203
- Telting, J. H., Østensen, R. H., Baran, A. S., et al. 2012, *Astron. Astrophys.*, 544, A1
- Terquem, C., Papaloizou, J. C. B., Nelson, R. P., & Lin, D. N. C. 1998, *Astrophys. J.*, 502, 788
- Théado, S., Alecian, G., LeBlanc, F., & Vauclair, S. 2012, *Astron. Astrophys.*, 546, A100
- Themeßl, N., Hekker, S., Southworth, J., et al. 2018, *MNRAS*, 478, 4669
- Thompson, S. E., Everett, M., Mullally, F., et al. 2012, *Astrophys. J.*, 753, 86
- Thoul, A. A., Bahcall, J. N., & Loeb, A. 1994, *Astrophys. J.*, 421, 828
- Timmes, F. X., Townsend, R. H. D., Bauer, E. B., et al. 2018, *Astrophys. J. Lett.*, 867, L30
- Tkachenko, A., Degroote, P., Aerts, C., et al. 2014, *MNRAS*, 438, 3093
- Tkachenko, A., Pavlovski, K., Johnston, C., et al. 2020, *Astron. Astrophys.*, 637, A60
- Tong, V. & García, R. 2015, *Extraterrestrial Seismology* (ISBN: 9781107300668. Cambridge: Cambridge University Press)
- Torres, G., Andersen, J., & Giménez, A. 2010, *Astron. Astrophys. Rev.*, 18, 67
- Townsend, R. H. D. 2003a, *MNRAS*, 343, 125
- Townsend, R. H. D. 2003b, *MNRAS*, 340, 1020
- Townsend, R. H. D., Goldstein, J., & Zweibel, E. G. 2018, *MNRAS*, 475, 879
- Townsend, R. H. D. & Teitler, S. A. 2013, *MNRAS*, 435, 3406
- Trampedach, R., Aarslev, M. J., Houdek, G., et al. 2017, *MNRAS*, 466, L43
- Triana, S. A., Moravveji, E., Pápics, P. I., et al. 2015, *Astrophys. J.*, 810, 16
- Trimble, V. & Leonard, P. J. T. 1996, *Pub. Astron. Soc. Pac.*, 108, 8
- Turcotte, S., Richer, J., & Michaud, G. 1998, *Ap. J.*, 504, 559
- Unno, W., Osaki, Y., Ando, H., Saio, H., & Shibahashi, H. 1989, *Nonradial oscillations of stars*, Tokyo: University of Tokyo Press, 1989, 2nd ed.
- Uzundag, M., Baran, A. S., Østensen, R. H., et al. 2017, *MNRAS*, 472, 700
- Van Beek, J., Prat, V., Van Reeth, T., et al. 2020, *Astron. Astrophys.*, 638, A149
- Van Eylen, V., Arentoft, C., Lundkvist, M. S., et al. 2018, *MNRAS*, 479, 4786
- Van Eylen, V., Lund, M. N., Silva Aguirre, V., et al. 2014, *Astrophys. J.*, 782, 14
- Van Grootel, V., Charpinet, S., Brassard, P., Fontaine, G., & Green, E. M. 2013, *Astron. Astrophys.*, 553, A97
- Van Grootel, V., Charpinet, S., Fontaine, G., et al. 2010a, *Astrophys. J. Lett.*, 718, L97
- Van Grootel, V., Charpinet, S., Fontaine, G., Green, E. M., & Brassard, P. 2010b, *Astron. Astrophys.*, 524, A63
- Van Hoolst, T. 1994, *Astron. Astrophys.*, 292, 471
- Van Reeth, T., Mombarg, J. S. G., Mathis, S., et al. 2018, *Astron. Astrophys.*, 618, A24
- Van Reeth, T., Tkachenko, A., & Aerts, C. 2016, *Astron. Astrophys.*, 593, A120
- Van Reeth, T., Tkachenko, A., Aerts, C., et al. 2015, *Astrophys. J. Suppl.*, 218, 27
- van Saders, J. L., Ceillier, T., Metcalfe, T. S., et al. 2016, *Nature*, 529, 181
- VandenBerg, D. A., Richard, O., Michaud, G., & Richer, J. 2002, *Ap. J.*, 571, 487
- Verma, K., Antia, H. M., Basu, S., & Mazumdar, A. 2014, *Astrophys. J.*, 794, 114
- Verma, K., Raodeo, K., Antia, H. M., et al. 2017, *Astrophys. J.*, 837, 47
- Verma, K., Raodeo, K., Basu, S., et al. 2019, *MNRAS*, 483, 4678
- Verma, K. & Silva Aguirre, V. 2019, *MNRAS*, 489, 1850
- Viallet, M., Meakin, C., Arnett, D., & Mocák, M. 2013, *Astrophys. J.*, 769, 1
- Viallet, M., Meakin, C., Prat, V., & Arnett, D. 2015, *Astron. Astrophys.*, 580, A61
- Viani, L. S., Basu, S., Joel Ong J., M., Bonaca, A., & Chaplin, W. J. 2018, *Astrophys. J.*, 858, 28
- von Zeipel, H. 1924, *MNRAS*, 84, 665
- Vrard, M., Kallinger, T., Mosser, B., et al. 2018, *Astron. Astrophys.*, 616, A94
- Wade, G. A., Neiner, C., Alecian, E., et al. 2016, *MNRAS*, 456, 2
- Walker, G., Matthews, J., Kuschnig, R., et al. 2003, *Pub. Astron. Soc. Pac.*, 115, 1023
- Walker, G. A. H., Kuschnig, R., Matthews, J. M., et al. 2005a, *Astrophys. J. Lett.*, 635, L77
- Walker, G. A. H., Kuschnig, R., Matthews, J. M., et al. 2005b, *Astrophys. J. Lett.*, 623, L145
- Weinberg, N. N. & Arras, P. 2019, *Astrophys. J.*, 873, 67
- Weiss, W. W., Rucinski, S. M., Moffat, A. F. J., et al. 2014, *Pub. Astron. Soc. Pac.*, 126, 573
- Welsh, W. F., Orosz, J. A., Aerts, C., et al. 2011, *Astrophys.*

- J. Suppl. Ser.*, 197, 4
- White, T. R., Huber, D., Maestro, V., et al. 2013, *MNRAS*, 433, 1262
- White, T. R., Huber, D., Mann, A. W., et al. 2018, *MNRAS*, 477, 4403
- Willems, B. 2003, *MNRAS*, 346, 968
- Winget, D. E., Nather, R. E., Clemens, J. C., et al. 1991, *Ap. J.*, 378, 326
- Winget, D. E., Nather, R. E., Clemens, J. C., et al. 1994, *Astrophys. J.*, 430, 839
- Witte, M. G. & Savonije, G. J. 1999, *Astron. Astrophys.*, 341, 842
- Wu, T. & Li, Y. 2019, *Astrophys. J.*, 881, 86
- Wu, Y. 2001, *MNRAS*, 323, 248
- Yu, J., Bedding, T. R., Stello, D., et al. 2020, *MNRAS*, 493, 1388
- Yu, J., Huber, D., Bedding, T. R., et al. 2018, *Astrophys. J. Suppl. Ser.*, 236, 42
- Zahn, J.-P. 1975, *Astron. Astrophys.*, 41, 329
- Zahn, J.-P. 1991, *Astron. Astrophys.*, 252, 179
- Zahn, J.-P. 1992, *Astron. Astrophys.*, 265, 115
- Zerbi, F. M., Rodríguez, E., Garrido, R., et al. 1999, *MNRAS*, 303, 275
- Zhou, Y., Asplund, M., & Collet, R. 2019, *Astrophys. J.*, 880, 13
- Zinn, J. C., Pinsonneault, M. H., Huber, D., et al. 2019, *Astrophys. J.*, 885, 166
- Zong, W., Charpinet, S., & Vauclair, G. 2016a, *Astron. Astrophys.*, 594, A46
- Zong, W., Charpinet, S., Vauclair, G., Giammichele, N., & Van Grootel, V. 2016b, *Astron. Astrophys.*, 585, A22
- Zwintz, K. 2008, *Astrophys. J.*, 673, 1088
- Zwintz, K., Fossati, L., Ryabchikova, T., et al. 2014, *Science*, 345, 550
- Zwintz, K., Hareter, M., Kuschnig, R., et al. 2009, *Astron. Astrophys.*, 502, 239
- Zwintz, K., Weiss, W. W., Kuschnig, R., et al. 2000, *Astron. Astrophys. Suppl. Ser.*, 145, 481